Modulating Charge Transport in Angular Naphthothiazoles Through Crystal Engineering

A thesis submitted for the degree of

Doctor of Philosophy

in

Chemistry

by

Athira T. John

Indian Institute of Science Education and Research
Thiruvananthapuram (IISER TVM),
Thiruvananthapuram – 695551
Kerala, India

November 2022

Declaration

I hereby declare that the Ph. D. thesis entitled **"Modulating Charge Transport in Angular Naphthothiazoles Through Crystal Engineering"** is an independent work carried out by me at the School of Chemistry, Indian Institute of Science Education and Research Thiruvananthapuram (IISER TVM), under the supervision of **Prof. Mahesh Hariharan** and it has not been submitted anywhere else for any other degree, diploma or title. In keeping with the general practice of reporting the scientific observations, due acknowledgements have been made wherever the work described is based on the findings of other investigators.

Place: IISER Thiruvananthapuram **Athira T. John**

Date: 02-11-2022

Certificate

This is to certify that the work embodied in the thesis entitled **"Modulating Charge Transport in Angular Naphthothiazoles Through Crystal Engineering"** has been carried out by **Athira T. John (PHD171005)** under my supervision at the School of Chemistry, Indian Institute of Science Education and Research Thiruvananthapuram (IISER TVM) and the same has not been submitted elsewhere for a degree.

Place: IISER Thiruvananthapuram
Date: 02-11-2022

Prof. Mahesh Hariharan
(Thesis Supervisor)

Dedicated

To

My Beloved family
Teachers
and
Friends

Acknowledgements

Without GOD's grace, I would not have the endurance to walk down this path with self-belief and courage to complete my Ph.D. If it weren't for the love, kindness, and encouragement of countless people throughout the years, I wouldn't be where I am today. I want to thank all of them for supporting me in this journey.

First and foremost, for this great experience I thank my thesis supervisor, Prof. Mahesh Hariharan for his continuous mentorship and guidance during my Ph.D. journey. I also want to express my sincere gratitude for your compassion and encouragement while I struggled through my Ph.D. I could not have imagined having a better mentor and advisor for my Ph.D. research.

I would like to express my sincere thanks to Prof. J. N. Moorthy and Prof. V. Ramakrishnan, present and former Directors of IISER TVM, for providing excellent infrastructure and research facilities at IISER TVM. I am also grateful to my thesis doctoral committee members, Prof. K. George Thomas and Dr. Reji Varghese for their timely suggestions, support and encouragement. I thank all my Ph.D. course instructors and faculty members of the school of chemistry at IISER TVM for inspiring me to broaden my research horizons. I extent my wholehearted thanks to Prof. T. Radhakrishnan (University of Hyderabad) for providing insightful comments and recommendations on my research work.

I am deeply obliged to all past and present members of the Hariharan group: Dr. Kalaivanan N., Dr. Abbey M. P., Dr. Nanditha G. N., Dr. Remya R., Dr. Ebin S., Ms. Devika S., Dr. Arun T., Ms. Amalu M., Ms. Lijina M. P., Dr. Mahesh G., Ms. Swathi Krishna P. E., Dr. Bappa G., Mr. Aniruddha M., Ms. Kavya V., Mr. Jibin S., Mr. Philip D. M., Ms. Ishamol S., Mr. Vinayak B., Mr. Amal K. H., Mr. Niyas M. A., Ms. Ambili R. V., Ms. Hridya P., Mr. Vishnu V., Ms. Meera M., Mr. Alfy B., Mr. Deepu G., Mr. Patoju S. D., Mr. Krishna P., Mr. Jeswin S., Ms. Akshaya N., Ms. Keerthy P. S., Mr. Vivek V. D., Mr. Akhilesh K. U., Ms. Hruidya C. B., Mr. Sohan D. J., Mr. Dillep P. S., and Ms. Pallavi P. D., Ms. Dayana, Ms. Medha, Ms. Suvarna S. C., Ms. Asma S., for the care, inspiration, and assistance during my Ph. D. work. I would also like to express my sincere gratitude to all the exceptionally brilliant and driven BS-MS students who worked with me: Mr. Deepu G., Ms. Akshaya N., Ms. Keerthy P. S., and have made significant contributions to the research work in the present thesis. I would also like to thank all the project students who have worked with me: Ms. Maalu M., Mr. Eby P., Ms. Pooja R., Mr. Basith, Ms. Devila P., and Mr. Benjamin. I am thankful to Mr. Vishnu E. K. for helping me in the adventurous journey with single-molecule spectroscopy and for the teamwork. Many

thanks to Ms. Saniya G., Ms. Keerthana, Ms. Gayatri, Ms. Athira N., Ms. Anjana J., Ms. Bincy, Ms. Christeena, Ms. Kavya, Ms. Amritha, Ms. Ruth, Ms. Chitra and Ms. Litty for providing me a fun-filled and stimulating environment at IISER TVM.

Special thanks to various people who have made my research life at IISER TVM more joyful. I thank Ms. Aathira E., Ms. Meera J., and Ms. Aparna R. K. for being with me during one of the most challenging times in my life. I thank Ms. Remya, Ms. Lijina M. P., Dr. Bappa G., Ms. Amalu M., Mr. Deepu G., and Mr. Jeswin S. for all the care, support, and inspiration during my research journey at IISER TVM. I would like to thank Ms. Neelima G. for helping me overcome some traumatic situations during my Ph.D. life at IISER TVM. I thank Ms. Shamna, Dr. Feba, Ms. Arya, Dr. Ajay J., Dr. Sulfikar A., Mr. Shafeek, Ms. Shourya, Ms. Anju, Mr. Hari, Mr. Venkadesh. I would also like to thank my Ph.D. batchmates Ms. Meera J., Ms. Amritha R., Ms. Ruth, Ms. Chitra, Mr. Vishnu E. K., Mr. Akash S., and Mr. Javed for the fruitful discussions.

I am grateful to Mr. Alex P. A. for structure solving and single-crystal X-ray diffraction measurements, Mr. Nibith K. for the elemental, GC-MS, and IR analyses, Mr. Adarsh B. for NMR measurements, Mr. Aneesh A., for the SEM analysis, Mr. Pradeep K. G., Ms. Athira S. and Mr. Prem K. for HRMS mass analyses and Mr. Kiran for MALDI-TOF mass analysis. I would also like to express my gratitude to all the teaching and nonteaching (library, purchase, IT, stores, finance, and mess) staff of IISER TVM for their assistance and support. I thank INSPIRE (DST), Government of India, and IISER TVM for the financial assistance.

I take this opportunity to express my sincere gratitude to all my teachers at IISER Mohali especially Dr. Sugumar Venkataramani for giving me flavour of research, motivating me throughout my BSMS major project and being by my side as I took my first steps in the scientific world. I would also like to thank all my friends at IISER Mohali, in particular Ms. Sruthi M., Ms. Amritha S., Ms. Arya J., Ms. Anusree P. V. My wholehearted thanks to Mr. Mayank S., for all the small and big things you did to make me feel less alone. I would like to thank those closest to me, my close friends Ms. Anju A., Ms. Anns T., Ms. Anjana E., for always being a phone call away to make me laugh. I would like to extend huge, warm thanks to Fr. Binny, Fr. Tom, Fr. Dominic for their prayers and constant motivation. I take this opportunity to express my sincere gratitude to all my teachers at St. Joseph's School Vandiperiyar, St. Thomas EMHSS Kumily, St. Mary's GHSS Palai, especially Sr. Albina, Sr. Roseline, Ms. Jessy, Mr. Sreelal, Ms. Mini for their support.

Above all, I want to thank my family for their love, support, sincere encouragement, and inspiration throughout my whole life. My parents have been my pillar of support throughout

my life, during all the hard times in my life, their prayers covered me, their counsel helped me stay strong. I thank my brother for being my enthusiastic cheerleader. Special thanks to my aunt Sr. Deepthy J., for her constant motivation and prayers. I take this opportunity to thank my cousin brother Mr. Ajeesh G., who had always supported and motivated me to aim high. I am forever indebted to my husband for his unconditional support during the ups and downs of the whole Ph.D. process, as well as to all he has sacrificed to make my work a top priority in our life.

Last but not least, thanks to my grandmother for all the love, support, prayers and unconditional love.

- Athira T. John

Preface

The drastic progress in the field of organic electronics can be attributed to the precise understanding of the design and synthesis of efficient organic semiconducting materials. π-conjugated molecules offers the flexibility of fine tuning the semiconducting properties, owing to its rich chemistry, for meeting application-specific demands. Multitude of novel π-conjugated materials functions as vital parts in organic light-emitting diodes, organic photovoltaic cells, and organic field-effect transistors. Since noncovalent interactions dictate crystal packing, control over noncovalent interactions is essential to bridge chemical structure to functional properties. The emergent optical properties of chromophoric systems in the crystalline state are dictated by the molecular structure and relative orientation of neighbouring molecules in the solid state. The solid-state supramolecular arrangement of organic semiconductors is equally decisive as the molecular structure in deciphering the emergent properties, but is more challenging to control. For the development of advanced functional materials, it is crucial to investigate the relationship between charge transport and the various crystalline packing morphologies in organic chromophores from a crystal engineering viewpoint. Investigating the methods to achieve the desired crystalline packing and recognizing new supramolecular motifs with emergent properties would eventually have implications in fundamental crystal engineering, supramolecular chemistry and biomimetic design of functional materials.

The Chapter 1 of the thesis provides a brief synopsis of the different parameters and regimes governing charge transport in organic molecules. Detailed description about band and hopping transport based on the localization of the charge carriers is explained. Anisotropy of charge mobility in organic semiconductors arising due to the variation in the electronic coupling between different pairs of the neighbouring molecules in different directions is presented. The various strategies adopted to obtain the common crystalline packing motifs (herringbone/γ-motif/β- motif/brickwork) by modulation of a) directional interactions, b) co-crystallization, c) polymorphism, d) heteroatom doping, e) orientation of the chromophore and f) shape of the chromophores are covered. Polymorphism in organic crystals affects the charge transport by fine tuning the crystal packing without altering the chemical structure. Orthogonal cross arrangement of chromophoric assembly is an innovative strategy to achieve selective charge filtering phenomena. Suppression of molecular motion and improved orbital overlap

contributing to high thermal device stability are features of molecules with bent π-cores. Thus, exploring the diverse crystalline packing modes adopted by organic chromophores by modulating shape is an emerging area of research.

Chapter 2 describes the hierarchical formation of 1D, 2D and 3D zipper motifs guided by distinct Br•••Br, Br•••S interactions. The work highlights the potential of halogen bonding interactions in fabricating functional supramolecular assemblies. A self-complementary 1D zipper resembling DNA base pair contacts was created by taking use of the potential for numerous connections created by two bromine atoms placed next to a sulphur atom in an angular naphthothiazole. 2,4-dibromo-5-ethoxynaphtho[1,2-*d*]thiazole (NTB_2) forms the molecular zipper by the recurring units of Br_4 synthon, flanked by type I and type II atom efficient Br•••Br interactions. A distinct 12-atom, 13-interaction creating a Br_4 synthon was described by the 1D zipper extending across type I X•••X interactions. Multivalent interactions of sulfur and bromine atoms joined NTB_2 to generate an indefinite 2D halogen-bonded zipper. 3D zipper in NTB2 is formed by the extension of 2D zipper by π-π stacking and a near orthogonal X•••X interaction. Interacting Quantum Atoms analysis highlighted that the exchange correlation component contributed more than the traditional electrostatic factor to the stability of the zipper constructed by Br_4 synthon. The analysis highlights the role of quantum covalency in the genesis of X•••X interactions. The NTB_2 zipper assembly exhibits selective electron transport in the type II X•••X bonded path, in accordance with the semiclassical Marcus theory of charge transport. Band structure study identified crystalline NTB_2 as a wide band gap semiconductor with a band gap of 2.80 eV, opening up new possibilities for the design of advanced functional materials.

Chapter 3 examines the impact of single-atom substitution on altering the crystal packing and optical band gap in 5-methoxynaphtho[1,2-*d*]thiazole (NTH) by systematically altering the molecular structure of NTH by substituting the terminal hydrogen atom with halogens (Cl, Br, I). Numerical descriptors isostructurality (I_s) and cell similarity (π) indices established the similarities in crystal packing of structurally equivalent Br- and I-substituted molecular crystals. To provide a qualitative representation of the 3D topology showing the main interactions in the supramolecular structures of the NTH derivatives, an energy framework analysis was used. The reduction in optical band gap from 3.48 to 3.07 eV was observed as the atomic number of halogen atoms increased, indicating that halogen atoms directly influence the electronic characteristics of organic crystals. The bromine- and iodine-substituted derivatives show a decrease in band gap with a rise in atomic number, despite their isostructural

packing. Isostructurality modulates the molecular architecture in NTB and NTI by eliminating the effects of atomic size and functional group variation. The band structure and projected density of states derived by using DFT calculations were employed to illustrate the lowering of the optical band gap in NTH derivatives. The projected density of states accounted the significant contribution of halogen atoms to the energy levels in band edges. The results indicate the possibility of halogenation in modifying the optoelectronic characteristics of organic functional materials.

In Chapter 4 electronic properties of novel angular 5-methoxynaphtho[1,2-*d*]thiazol-2-amine (NTN) and 4-bromo-5-methoxynaphtho[1,2-*d*]thiazol-2- amine (NTNB), whose crystal packing is described by π stacked columns connected by resonance assisted hydrogen bonding (RAHB) perpendicular to the π•••π stacking direction is analysed. The stabilizing nature of RAHB in both the NT derivatives was confirmed from IQA analysis revealing the major contribution arising from electrostatics. The RAHB dimer of crystalline NTs and the antiparallel dimer of NTNB show dipole moment minimization emphasising the importance of electrostatic dipolar interactions in customising the solid-state packing. An increase in the aromaticity of antiparallel NTNB dimer can provide a more accurate roadmap for the structural engineering of π•••π stacked organic molecules. NBO calculations were used to evaluate the stabilisation energies related to a charge-transfer interaction between the nitrogen atom's lone pair and the antibonding NH orbital in RAHB. Quantum chemical calculations and Marcus-Hush formalism in NTN revealed maximal electron and hole transfer coupling along π•••π stacked and RAHB dimers respectively. While in NTNB, higher hole and electron transfer coupling is observed along π•••π stacked dimer. Crystal engineering can be further explored as an effective approach to modulate the charge transport characteristics by achieving the precise control of RAHB and π–π stacking in π-conjugated molecules.

Contents

List of Figures

List of Tables

List of Schemes

1. Charge Transport Through Discrete Crystalline Architectures

1.1. Introduction……..……... 1

1.2. Charge Transport in Organic Semiconductors ...……..….. 2

1.2.1. Band Transport Regime……..…….……2

1.2.2. Hopping Regime…….…… 4

1.3. Molecular Packing ……..……...…….…….……... 6

1.3.1. Polymorphism…….……..... 8

1.3.2. Cocrystallization…… 9

1.3.3. Noncovalent Interaction…..…….. 10

1.3.4. Heteroatom Functionalization…….. 12

1.3.5. Orientation of the Molecule……. 12

1.3.6. Shape of the Molecule.……. 14

1.4. Aim and Objectives of the Thesis……...…….…….…. 16

1.5. References…….……..... 17

2. Atom-Efficient Halogen−Halogen Interactions Assist One-, Two-, and Three-Dimensional Molecular Zippers

2.1. Introduction…… 23

2.2. Result and Discussion……..... 24

2.3. Conclusion…… 37

2.4. Experimental Section ……..... 39

2.5 Appendix…… 41

2.6. Reference……... 47

3. The Effect of Single-Atom Substitution on Structure and Band Gap in Organic Semiconductors

3.1. Introduction……... 55

3.2. Result and Discussion……... 56

3.3. Conclusion……. 73

3.4. Experimental Section …… 75

3.5 Appendix…… 78

3.6. Reference…….. 79

4. Resonance-Assisted Hydrogen Bonding and π–π Stacking Modulates the Charge Transfer Coupling in Crystalline Naphthothiazoles

4.1. Introduction…….. 85

4.2. Result and Discussion……... 86

4.3. Conclusion…… 103

4.4. Experimental Section ……... 104

4.5 Appendix…… 106

4.6. Reference…….. 107

5. List of Publications……...… 114

6. Workshops and Conferences…….. 115

7. **Copyrights and Permissions** …….. 116

List of Figures

Figure	Title	Page
1.1	Schematic representation of a) band transport and b) hopping transport	3
1.2	a) INDO calculated electron and hole transfer integrals in a tetracene cofacial dimer by varying the intermolecular distance. b) Evolution of hole transfer integral in pentacene dimer by varying the tilt angle. Reproduced with permission from Ref. 29, Copyright 2013 Wiley VCH.	5
1.3	a) Evolution of INDO calculated electron and hole transfer integrals in a cofacial tetracene dimer by varying the degree of translation of one molecule along the long (a) and short (b) axis. Reproduced with permission from Ref . 29. Copyright 2013 Wiley VCH.	6
1.4	Schematic representation of common molecular packing modes in crystalline organic materials. Molecules having positive charge (hole) is highlighted and the near neighbours are coloured in violet. a) γ - motif with eight first neighbours, b) Herringbone arrangement with eight first neighbours, c) Sandwich herringbone arrangement with five first neighbours, d) β - motif with eight first neighbours, e) Brickwall arrangement with six first neighbours.	7
1.5	Schematic representation of a) Radial assembly, b) Helical assembly and c) Cross stacking.	8
1.6	Improved charge transport characteristics in 2:1 non-equal ratio cocrystal compared to 1:1 cocrystal and the single component crystal. Reproduced with permission from Ref. 43, Copyright 2022 Wiley VCH.	10
1.7	a) Crystalline packing in $NIBr_2OMe$ with maximal electron and hole along the halogen-halogen bonded and stacking directions. Anisotropic b) electron and c) hole mobilities along the stacking plane. Reproduced with permission from Ref. 45 Copyright 2021 American Chemical Society.	11
1.8	a) Molecular structure of $PTEBr_2$, b) schematic representation showing charge filtering in 1,7- dibromoperylene-3,4,9,10-tetracarboxylic tetrabutylester ($PTEBr_2$) Greek cross (+) aggregate. Reproduced with permission from Ref. 52, Copyright 2018 Wiley-VCH. c) orthogonally cross-stacked dimer of 6,13-dimesitylpentacene (M_2−P), d) t_e/t_h at different roational angles (α) of the pentacene dimer, Reproduced with permission from Ref. 53 Copyright 2021 American Chemical Society.	13
1.9	Schematic representation of the molecular structure of rod-type, bent-type and zigzag type organic molecules with semiconducting properties. Reproduced with permission from Ref. 55, Copyright 2014 Wiley VCH.	15
2.1	(a) T1 dimer, (b) T2 dimer, (c) 2D zipper formed from T1 and T2 dimers (BCP and RCP obtained from QTAIM analysis), (d) T3 dimer, (e) 3D zipper of NTB_2 formed from the extension of 2D zipper assisted by T3 dimer along the a-axis.	26
2.2	Angles between Br•••Br interaction in a) T1 dimer, b) T2 Dimer, C) T3 Dimer of NTB_2.	27
2.3	QTAIM electron density map showing Br•••Br interaction in T3 dimer of NTB_2.	29

2.4	NCI plot showing weak stabilizing interactions in NTB_2 zipper represented as green discs.	31
2.5	ESP Electrostatic potential in atomic units on the 0.001 isodensity surfaces of NTB_2 dimer. ESP values range from -0.03 a.u. (red) to +0.02 a.u. (blue).	31
2.6	SEM images showing the surface fiber morphology of NTB_2.	34
2.7	Tauc plot of NTB_2.	34
2.8	(a) Electronic band structure of NTB_2, HOMO and LUMO are plotted as blue and red filled circles respectively, the labeled points indicate Γ(0.0, 0.0, 0.0), R_2(0.8, −0.3, 0.2), T_2(0.0, −0.3, 0.1), U_2(0.8, −0.3, 0.0), V_2(−0.8, −0.1, 0.1), X(−0.9, −0.1, 0.0), and Y(0.0, 0.0, −0.2) positions in reciprocal space. (b) Total DOS spectrum of NTB_2 and valence orbital projected PDOS spectra of the constituent atoms from DFT calculations.	35
2.9	Total DOS spectrum of NTB_2 a) showing overlap of bromine 4p and sulphur 3p, b) PDOS spectra of p and s orbitals of Br, C, H, N and S atoms from DFT calculations.	35
2.10	(a) LUMO and (b) HOMO (isosurface value 0.02) of NTB_2. (c) Anisotropic electron and hole mobility of NTB_2 along the stacking plane. The crystallographic a-axis is taken as the reference axis, and the ac-plane as the plane of interest.	36
2.11	Anisotropic a) hole and b) electron motilities of NTB_2 along the stacking plane. Crystallographic *a*-axis is taken as the reference axis and projected on *ac* plane.	37
3.1	Crystal structure of a) NTH, b) NTC, c) NTB and d) of NTI.	57
3.2	Interactions governing packing in a) NTH, b) NTC, c) NTB and d) NTI.	59
3.3	Isostructural packing arrangements in (a) NTI and (b) NTB.	60
3.4	Molecular overlays of NTI (blue) and NTB (green).	60
3.5	Role of aromatic ring stabilization NTH.	61
3.6	Role of aromatic ring stabilization NTC.	62
3.7	Role of aromatic ring stabilization NTB.	63
3.8	Role of aromatic ring stabilization NTI.	64
3.9	Energy framework for separate electrostatic (red), dispersion (green) and total energies (blue) for (a) NTI and (b) NTB. The energy scale factor is 50.	66
3.10	Selected molecular pairs to calculate interaction energies of NTH.	66
3.11	Intermolecular interaction energies of molecular pairs (NTH).	67
3.12	Selected molecular pairs to calculate interaction energies of NTC.	67
3.13	Intermolecular interaction energies of molecular pairs (NTC).	67
3.14	Energy framework for separate electrostatic (red), dispersion (green) and total energy (blue) for a) NT and b) NTC.	68
3.15	Selected molecular pairs to calculate interaction energies of NTB.	68
3.16	Intermolecular interaction energies of molecular pairs (NTB).	69
3.17	Selected molecular pairs to calculate interaction energies of NTI.	69
3.18	Intermolecular interaction energies of molecular pairs (NTI).	69

3.19	QTAIM electron density map and NCI plot showing weak stabilizing interactions in NTC.	70
3.20	Tauc plot showing a reduction in the optical band gap of NTs from 3.48 to 3.07 eV.	71
3.21	Electronic band structure and projected density of states (states/eV) of NTH.	71
3.22	Electronic band structure and projected density of states (states/eV) of NTC.	72
3.23	Electronic band structure and projected density of states (states/eV) of a) NTB and b) NTI.	72
3.24	Close view of conduction bands from projected density of states (states/eV) of (a) NTC, (b) NTB and (c) NTI.	73
4.1	Chemical and X-ray molecular structures of (a) NTN and (b) NTNB.	87
4.2	Resonance-assisted intermolecular hydrogen bonding in NT derivatives.	89
4.3	QTAIM electron density map showing N•••H interactions in RAHB dimer of a) NTN b) NTNB and π-π stack of c) NTN d) NTNB.	90
4.4	NCI plot showing weak stabilizing interactions represented as green discs in RAHB dimers of a) NTN b) NTNB and π-π stack stacked dimers of c) NTN d) NTNB.	91
4.5	Packing arrangement in crystalline (a) NTN and (b) NTNB derivatives.	92
4.6	2-dimensional fingerprint plots showing a) total b) C•••C c) C•••H d) H•••H e) N•••H f) O•••H g) S•••H interactions in NTN.	93
4.7	2-dimensional fingerprint plots showing a) total b) C•••C c) C•••H d) H•••H e) N•••H f) O•••H g) C•••S h) Br•••H interactions in NTNB.	93
4.8	ESP maps (0.002 isodensity surface) of (a) NTN and (b) NTNB.	94
4.9	Schematic illustration of NICS probes placed at 1 Å above the centroid of each ring of monomer a) NTN b) NTNB and c) NTNH.	95
4.10	Schematic illustration of NICS probes placed at 1 Å above the centroid of each ring in RAHB dimers a) NTN and b) NTNB.	96
4.11	Schematic illustration of NICS probes placed at 1 Å above the centroid of each ring in π-π stacked dimers a) NTN b) NTNB and c) NTNH.	96
4.12	NBO plots of the donor and acceptor orbitals involved in the RAHB interaction in a) NTN and b) NTNB.	99
4.13	HOMOs (a, c) and LUMOs (b, d) of NTN and NTNB (isosurface value 0.02), respectively.	100
4.14	Anisotropic hole and electron mobilities of (a) NTN and (b) NTNB along the stacking plane. The crystallographic a axis is taken as the reference axis and is projected on the ac plane.	102

List of Tables

Table	Title	Page
2.1	Crystallographic data and refinement process for NTB_2	25
2.2	Relative % of intermolecular interactions obtained from Hirshfeld analysis.	27
2.3	Calculated topological properties of electron density function for the intermolecular interactions in crystalline NTB_2.	27
2.4	IQA interaction energies. Total noncovalent interaction energies and its components are shown. Energies are given in kcal/mol.	30
2.5	Interaction Energies of Representative NTB_2 Dimers from SAPT(0) jun-cc-pvdz Calculations[a]	32
2.6	Selected donor-acceptor natural bond orbital interactions with their corresponding second-order perturbation stabilization energies in T1, T2 and T3 dimes of NTB_2. Energies are given in kcal/mol.	33
2.7	Magnitudes of dipole moments for adjacent dimers in the crystal packing of NTB_2.	33
2.8	Electron and hole reorganization energy ($\lambda_{e/h}$) and charge transfer coupling values ($V_{e/h}$) of selected dimers of NTB_2.	36
3.1	Crystallographic data and refinement process for NT derivatives.	58
3.2	Relative % of intermolecular interactions obtained from Hirshfeld analysis.	59
3.3	List of strong and moderate aromatic interactions in NTH using aromatic analyzer component in Mercury 4.0.	62
3.4	List of strong and moderate aromatic interactions in NTC using aromatic analyzer component in Mercury 4.0.	63
3.5	List of strong and moderate aromatic interactions in NTB using aromatic analyzer component in Mercury 4.0.	64
3.6	List of strong and moderate aromatic interactions in NTI using aromatic analyzer component in Mercury 4.0.	65
3.7	Magnitudes of dipole moments (Debye) for monomer and antiparallel stacked dimers in the crystal packing of NTs.	70
3.8	Calculated topological properties of electron density function for the intermolecular interactions in crystalline NTC.	70
3.9	IQA interaction energies. Total noncovalent interaction energies and its components of NTC are shown. Energies are given in kcal/mol.	71
4.1	Crystallographic data and refinement parameters for NTN and NTNB.	88
4.2	Calculated topological properties of electron density function for the intermolecular interactions in crystalline NTN and NTNB.	90
4.3	IQA interaction energies. Total noncovalent interaction energies and its components of NTN and NTNB are shown. Energies are given in kcal/mol.	91

4.4	Interaction energies of representative NTN and NTNB hydrogen bonded dimers from SAPT(0) aug-cc-pvdz calculations.	92
4.5	Relative % of intermolecular interactions obtained from Hirshfeld analysis for NTN and NTNB.	94
4.6	Magnitudes of dipole moments (Debye) for monomer and different dimers in the crystal packing of NTN and NTNB.	95
4.7	$NICS_{zz}$ (1) calculated for NTN monomer and RAHB dimer. a, b, and c represent the rings in monomer and a', b', and c' represent the corresponding rings in the dimer. $NICS_{zz}$ (1) units are in ppm. $\Delta NICS_{ZZ}$ (1) = $NICS_{ZZ}$ (1) (dimer) – $NICS_{ZZ}$ (1) (monomer).	97
4.8	$NICS_{zz}$ (1) calculated for NTNB monomer and RAHB dimer.	97
4.9	$NICS_{zz}$ (1) calculated for monomer and parallel π-π stacked dimer of NTN.	97
4.10	$NICS_{zz}$ (1) calculated for NTNB monomer and antiparallel π-π stacked dimer.	98
4.11	$NICS_{zz}$ (1) calculated for monomer and antiparallel π-π stacked dimer of NTNH.	98
4.12	Selected donor-acceptor natural bond orbital interactions with their corresponding second-order perturbation stabilization energies of N-H•••N RAHB dimers in NTN and NTNB. Energies are given in kcal/mol.	98
4.13	Electron and hole transfer coupling values of selected dimers of NTN and NTNB.	100
4.14	The hole and electron reorganization energy of NTN and NTNB.	101
4.15	The theoretically predicted hole and electron mobility of NTN and NTNB.	101

List of Schemes

Scheme	Title	Page
2.1	Schematic representation of (a) Type I trans (b) Type I cis, and (c) Type II dihalogen interactions. (d) Chemical structure of NTB_2.	24
2.2	Reaction scheme for the synthesis of NTB_2.	24
3.1	Chemical structure and schematic representation of modulation in band gap via halogenation in 5- Methoxynaphtho[1,2-*d*]thiazole.	56
3.2	Reaction scheme for the synthesis of NTH, NTC, NTB and NTI.	57
4.1	Reaction scheme for the synthesis of NTN (3) and NTNB (4).	87

Chapter 1

Charge Transport Through Discrete Crystalline Architectures

1.1. Introduction

Organic π-conjugated materials exhibit remarkable potential as active elements in optoelectronics and have advanced significantly over the past few decades with promising applications in light-emitting diodes,[1] photovoltaics,[2] and field-effect transistors.[3] Charge transport at the molecular level is significantly influenced by the electronic coupling and the reorganization energy.[4] The electronic coupling ($V_{e/h}$) of an organic scaffold is highly dependent on the molecular arrangements in its crystal lattice, as $V_{e/h}$ determines the extent of overlap of the frontier orbitals involved in charge transport.[5] Rational modulation of noncovalent intermolecular interactions for crystal engineering is as crucial as the covalent bond for molecular synthesis.[6] Noncovalent interactions emanating from the introduction of heteroatoms can alter the crystalline packing of organic chromophores and significantly influence the charge transport properties.[7] Exploring the correlation between diverse crystalline packing morphologies adopted by organic chromophores and charge transport properties from a crystal engineering perspective including intermolecular interactions and molecular structure is a significant area of research for the design of advanced functional materials.

Unlike their inorganic counterparts, organic semiconducting solids are forged by relatively weaker noncovalent interactions, manifesting a wide bandgap and distinct charge transport mechanism. An in-depth understanding of how subtle changes at the molecular level could alter the crystal packing and charge transport properties holds paramount importance in devising efficient organic semiconducting materials. Therefore, comprehending the processes that determine charge transport significantly impacts designing materials with enhanced structure-property relationships. Different approaches are used to experimentally measure the charge carrier

mobility including time-of-flight (TOF) technique,[8,9] field-effect transistor configuration,[10] Hall effect mobility,[11] space charge limited current techniques,[12] method of charge extraction by linearly increasing voltage[13,14] and time-resolved microwave conductivity measurements.[15] A comprehensive analysis of the above-mentioned experimental techniques is explained in-depth in comprehensive reviews on this topic.[4,10,16]

1.2 Charge Transport in Organic Semiconductors

The primary characteristic describing charge transport properties in a semiconductor is the charge carrier mobility, μ, ($cm^2V^{-1}s^{-1}$), defined as the ratio between the drift velocity of charge carriers ν, induced by an external electric field, and the amplitude of the external electric field, F, (Vcm^{-1}).[4]

$$\mu = \frac{\nu}{F}$$

Charge carrier mobility is influenced by the material's intrinsic properties (molecular structure and packing), extrinsic properties (types of defects present and their concentration), and external factors (temperature and electric field).[17] The long standing disputes of charge transport in organic crystals arise from the conflict between the localized/delocalized transport descriptions, as they extrapolate at two opposing extrema. The mechanism of charge transport is generally categorized into three regimes[18,19] based on the localization of the charge carriers and magnitude of electron-phonon interaction: i) Boltzmann band model based on delocalized coherent transport of free charge carriers with the intermolecular electronic coupling (V) significantly larger than the molecular reorganization energy (λ); ii) intermediate regime where V is comparable to λ and iii) Hopping model where electron interacts strongly with lattice vibrations leading to localized incoherent transport with V considerably lower than λ.

1.2.1 Band Transport Regime

Bloch theorem is the cornerstone of band theory, describing the general nature of an electron orbital in a periodic potential as plane waves modified by periodic functions (Figure 1a).[20] The electron and hole mobilities in the band regime are derived from the widths and shapes of conduction and valence bands of the material built from the interaction of the HOMO and LUMO levels. Mobility of charge carrier in the band transport regime is given by:

$$\mu = q\tau\frac{1}{m^*}$$

where q is the elementary charge, m* effective mass of the charge carrier, and τ is the mean relaxation time between collisions. Band theory is in principle used to describe transport in defect-free ultrapure organic semiconductors in a low temperature limit. The effective mass and the relaxation time are the two factors in band theory that require computational evaluation to determine the mobility. An enhancement in thermally activated transport is observed with increase in temperature, on account of charge localization due to band narrowing. Understanding the exact mechanism of charge transport through organic molecular structures remains elusive. Predicting the transport regime based on the localized or delocalized nature of charge carrier might not hold true in every cases. Instead, there are cases where organic solids adhere to charge transport mechanisms, neither being localized at a site, nor completely delocalized in the carrier band, owing to the interplay between electron-phonon coupling and electronic coupling giving rise to an intermediate regime.

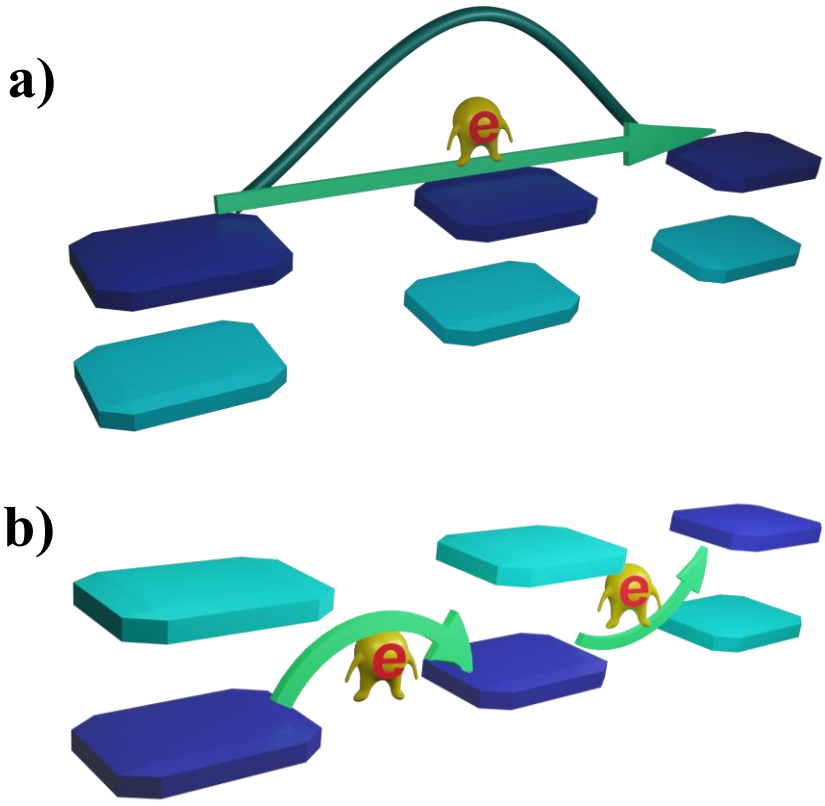

Figure 1.1: Schematic representation of a) band transport and b) hopping transport.

1.2.2 Hopping Regime

At higher temperatures, organic crystals undertake the opposite limiting regime in terms of charge carrier transport, ie. polaronic or hopping transport. The models presume the charge carriers are localised on a site and moves through the materials by discrete jumps from one site to another (Figure 1b).[21] Hopping drift mobility is calculated employing Einstein relation:

$$\mu = \frac{e}{k_B T} D$$

where D is the diffusion coefficient, k_B is the Boltzmann constant and T is the temperature. The hopping rate (k_i) of the charge carriers can be calculated employing the Marcus-Hush expression:[22]

$$k_i = \frac{{V_{e/h}}^2}{\hbar}\left(\frac{\pi}{\lambda_{e/h} k_B T}\right)^{\frac{1}{2}} exp\left(-\frac{\lambda_{e/h}}{4 k_B T}\right)$$

where V is the intermolecular electronic coupling and λ is the reorganization energy. According to Marcus theory, two major parameters determine the efficient carrier mobility, i) electronic coupling (transfer integral) between adjacent molecules should be maximum, and ii) reorganization energy should be minimum.

Reorganization energy (λ) consists of internal as well as external contributions. The changes in the surrounding media accompanying charge transfer are considered as an external contribution and are often forsaken by theoretical simulations. In contrast, the internal contribution towards reorganization energy (0.07 – 0.18 eV)[17] corresponds to the total change in geometry relaxation energies occurring when a molecule goes from its neutral state to charged state geometry, including change in molecular rigidity, degree of freedom, conjugation lengths, etc. Yet another crucial parameter for evaluating charge hopping rate is the transfer integral (V). V is related to the degree of electronic coupling associated with the orbital wave function overlap between HOMO (for holes) and LUMO (for electrons) levels of the adjacent molecules ($10 \leq V \leq 100$ meV) and is firmly persuaded by the chemical structure of the molecule, molecular packing motif, π-π stacking distance.[17] According to the Marcus-Hush equation, small reorganization energy and a significant transfer integral are advantageous for accelerating the charge transfer rate. Consequently beneficial for computational screening of candidates with high hopping carrier mobility in organic

semiconductors. The magnitude of electronic coupling V_{ab} between two molecular orbitals Ψ_a and Ψ_b residing on neighboring molecules is defined by the matrix element:

$$V_{ab} = < \Psi_a | H | \Psi_b >$$

where H is the one electron hamiltonian of the system and the value of V_{ab} can be evaluated explicitly[23] or by employing the energy splitting method.[5] Theoretical calculations reveal that both reorganization energy and transfer integral are substantially influenced by the molecular structure and accompanying supramolecular organization in the solid-state.[24,25] With increasing tilt angle and π-π stacking distance, the transfer integral significantly decreases due to the breakdown of electronic coupling and intermolecular interactions (Figure 1.2). Also, wavefunction overlap and electronic coupling are reduced as a result of the displacement of molecules along short and long axis.[26,27] Considering the hole transport in tetracene as an example, it was observed that charge transfer integral improved when the interaction between the π orbitals are both antibonding or bonding interactions and lowered when there is a cancellation between them. This finding suggests to ensure high performance of organic semiconductor crystals with efficient charge transport, optimal π-atomic orbital overlap is more crucial than merely maximizing the cofacial overlap (Figure 1.3a,b).[24,28] As molecular packing is often governed by intermolecular noncovalent

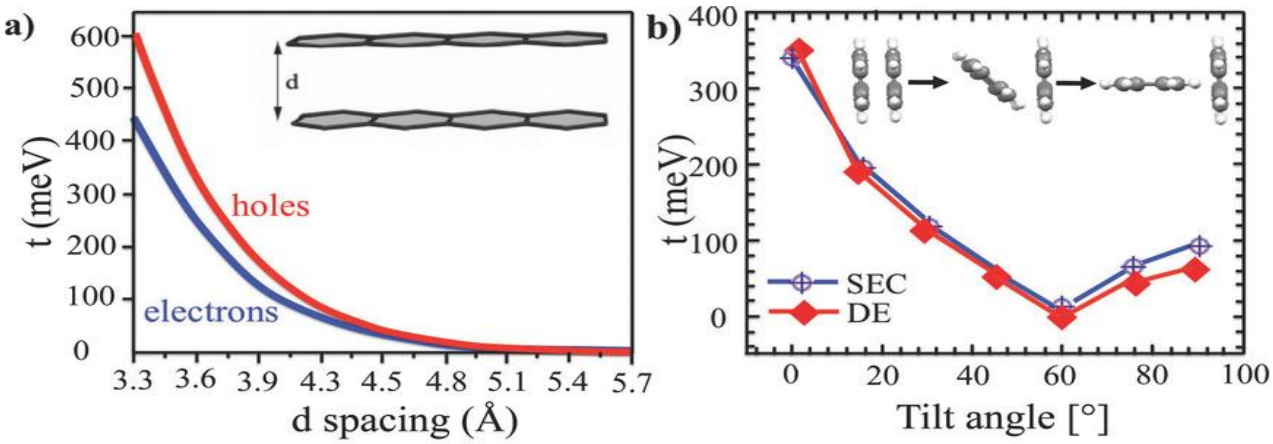

Figure 1.2: a) INDO calculated electron and hole transfer integrals in a tetracene cofacial dimer by varying the intermolecular distance. b) Evolution of hole transfer integral in pentacene dimer by varying the tilt angle. Reproduced with permission from Ref. 29, Copyright 2013 Wiley VCH.

interactions, designing molecules with effective orbital overlap depends on the electronic structure of the molecule as well as the presence of strong and long-range intermolecular interactions.[29]

1.3. Molecular Packing

The fundamental requirements for producing high-performance organic semiconductors from the perspective of molecular design are densed molecular packing with maximal π-atomic orbital overlap and adequate electronic structures comprising of energy gap and alignment.

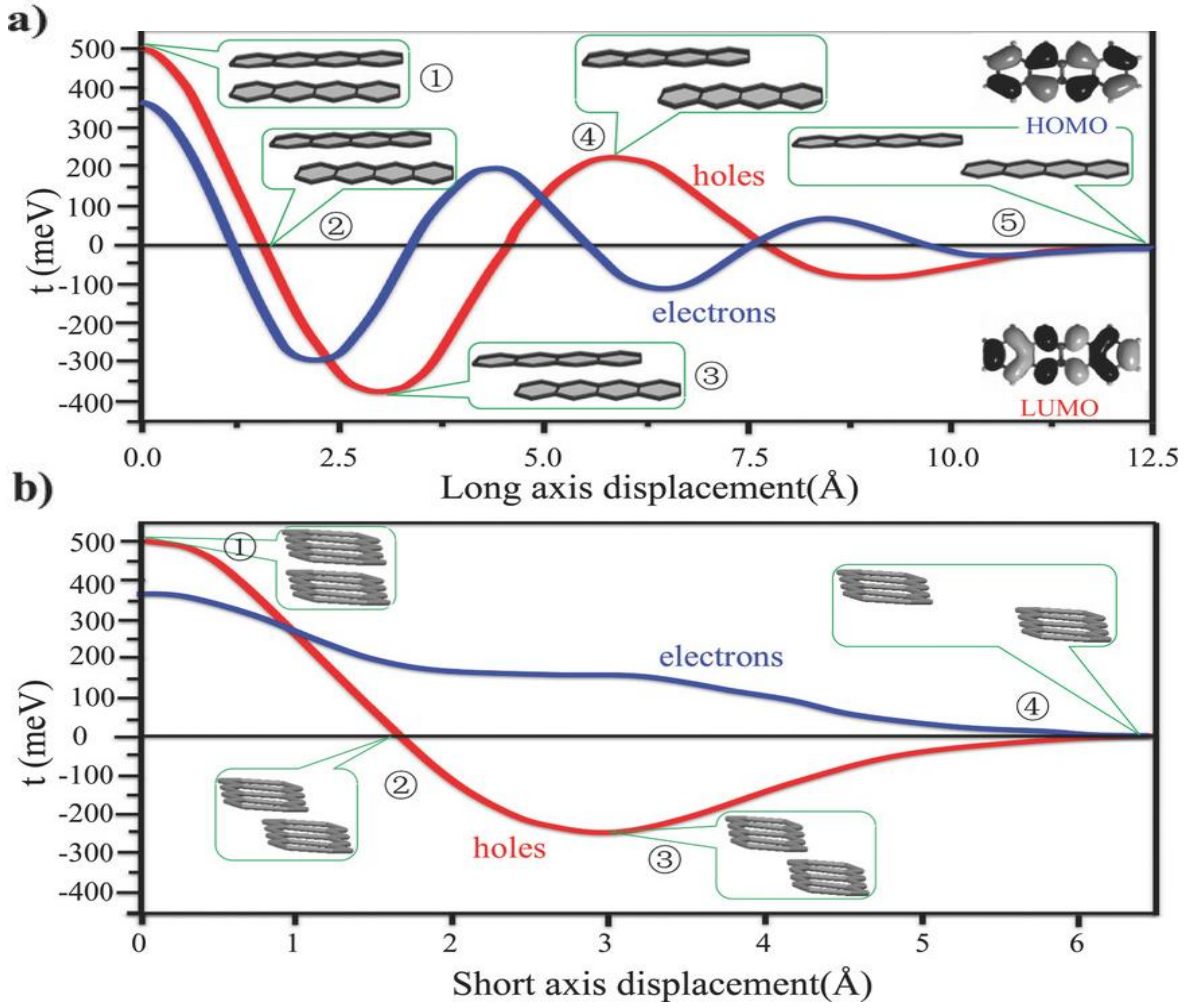

Figure 1.3: a) Evolution of INDO calculated electron and hole transfer integrals in a cofacial tetracene dimer by varying the degree of translation of one molecule along the long (a) and short (b) axis. Reproduced with permission from Ref. 29, Copyright 2013 Wiley VCH.

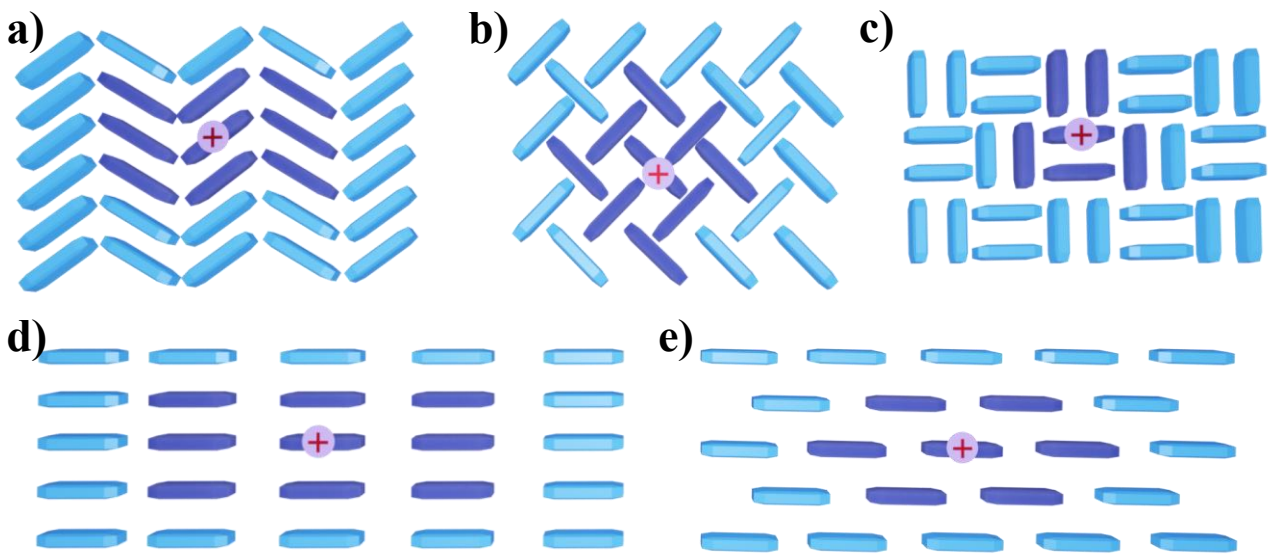

Figure 1.4. Schematic representation of common molecular packing modes in crystalline organic materials. Molecules having positive charge (hole) is highlighted and the near neighbours are coloured in violet. a) γ - motif with eight first neighbours, b) Herringbone arrangement with eight first neighbours, c) Sandwich herringbone arrangement with five first neighbours, d) β - motif with eight first neighbours, e) Brickwall arrangement with six first neighbours.

Representative crystalline motifs in polycyclic aromatic hydrocarbons based on the edge-to-face (herringbone and sandwich herringbone) and face-to-face (γ-motif, β-motif, and brickwork) noncovalent interactions[30] are summarized in figure 1.4. Among all the packing modes, the one with the highest π-π stacking is regarded to be the most efficient motif for charge transport, because large π-π overlap stabilizes the charged state and allows the efficient propagation of charge carriers. Inclusion of radial, cross-staked and helical packing motifs to the traditional taxonomy of crystalline supramolecular motifs opens door for the identification of novel crystalline motifs with emergent properties (Figure 1.5).[31] Extensive research has been employed to obtain facile and efficient routes for transporting charges from one molecule to its adjacent molecule. In this thesis we highlight the different strategies adopted to modulate the crystalline packing in organic scaffolds for efficient charge transport including i) polymorphism, ii) heteroatom function-alization, iii) noncovalent interactions iv) cocrystallization v) orientation and vi) shape of the molecule.

1.3.1. Polymorphism

Polymorphism is crucial to explore the fundamental relationship between crystal packing and charge transport without altering the molecule's chemical structure since small changes in the crystal packing can significantly influence the mobility of the charge carriers.[32] Benchmark organic semiconductors like pentacene, TIPS-pentacene, rubrene, and sexithiophene are polymorphic. Quantum chemical calculations were performed on slip-stacked (I) and γ-herringbone (II) polymorphs of 6,13-Bis(trimethylsilylethynyl)pentacene (TMS-pentacene).[33] The structural difference among polymorphs I (P1) and II (P2) was observed in the weak intermolecular interactions linking the adjacent π-stacks and the π-π stacking distance. C-H•••H-C interactions dictate the edge-to-face γ-herringbone motif, while C-H•••π interactions facilitate face-to-face

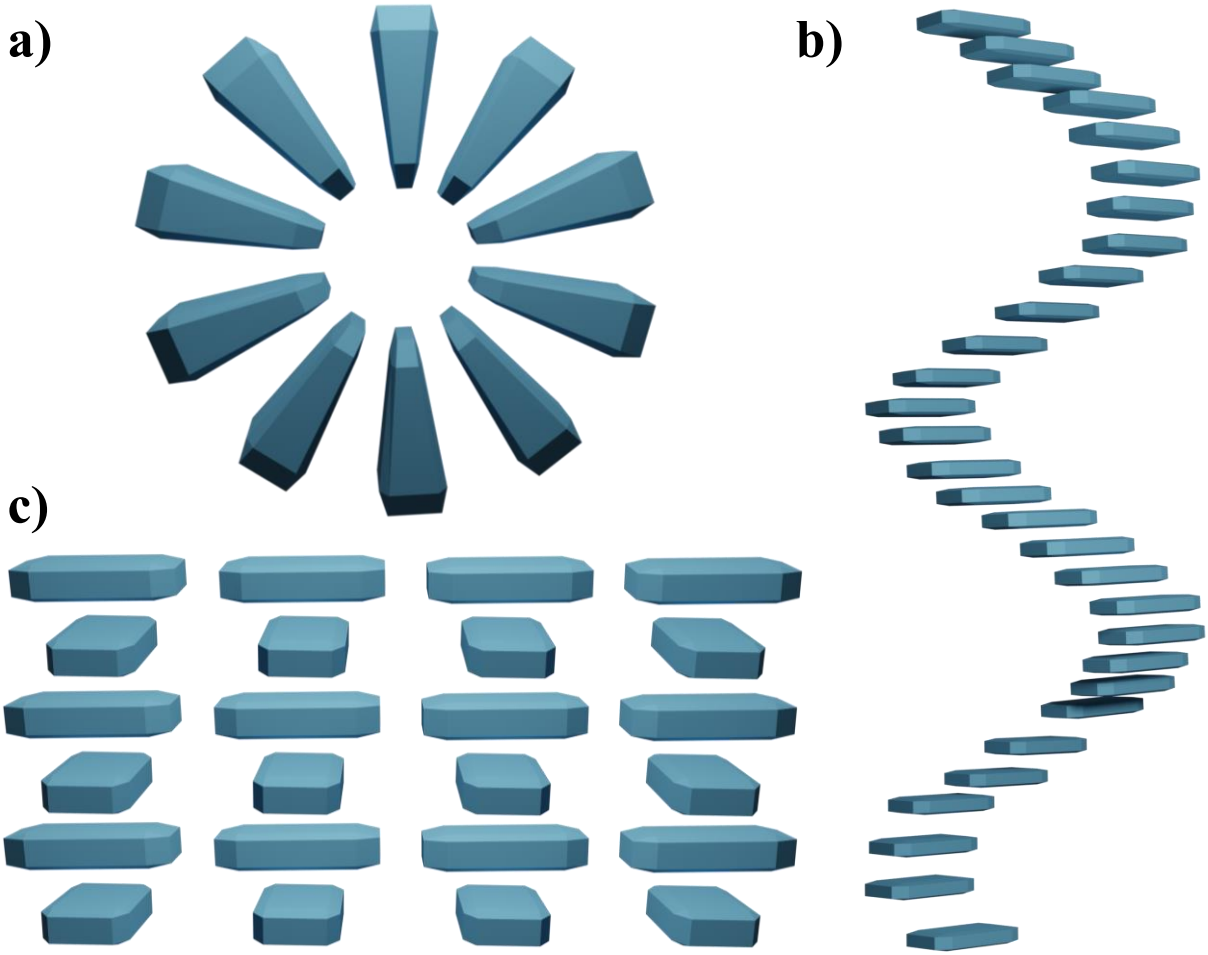

Figure 1.5. Schematic representation of a) Radial assembly, b) Helical assembly, and c) Cross stacking.

packing in the slip-stacked motif. The interplanar distance in P1 was found to be 3.4 Å, whereas P2 displayed two different π-π distances of 3.3 and 3.5 Å. The theoretical electronic coupling and anisotropic mobility calculations indicate enhanced hole mobility (μ_h = 3.7 $cm^2V^{-1}s^{-1}$) in P2 compared to P1 (μ_h = 0.1 $cm^2V^{-1}s^{-1}$). Theoretical[34] and experimental[35] assays on peri-substituted pentacenes demonstrating ambipolar charge transport are further validated by P2's substantial hole and electron mobility. Although polymorphism considerably reduces the variables influencing charge transport, more strategies are still adopted to tweak the molecular packing and the charge transfer coupling in crystalline organic molecules.

1.3.2. Cocrystallization

Cocrystallization is a vital crystal engineering technique where two or more organic molecules are stoichiometrically merged and held together by noncovalent intermolecular interactions.[36] Heeger's discovery of a two-component cocrystal of tetrathiafulvalene-7,7,8,8-tetracyanoquinodimethane (TTF-TCNQ) displaying remarkable conductivity, sparked a flurry of interest in the study of multicomponent materials.[37] Since then, organic cocrystals have been noted to exhibit versatile properties, including ambipolar charge transport,[38] ferroelectricity,[39] room-temperature phosphorescence,[40] etc. The intermolecular packing of donor-acceptor (DA) cocrystals significantly affects the transport properties, as segregated stacking exhibit ambipolar electrical conductivity and mixed stacking yields ferroelectric behavior.[41] A series of TTF-TCNQ-based cocrystals were examined to study the crystalline packing and corresponding structure-packing-property relationship. The mixed stacked DA systems possess higher lattice energy than the segregated stacking.[42] Regardless of the packing mode, the energy decomposition analysis (PIXEL) showed that the dispersion component, as opposed to the Coulombic and polarization components, contributed significantly towards the lattice stability. Band structure and density of states calculations of prototypical cocrystals centered on TTF-TCNQ model systems divulged metallic and semiconductive properties for the segregated and mixed stack cocrystals, providing clear evidence for D-on-D and A-on-A segregated architectures' innate enhanced charge transport potential. The packing in organic semiconductors can be customized by utilizing non-equal ratio cocrystallization resulting in improved charge transport properties than the single component and 1:1 ratio cocrystal. Cocrystals IC2-DPAO and ICFO with 2:1 and 1:1 ratios were constructed using a model compound indolo[2,3-a]carbazole (IC), and 9-fluorenone (FO) and 2,6-

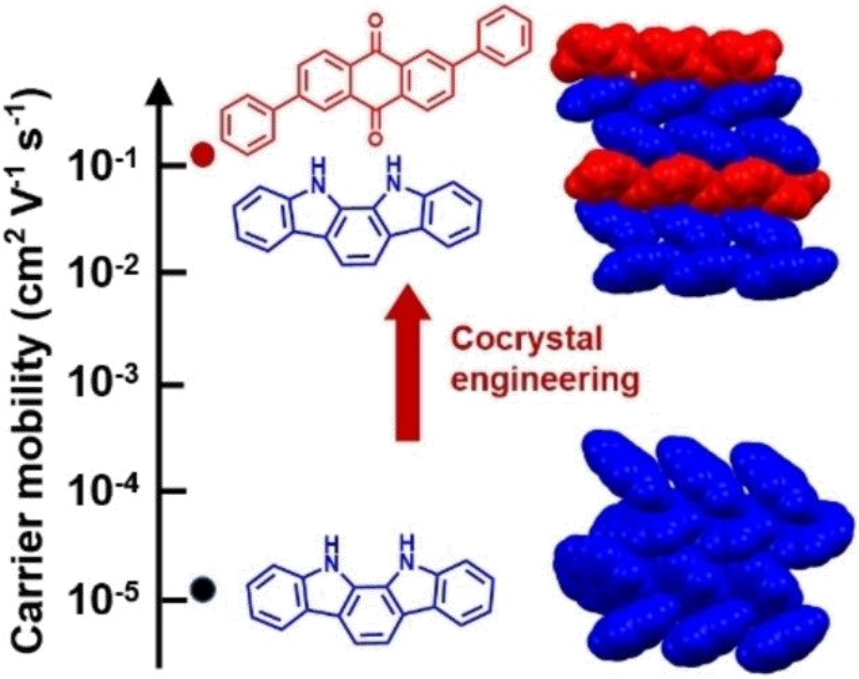

Figure 1.6. Improved charge transport characteristics in 2:1 non-equal ratio cocrystal compared to 1:1 cocrystal and the single component crystal. Reproduced with permission from Ref. 43, Copyright 2022 Wiley VCH.

diphenylanthraquinone (DPAO) coformers (Figure 1.6).[43] The herringbone packing in the parent IC crystal is retained in the segregated stack IC2-DPAO cocrystal, while in the segregated IC-FO cocrystal, IC adopts a slipped packing motif. The improved carrier mobility in the 2:1 ratio IC2-DPAO cocrystal is attributed to the herringbone packing with a double-channel charge transport network. The strong electronic coupling and modest hole effective mass revealed by DFT calculations agree with the measured carrier mobility in IC2-DPAO, highlighting the significance of non-equal ratio cocrystal engineering to achieve packing structures conducive for charge transport.

1.3.3. Noncovalent Interactions

Specific directional interactions nurture the formation of supramolecular synthons that hierarchically assemble to form the crystalline architecture with remarkable functional properties.[44]

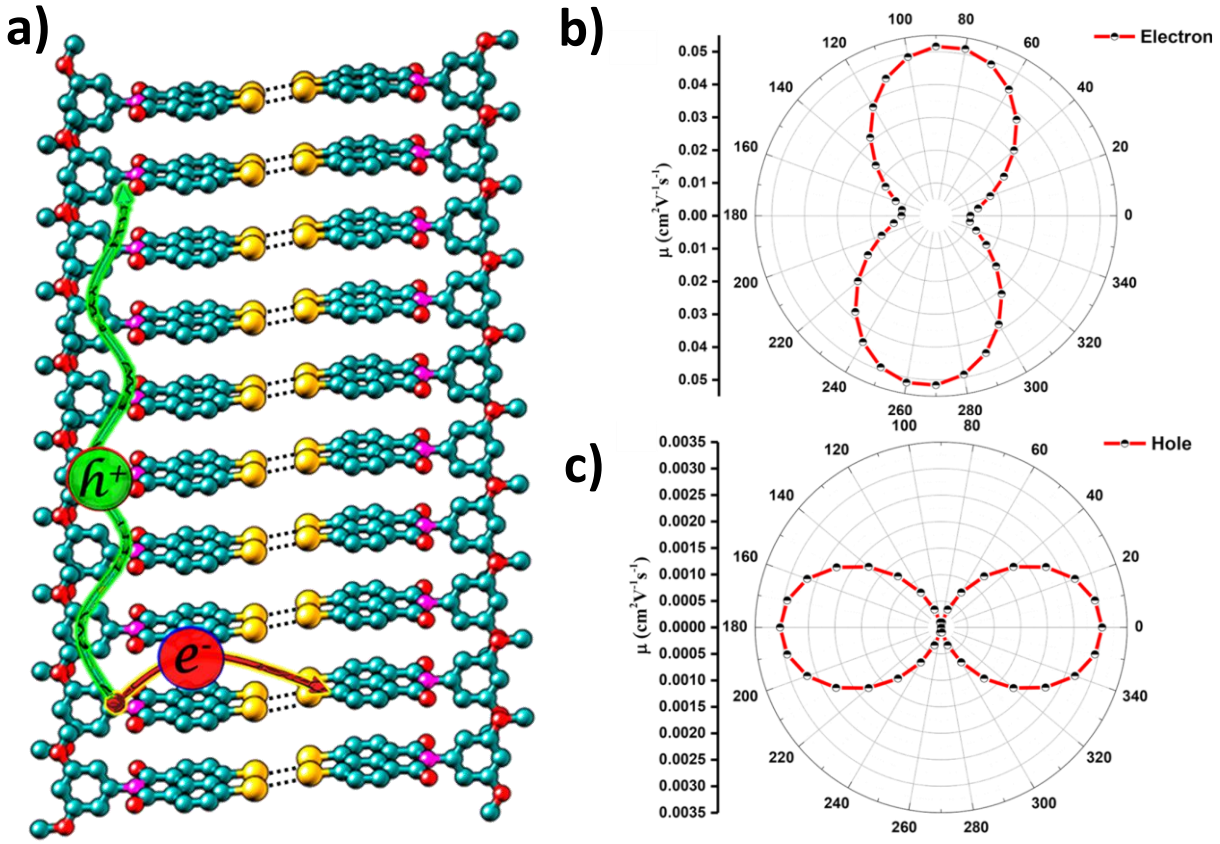

Figure 1.7. a) Crystalline packing in $NIBr_2OMe$ with maximal electron and hole mobilities along the halogen-halogen bonded and stacking directions. Anisotropic b) electron and c) hole mobilities along the stacking plane. Reproduced with permission from Ref. 45, Copyright 2021 American Chemical Society.

The crystal structure analysis of 1,8-dibromonaphthalene(3,5-dimethoxyphenyl)imide ($NIBr_2OMe$) revealed parallelly ordered segregated stacks stabilized by a parallelogram-type Br_4 synthon.[45] In addition to the peri-peri halogen-halogen interactions, the arrangement of the DA molecules with HOMO/LUMO localized on the donor/acceptor parts causes maximum hole mobility along the stacking direction and a maximum electron mobility perpendicular to this direction, boosting orthogonal charge carrier transport (Figure 1.7). The orthogonal channels for the maximal hole and electron transport predicted by the theoretical calculation of anisotropic mobility are advantageous for the directional screening of charge carriers suitable for device applications. Hydrogen bonds, in addition to halogen bonds have the potential to modulate the packing to alter the charge transport properties. Biological conductors like DNA,[46] natural dyes[47] and oligopeptides[48] utilize hydrogen bonds to instruct multivalent interactions stabilized by π•••π

interactions. Two crystal polymorphs of ellipticine are used to investigate the charge transport properties of the molecular assembly driven by hydrogen bonding and π•••π stacking.[49] Low dihedral angle, wavefunction delocalization across the hydrogen bonding moieties and a short distance between the hydrogen bonding pair are attributed to the increase in charge transfer integral along the hydrogen bonded channel in the polymorphs. Fabricating field-effect transistors demonstrated the experimental validation of long-range charge transport through the hydrogen bonds spanning micron-length scales.

1.3.4. Heteroatom Functionalization

The discrete packing arrangements in organic chromophores are dictated by numerous noncovalent interactions. Introduction of heteroatom to hydrocarbon backbone can induce change in condensed phase architecture by creating additional interactions. Consequently, heteroatom doping will have an impact on the charge transport properties in chromophoric assemblies. Nitrogen doping in wing-shaped tetrabenzoacene (TBA) derivatives has reduced the interplanar distance through N•••C interactions.[50] Theoretical charge transport properties carried out in distinct molecular dimer of dopped TBA derivatives through pitch and roll displacement unveiled the capability of slip-stacked dimeric arrangements to exhibit efficient charge transport. A series of propeller shaped para-substituted triphenylamine (TPA) derivatives have been examined to understand the correlation between crystalline packing and charge transport properties by tuning the substituent groups connected to the core.[51] TPA moiety is predicted to have weak electronic coupling due to the poor orbital overlap imposed by the propeller shape of the TPA core. Among the TPA derivatives TCN possessed the highest hole mobility as a result of low value of hole reorganization energy (0.073 eV) and gamma packing arrangement. Cyanation promoted π-stacking between neighbouring molecules and thereby improved the electronic coupling between them. The study provides insights into developing better TPA hole transport materials for optoelectronic applications.

1.3.5. Orientation of the Molecule

Molecular organization in the condensed phase of organic chromophores have proven pivotal in recognizing efficient optoelectronic and photonic materials. The constituent parts of a molecular framework are anticipated to communicate in a myriad of ways. Therefore, distinctive orientation

manifested by aggregated or crystalline structure have a persuasive effect on the functional properties, including charge transport and optoelectronic characteristics. Hariharan and coworkers demonstrated an ideal Greek cross (+) chromophore array in crystalline $PTEBr_2$ with an orthogonally stacked arrangement of the molecules ($\alpha = 90°$) (Figure 1.8a).[52] Convex and concave types of dimers were created by the perpendicularly cross-stacked columns, which were determined by π•••π interactions and C•••Br and Br•••O interactions, respectively. The 2D crystalline packing in $PTEBr_2$ was driven by C-H•••O and C-H•••π interactions. Theoretical calculation of charge transport properties showed selective hole mobility ($\mu_h/\mu_e = 575.8$) in $PTEBr_2$, that can be

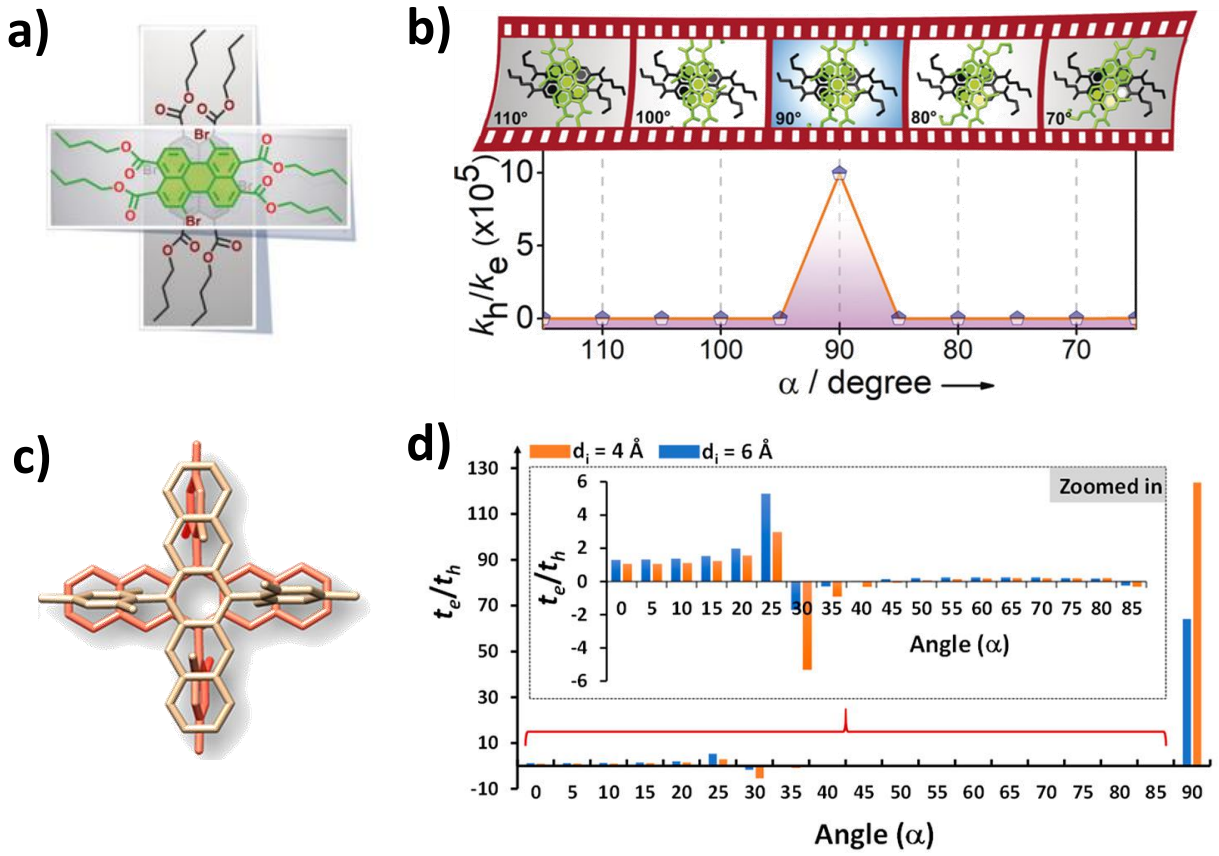

Figure 1.8. a) Molecular structure of $PTEBr_2$, b) Schematic representation showing charge filtering in 1,7-dibromoperylene-3,4,9,10-tetracarboxylic tetrabutylester ($PTEBr_2$) Greek cross (+) aggregate, Reproduced with permission from Ref. 52, Copyright 2018 Wiley-VCH. c) Orthogonally cross-stacked dimer of 6,13-dimesitylpentacene (M_2−P), d) t_e/t_h at different roational angles (α) of the pentacene dimer, Reproduced with permission from Ref. 53 Copyright 2021 American Chemical Society.

exploited to design materials with charge filtering phenomenon (Figure 1.8b). Additionally, the same group has reported a number of 6,13-bisaryl substituted pentacene derivatives that form distinctive Greek cross (+)-architecture with appreciable interchromophoric separation (d_i = 4.74−5.99 Å) in the solid state (Figure 1.8c).[53] The crystalline assembly is dictated by the intermolecular C-H•••C noncovalent interactions between the pentacene backbone and aryl substituents. The pentacene cross-stacks bestow preferential electron- transfer coupling at a fairly short interchromophoric distance (d_i < 5 Å). The HOMO of the molecule has a node along its long molecular axis, hindering HOMO-HOMO overlap and reducing the hole-transfer coupling. The orthogonal cross-stacked orientation has the highest t_e/t_h value compared to the minimal t_e/t_h at other angles (Figure 1.8d). Following the observation of charge filtering in orthogonally cross-stacked molecular systems, a comprehensive theoretical analysis of the electronic coupling characteristics as a function of rotational angle in stacked acenes was probed by Hariharan And coworkers, allowing multiple possibilities of molecular arrangement through rotational motion. In the series of (4n+2) π-electronic acene system, those having odd and even number of benzenoids exhibits exclusive electron transfer and hole transfer coupling, respectively in its Greek cross alignment. The gerade symmetric orbitals exhibit zero inter-orbital overlap, resulting in the deactivation of hole or electron transfer coupling in orthogonally cross-stacked acenes. Consequently, irrespective of molecular candidate, a mutually exclusive hole and electron transfer coupling is observed in the Greek cross orientation.

1.3.6. Shape of the Molecule

The correlation between the properties of individual molecules and its close packed structure is far from trivial. The charge carrier transport in supramolecular assemblies gets disrupted since the molecules are perpetually in thermal motion due to the weak intermolecular interactions.[54] The small radii of rotation and translation in linear and quasi-linear molecules makes them susceptible to high degree of molecular motion with temperature. This limits the potential of the linear and quasi-linear molecules in organic solar cells (OSCs). Hence, reduction of unfavorable motions should be considered as a salient parameter along with the molecular characteristics and intermolecular orbital overlap for the future rational design of organic semiconductors (Figure 1.9).[55] The conceptually new bent-shaped π cores possess high radii of rotation and translation can

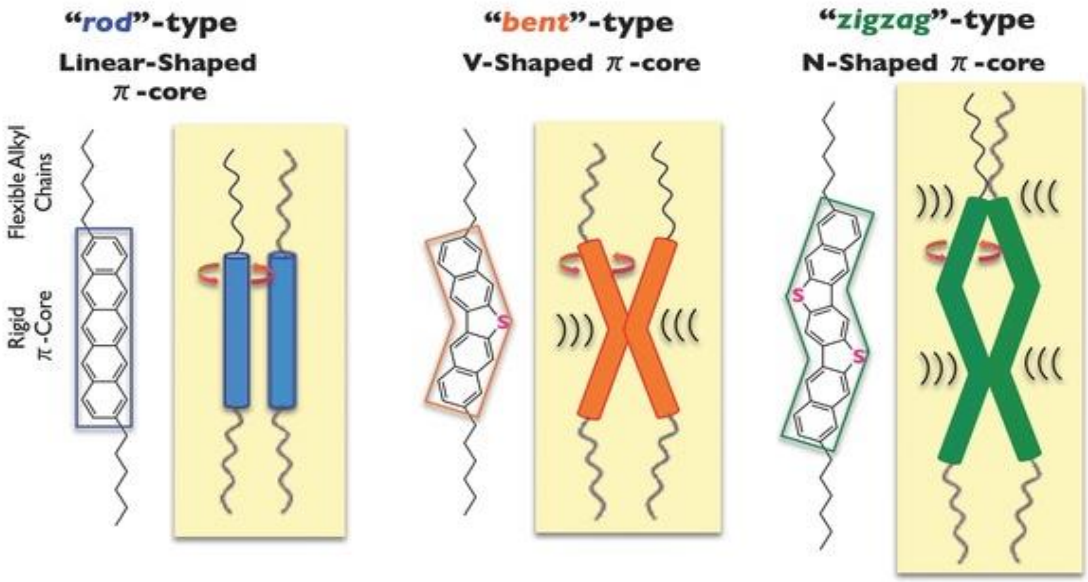

Figure 1.9. Schematic representation of the molecular structure of rod-type, bent-type and zigzag type organic molecules with semiconducting properties. Reproduced with permission from Ref. 55, Copyright 2014 Wiley VCH.

be used in future OSC since it meets the prior mentioned requirements. Takeya and coworkers have validated the versatility of bent shaped OSCs by probing the electronic properties of a series of nonlinear aromatic cores. Theoretical simulations of transfer integrals and effective masses indicate favorable charge transport features that hold promise for high carrier mobility (μ). Thermal investigations indicate that the bent-shaped OSCs are thermally stable, and their crystal phases are thermally robust, allowing them to be manufactured at high temperatures. In comparison to traditional linear and quasilinear OSCs, bent-shaped OSCs offer distinct benefits in terms of achieving high-performance and resilient OSCs for future practical applications.

.

1.4. Aim and Objectives of the Thesis

π-Conjugated materials are excellent candidates for novel organic optoelectronic devices driven by molecular design. Molecular packing in organic crystals significantly affects the charge transport properties but is difficult to predict because of the intricate intermolecular interactions. Crystal engineering essentially aims to comprehend intermolecular interactions in the framework of crystal packing and design novel molecules for the fabrication of functional materials. In this thesis we attempt to identify characteristic charge transport properties in functional crystalline solids arising as a function of molecular structure, orientation, intermolecular interactions and packing arrangements. Different strategies including polymorphism, cocrystallization, directional interactions, heteroatom doping, orientation of the chromophore and shape of the molecule can be exploited to modulate the packing motifs in organic crystals thereby alter the charge transport properties of the system. Small variations in the molecular packing can result in considerable changes in charge carrier mobilities because of which modulating the shape of the molecule is emerging as a cutting-edge design method for tweaking charge transport parameters in the burgeoning area of organic electronics. Chapter 2 showcases how multivalent interactions of bromine cultivate type I, type II, and a near orthogonal halogen-halogen interactions forging aesthetic 1D-, 2D-, and 3D-zipper assembly in angular napthothiazoles. Halogenated isostructural napthothiazole crystals exhibiting a reduction in optical band gap with an increase in atomic number is explored in chapter 3. Engineering of crystal packing in angular naphthothiazoles upon bromine substitution facilitating selective charge transfer coupling along π-π stacking direction is discussed in chapter 4.

1.5. References

(1) Burroughes, J. H.; Bradley, D. D. C.; Brown, A. R.; Marks, R. N.; Mackay, K.; Friend, R. H.; Burns, P. L.; Holmes, A. B. Light-Emitting Diodes Based on Conjugated Polymers. *Nature* **1990**, *347*, 539–541.

(2) Sariciftci, N. S.; Smilowitz, L.; Heeger, A. J.; Wudl, F. Photoinduced Electron Transfer from a Conducting Polymer to Buckminsterfullerene. *Science* **1992**, *258*, 1474–1476.

(3) Sirringhaus, H.; Brown, P. J.; Friend, R. H.; Nielsen, M. M.; Bechgaard, K.; Langeveld-Voss, B. M. W.; Spiering, A. J. H.; Janssen, R. A. J.; Meijer, E. W.; Herwig, P.; de Leeuw, D. M. Two-Dimensional Charge Transport in Self-Organized, High-Mobility Conjugated Polymers. *Nature* **1999**, *401*, 685–688.

(4) Coropceanu, V.; Cornil, J.; da Silva Filho, D. A.; Olivier, Y.; Silbey, R.; Brédas, J. L. Charge Transport in Organic Semiconductors. *Chemical Reviews* **2007**, *107*, 926–952.

(5) Brédas, J. L.; Calbert, J. P.; Da Silva Filho, D. A.; Cornil, J. Organic Semiconductors: A Theoretical Characterization of the Basic Parameters Governing Charge Transport. *Proceedings of the National Academy of Sciences of the United States of America* **2002**, *99*, 5804–5809.

(6) Yu, P.; Zhen, Y.; Dong, H.; Hu, W. Crystal Engineering of Organic Optoelectronic Materials. *Chem* **2019**, *5*, 2814–2853.

(7) Ramakrishnan, R.; Niyas, M. A.; Lijina, M. P.; Hariharan, M. Distinct Crystalline Aromatic Structural Motifs: Identification, Classification, and Implications. *Accounts of Chemical Research* **2019**, *52*, 3075–3086.

(8) Kepler, R. G. Charge Carrier Production and Mobility in Anthracene Crystals. *Physical Review* **1960**, *119*, 1226–1229.

(9) Leblanc, O. H. Hole and Electron Drift Mobilities in Anthracene. *The Journal of Chemical Physics* **1960**, *33*, 626.

(10) Shuttle, C. G.; Hamilton, R.; Nelson, J.; O'Regan, B. C.; Durrant, J. R.; Tiwari, S.; Greenham, N. C. Measurement of Charge-Density Dependence of Carrier Mobility in an Organic Semiconductor Blend. *Advanced Functional Materials* **2009**, *20*, 69–89.

(11) Podzorov, V.; Menard, E.; Rogers, J. A.; Gershenson, M. E. Hall Effect in the Accumulation Layers on the Surface of Organic Semiconductors. *Physical Review Letters* **2005**, *95*, 1–4.

(12) An, Z.; Yu, J.; Jones, S. C.; Barlow, S.; Yoo, S.; Domercq, B.; Prins, P.; Siebbeles, L. D. A.;

Kippelen, B.; Marder, S. R. High Electron Mobility in Room-Temperature Discotic Liquid-Crystalline Perylene Diimides. *Advanced Materials* **2005**, *17*, 2580–2583.

(13) Mozer, A. J.; Dennler, G.; Sariciftci, N. S.; Westerling, M.; Pivrikas, A.; Österbacka, R.; Juška, G. Time-Dependent Mobility and Recombination of the Photoinduced Charge Carriers in Conjugated Polymer/Fullerene Bulk Heterojunction Solar Cells. *Physical Review B* **2005**, *72*, 035217.

(14) Juška, G.; Genevičius, K.; Nekrašas, N.; Sliaužys, G.; Dennler, G. Trimolecular Recombination in Polythiophene: Fullerene Bulk Heterojunction Solar Cells. *Applied Physics Letters* **2008**, *93*, 2006–2009.

(15) Schouten, P. G.; Warman, J. M.; De Haas, M. P. Effect of Accumulated Radiation Dose on Pulse Radiolysis Conductivity Transients in a Mesomorphic Octa-n-Alkoxy-Substituted Phthalocyanine. *Journal of Physical Chemistry* **1993**, *97*, 9863–9870.

(16) Tiwari, S.; Greenham, N. C. Charge Mobility Measurement Techniques in Organic Semiconductors. *Optical and Quantum Electronics* **2009**, *41*, 69–89.

(17) Ostroverkhova, O. Organic Optoelectronic Materials: Mechanisms and Applications. *Chemical Reviews* **2016**, *116*, 13279–13412.

(18) Oberhofer, H.; Reuter, K.; Blumberger, J. Charge Transport in Molecular Materials: An Assessment of Computational Methods. *Chemical Reviews* **2017**, *117*, 10319–10357.

(19) Shuai, Z.; Geng, H.; Xu, W.; Liao, Y.; André, J.-M. From Charge Transport Parameters to Charge Mobility in Organic Semiconductors through Multiscale Simulation. *Chemical Society Reviews* **2014**, *43*, 2662.

(20) Lee, N.-E.; Zhou, J.-J.; Agapito, L. A.; Bernardi, M. Charge Transport in Organic Molecular Semiconductors from First Principles: The Bandlike Hole Mobility in a Naphthalene Crystal. *Physical Review B* **2018**, *97*, 115203.

(21) Boden, N.; Bushby, R. J.; Clements, J.; Movaghar, B.; Donovan, K. J.; Kreouzis, T. Mechanism of Charge Transport in Discotic Liquid Crystals. *Physical Review B* **1995**, *52*, 13274–13280.

(22) Wen, S.-H.; Li, A.; Song, J.; Deng, W.-Q.; Han, K.-L.; Goddard, W. A. First-Principles Investigation of Anistropic Hole Mobilities in Organic Semiconductors. *The Journal of Physical Chemistry B* **2009**, *113*, 8813–8819.

(23) Troisi, A.; Orlandi, G. The Hole Transfer in DNA: Calculation of Electron Coupling between Close Bases. *Chemical Physics Letters* **2001**, *344*, 509–518.

(24) Coropceanu, V.; Cornil, J.; da Silva Filho, D. A.; Olivier, Y.; Silbey, R.; Brédas, J.-L. Charge Transport in Organic Semiconductors. *Chemical Reviews* **2007**, *107*, 926–952.

(25) Brédas, J. L.; Beljonne, D.; Coropceanu, V.; Cornil, J. Charge-Transfer and Energy-Transfer Processes in π-Conjugated Oligomers and Polymers: A Molecular Picture. *Chemical Reviews* **2004**, *104*, 4971–5003.

(26) Li, L.; Tang, Q.; Li, H.; Yang, X.; Hu, W.; Song, Y.; Shuai, Z.; Xu, W.; Liu, Y.; Zhu, D. An Ultra Closely π-Stacked Organic Semiconductor for High Performance Field-Effect Transistors. *Advanced Materials* **2007**, *19*, 2613–2617.

(27) Cornil, J.; Beljonne, D.; Calbert, J.-P.; Brédas, J.-L. Interchain Interactions in Organic π-Conjugated Materials: Impact on Electronic Structure, Optical Response, and Charge Transport. *Advanced Materials* **2001**, *13*, 1053–1067.

(28) Nan, G.; Wang, L.; Yang, X.; Shuai, Z.; Zhao, Y. Charge Transfer Rates in Organic Semiconductors beyond First-Order Perturbation: From Weak to Strong Coupling Regimes. *The Journal of Chemical Physics* **2009**, *130*, 024704.

(29) Dong, H.; Fu, X.; Liu, J.; Wang, Z.; Hu, W. 25th Anniversary Article: Key Points for High-Mobility Organic Field-Effect Transistors. *Advanced Materials* **2013**, *25*, 6158–6183.

(30) Desiraju, G. R.; Gavezzotti, A. Crystal Structures of Polynuclear Aromatic Hydrocarbons. Classification, Rationalization and Prediction from Molecular Structure. *Acta Crystallographica Section B Structural Science* **1989**, *45*, 473–482.

(31) Ramakrishnan, R.; Niyas, M. A.; Lijina, M. P.; Hariharan, M. Distinct Crystalline Aromatic Structural Motifs: Identification, Classification, and Implications. *Accounts of Chemical Research* **2019**, *52*, 3075–3086.

(32) Chung, H.; Diao, Y. Polymorphism as an Emerging Design Strategy for High Performance Organic Electronics. *Journal of Materials Chemistry C* **2016**, *4*, 3915–3933.

(33) Bhat, V.; Gopan, G.; Nair, N. G.; Hariharan, M. γ-Herringbone Polymorph of 6,13-Bis(Trimethylsilylethynyl)Pentacene: A Potential Material for Enhanced Hole Mobility. *Chemistry - A European Journal* **2018**, *24*, 8679–8685.

(34) Fan, J.-X.; Chen, X.-K.; Zhang, S.-F.; Ren, A.-M. Theoretical Study on Charge Transport Properties of Intra- and Extra-Ring Substituted Pentacene Derivatives. *The Journal of Physical Chemistry A* **2016**, *120*, 2390–2400.

(35) Diao, Y.; Lenn, K. M.; Lee, W.-Y.; Blood-Forsythe, M. A.; Xu, J.; Mao, Y.; Kim, Y.; Reinspach, J. A.; Park, S.; Aspuru-Guzik, A.; Xue, G.; Clancy, P.; Bao, Z.; Mannsfeld, S.

C. B. Understanding Polymorphism in Organic Semiconductor Thin Films through Nanoconfinement. *Journal of the American Chemical Society* **2014**, *136*, 17046–17057.

(36) Dar, A. A.; Rashid, S. Organic Co-Crystal Semiconductors: A Crystal Engineering Perspective. *CrystEngComm* **2021**, *23*, 8007–8026.

(37) Coleman, L. B.; Cohen, M. J.; Sandman, D. J.; Yamagishi, F. G.; Garito, A. F.; Heeger, A. J. Superconducting Fluctuations and the Peierls Instability in an Organic Solid. *Solid State Communications* **1993**, *88*, 989–995.

(38) Yu, P.; Li, Y.; Zhao, H.; Zhu, L.; Wang, Y.; Xu, W.; Zhen, Y.; Wang, X.; Dong, H.; Zhu, D.; Hu, W. 1D Mixed-Stack Cocrystals Based on Perylene Diimide toward Ambipolar Charge Transport. *Small* **2021**, *17*, 2006574.

(39) Horiuchi, S.; Ishii, F.; Kumai, R.; Okimoto, Y.; Tachibana, H.; Nagaosa, N.; Tokura, Y. Ferroelectricity near Room Temperature in Co-Crystals of Nonpolar Organic Molecules. *Nature Materials* **2005**, *4*, 163–166.

(40) Pang, X.; Wang, H.; Wang, W.; Jin, W. J. Phosphorescent π-Hole···π Bonding Cocrystals of Pyrene with Halo-Perfluorobenzenes (F, Cl, Br, I). *Crystal Growth & Design* **2015**, *15*, 4938–4945.

(41) Madhu, M.; Ramakrishnan, R.; Vijay, V.; Hariharan, M. Free Charge Carriers in Homo-Sorted π-Stacks of Donor–Acceptor Conjugates. *Chemical Reviews* **2021**, *121*, 8234–8284.

(42) Niyas, M. A.; Ramakrishnan, R.; Vijay, V.; Hariharan, M. Structure-Packing-Property Correlation of Self-Sorted Versus Interdigitated Assembly in TTF·TCNQ-Based Charge-Transport Materials. *Chemistry - A European Journal* **2018**, *24*, 12318–12329.

(43) Guo, J.; Zeng, Y.; Zhen, Y.; Geng, H.; Wang, Z.; Yi, Y.; Dong, H.; Hu, W. Non-Equal Ratio Cocrystal Engineering to Improve Charge Transport Characteristics of Organic Semiconductors: A Case Study on Indolo[2,3-a]Carbazole. *Angewandte Chemie International Edition* **2022**, *61*, e202202336.

(44) Sharber, S. A.; Mullin, W. J.; Thomas, S. W. Bridging the Void: Halogen Bonding and Aromatic Interactions to Program Luminescence and Electronic Properties of π-Conjugated Materials in the Solid State. *Chemistry of Materials* **2021**, *33*, 6640–6661.

(45) Vijay, V.; Ramakrishnan, R.; Hariharan, M. Halogen-Halogen Bonded Donor-Acceptor Stacks Foster Orthogonal Electron and Hole Transport. *Crystal Growth & Design* **2021**, *21*, 200–206.

(46) Guo, X.; Gorodetsky, A. A.; Hone, J.; Barton, J. K.; Nuckolls, C. Conductivity of a Single

DNA Duplex Bridging a Carbon Nanotube Gap. *Nature Nanotechnology* **2008**, *3*, 163–167.

(47) Irimia-Vladu, M.; Głowacki, E. D.; Troshin, P. A.; Schwabegger, G.; Leonat, L.; Susarova, D. K.; Krystal, O.; Ullah, M.; Kanbur, Y.; Bodea, M. A.; Razumov, V. F.; Sitter, H.; Bauer, S.; Sariciftci, N. S. Indigo - A Natural Pigment for High Performance Ambipolar Organic Field Effect Transistors and Circuits. *Advanced Materials* **2012**, *24*, 375–380.

(48) Panda, S. S.; Katz, H. E.; Tovar, J. D. Solid-State Electrical Applications of Protein and Peptide Based Nanomaterials. *Chemical Society Reviews* **2018**, *47*, 3640–3658.

(49) Zhang, F.; Lemaur, V.; Choi, W.; Kafle, P.; Seki, S.; Cornil, J.; Beljonne, D.; Diao, Y. Repurposing DNA-Binding Agents as H-Bonded Organic Semiconductors. *Nature Communications* **2019**, *10*, 1–11.

(50) Benny, A.; Sasikumar, D.; Hariharan, M. In Silico Exploration for Maximal Charge Transport in Organized Tetrabenzoacenes through Pitch and Roll Displacements. *Journal of Physical Chemistry C* **2019**, *123*, 26758–26768.

(51) Ambili, R. V.; Sasikumar, D.; Hridya, P.; Hariharan, M. Deciphering the Multifarious Charge-Transport Behaviour of Crystalline Propeller-Shaped Triphenylamine Analogues. *Chemistry - A European Journal* **2019**, *25*, 1992–2002.

(52) Sebastian, E.; Philip, A. M.; Benny, A.; Hariharan, M. Null Exciton Splitting in Chromophoric Greek Cross (+) Aggregate. *Angewandte Chemie International Edition* **2018**, *57*, 15696–15701.

(53) Lijina, M. P.; Benny, A.; Ramakrishnan, R.; Nair, N. G.; Hariharan, M. Exciton Isolation in Cross-Pentacene Architecture. *Journal of the American Chemical Society* **2020**, *142*, 17393—17402.

(54) Okamoto, T.; Yu, C. P.; Mitsui, C.; Yamagishi, M.; Ishii, H.; Takeya, J. Bent-Shaped p - Type Small-Molecule Organic Semiconductors: A Molecular Design Strategy for Next-Generation Practical Applications. *Journal of the American Chemical Society* **2020**, *142*, 9083–9096.

(55) Mitsui, C.; Okamoto, T.; Yamagishi, M.; Tsurumi, J.; Yoshimoto, K.; Nakahara, K.; Soeda, J.; Hirose, Y.; Sato, H.; Yamano, A.; Uemura, T.; Takeya, J.; Okamoto, T.; Takeya, J.; Mitsui, C.; Yamagishi, M.; Yoshimoto, K.; Hirose, Y.; Uemura, T.; Tsurumi, J.; Nakahara, K.; Soeda, J.; Sato, H.; Yamano, A. High-Performance Solution-Processable N-Shaped Organic Semiconducting Materials with Stabilized Crystal Phase. *Advanced Materials* **2014**, *26*, 4546–4551.

Chapter 2

Atom-Efficient Halogen−Halogen Interactions Assist One-, Two-, and Three-Dimensional Molecular Zippers

Abstract: Unprecedented multimodal weak interactions are quintessential to create novel supramolecular topologies. Among the plethora of weak interactions, halogen−halogen (X•••X) interactions offer innovative possibilities for the design of multidimensional scaffolds. Herein, we chronicle the state-of-the-art 1D, 2D, and 3D zipper motifs steered by distinct interhalogen interactions, revealing the potential of halogen bonding in engineering biomimetic molecular assemblies. Recurring units of Br_4 synthon, framed by type I and type II atom efficient X•••X interactions in a dibromonaphthothiazole derivative, 2,4-dibromo-5- ethoxynaphtho[1,2-*d*]thiazole (NTB_2), forges the molecular zipper. On the basis of the semiclassical Marcus theory of charge transport, the NTB_2 zipper assembly displays selective electron transport along the type II X•••X bonded direction. Band structure analysis classified the crystalline NTB_2 as a wide band gap semiconductor with a band gap of 2.80 eV. The robustness of the X•••X mediated zipper motif opens up new avenues in the development of advanced functional materials.

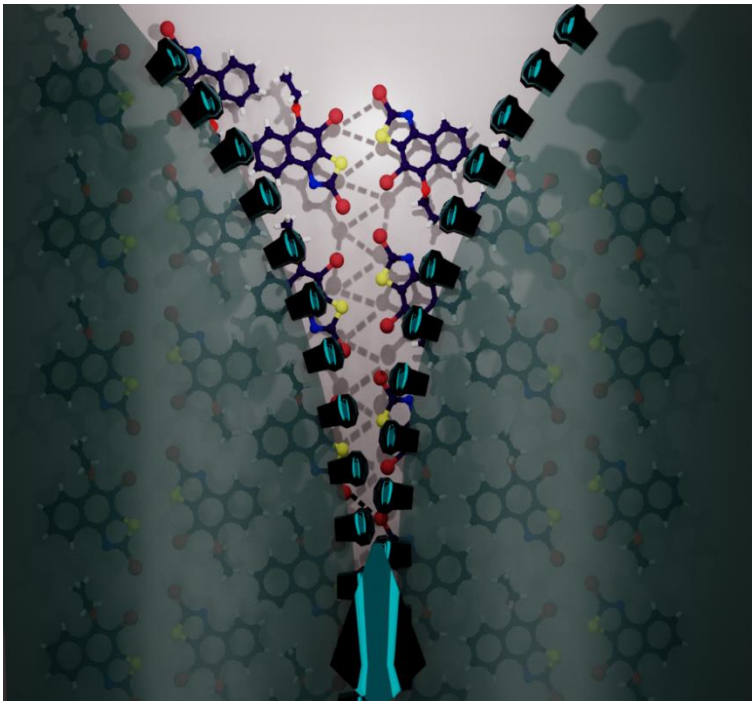

2.1. Introduction

Self-assembly of interacting units which compose complex multistranded architecture is a common structural motif in biology, for instance, leucine zipper[1] and β-pleated sheets.[2] The most intriguing structural design that resembles natural DNA is a molecular zipper, which is of paramount importance in molecular biology,[3,4] fiber behavior,[5] and guest sorption.[6] Hence, the quest for functional supramolecular structures to construct discrete molecular zippers is of huge significance. Hydrogen bonding,[7] electrostatic interactions, π−π interactions,[8] and van der Waals forces[9] play a central role in engendering synthetic biomolecular zippers. We exploited the excellent directionality and tunability offered by X•••X interactions by integrating bromine atoms in angular naphthothiazole moiety, which induces atom efficient interactions tethering an infinite zipper assembly (NTB_2). Thiazole-based small organic molecules and conjugated polymers exhibiting high hole or electron mobilities were used as p- or n-type semiconductors.[10] The in-depth inspection of important structure-property relationships[11] is vital for the design of functional, high-performance organic semiconductors.[12] Incorporation of halogen atoms to the aromatic core has been shown to decrease the band gap of conjugated compounds.[13] The possibility of enhancing semiconducting property by the halogen incorporation in thiazole-based systems was taken into account while structuring NTB_2.

A fundamental understanding of noncovalent interactions (NCI) is the cornerstone of crystal engineering, a paradigm of supramolecular chemistry. The cooperative and synergistic nature of NCI can be exercised to form highly ordered and complex array of supramolecular synthons with alluring properties. Halogen bonding, a σ-hole[14] interaction analogous to hydrogen bonding is a prime member in the repertoire of NCI, encompassing a wide range of applications including supramolecular gels,[15] material science,[16] anion recognition,[17] and biomimetic systems.[18,19] Although iodine forms the strongest halogen bond, bromine has been incorporated in biological and semiconducting systems owing to its compatible size and better stability.[20] The classical electrostatic model[21] of σ-hole interaction was established to explain the stability of halogen bonds. However, quantum covalency,[22,23] hyperconjugation,[24] dispersion, and induction forces[25] have been acknowledged as crucial for the stability of halogen bonds. Conventionally, R−X•••X−R (X = halogen atom) contacts are classified as types I and II, based on the geometric and chemical distinction (Scheme 2.1).[26] Contrary to the conviction of the destabilizing nature, type I interactions proved to be stabilizing in supramolecular synthons owing to the exchange-correlation

component.[18] Atom-efficient self-complementary interactions in small molecules are indispensable to augment ordered multistranded molecular arrays.[27] In crystalline NTB_2, the halogen bond boosted self-complementary molecular pair interlocks like teeth in true zipper.

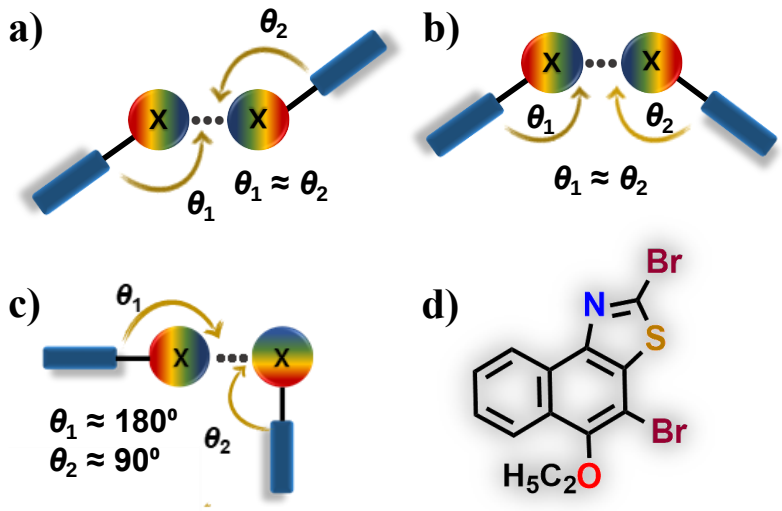

Scheme 2.1: Schematic representation of (a) Type I trans (b) Type I cis, and (c) Type II dihalogen interactions. (d) Chemical structure of NTB_2.

2.2. Results and Discussion

The Sandmeyer reaction was employed to synthesize 2,4-dibromo-5-ethoxynaphtho[1,2-*d*]thiazole (NTB_2) (Scheme 2.2).[28] Needle-shaped colorless single crystals of NTB_2 with the space group $P\bar{1}$ were obtained by slow evaporation from acetonitrile (Table 2.1). The crystal structure of

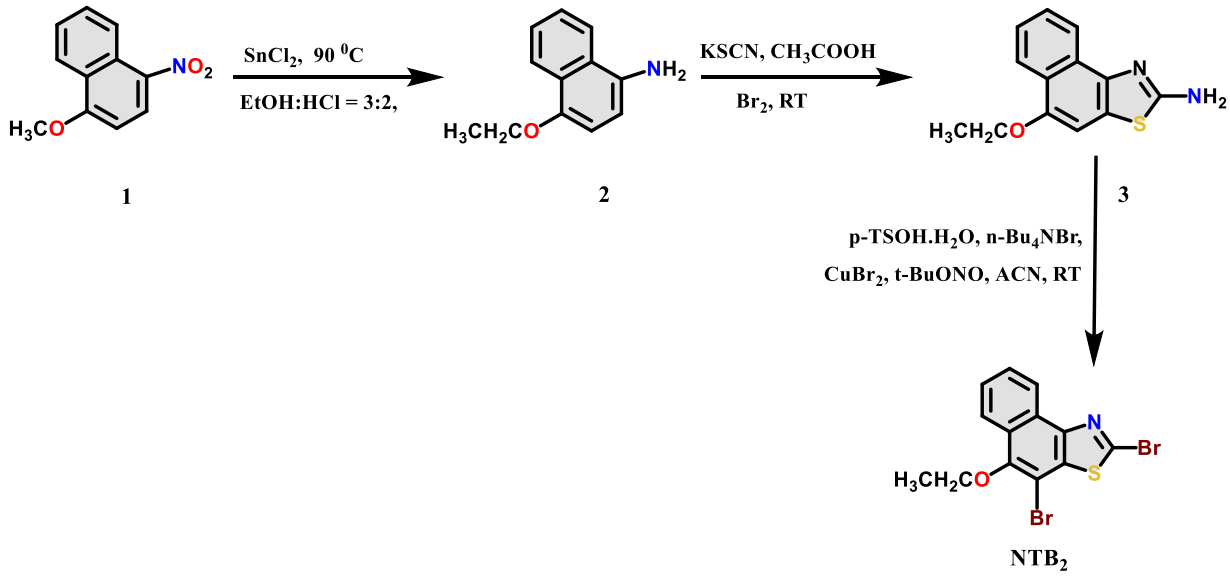

Scheme 2.2: Reaction scheme for the synthesis of NTB_2.

Table 2.1: Crystallographic data and refinement process for NTB_2.

Parameters	NTB_2
Formula	$C_{13}H_9Br_2NOS$
Formula weight	387.09
Colour	Colorless
Crystal system	Triclinic
Space group, Z	$P\bar{1}$, 2
a (Å)	4.032
b (Å)	9.774
c (Å)	16.841
α, deg	104.639
β, deg	91.864
γ, deg	95.118
Volume, $Å^3$	638.6
R factor	5.15
Temp, K	296
$d_{calculated}$ (mg/m^3)	2.013
No. of reflections collected	16425
No. of unique reflections	2253
$2\theta_{max}$, deg	24.986
No. of parameters	163
R1, wR2, (l > 2s(l))	0.0515, 0.1125
R1, wR2 (all data)	0.1265, 0.1477
Goodness of fit	1.016
CCDC number	2061950

NTB_2 comprises a planar naphthothiazole moiety and an ethoxy group in an out-of-plane orientation. Single-crystal X-ray diffraction analysis revealed intermolecular van der Waals (vdW)[29] Br•••Br interactions with interatomic distances of 3.65, 3.84, and 4.03 Å (Figure 2.1a, b, d). Though Bondi's[30] classification is widely employed in predicting noncovalent interactions, the existence of Br•••Br interactions beyond the sum of van der Waals radii have been established recently.[31–33] Comprehensive analysis of the crystal structure substantiate the key roles played by Br•••Br, Br•••S, and π−π interactions in forming the 3D close packing of NTB_2 (Figure 2.1). The crystal lattice of NTB_2 comprises of three different noncovalently interacting dimers (T1, T2, and stacked dimer (T3)), classified based on distinct interhalogen interactions. The (sp^2)C−Br•••Br−C(sp^2) angles in T1 ($\theta_1 = \theta_2 = 151.12°$), T_2 ($\theta_1 = 94.03°$, $\theta_2 = 167.15°$), and T3 ($\theta_1 = 79.19°$ and $\theta_2 = 100.81°$) confirm the existence of types I and II and a near-orthogonal Br•••Br interaction (Figure 2.2). Cooperative intermolecular Br•••Br interactions between four units of NTB_2 furnished a Br_4 synthon which extends infinitely through type I (cis and trans) X•••X interactions. Synergistic Br•••Br (type II) and Br•••S interactions drive the design of self-complementary 1D zipper (T2) of NTB_2. Self-complementary T2 replicas fabricate an extended infinite chain of halogen bonded zipper assembly along the crystallographic b-axis (Figure 2.1c).

To explore the nature and strength of X•••X interaction fostering extended self-complementary zipper assembly in NTB_2, Hirshfeld surface (HS),[34] noncovalent interaction (NCI),[35] Bader's quantum theory of atoms in molecules (QTAIM),[36] and truncated symmetry-adapted perturbation theory (SAPT(0))[37] investigations were performed. Mapping the HS allowed

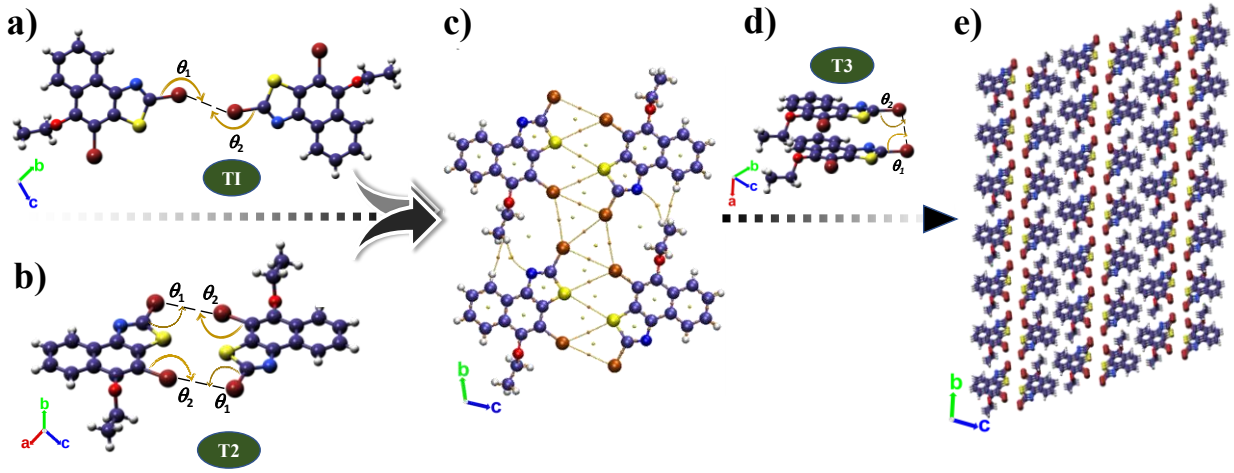

Figure 2.1: (a) T1 dimer. (b) T2 dimer. (c) 2D zipper formed from T1 and T2 dimers (BCP and RCP obtained from QTAIM analysis). (d) T3 dimer. (e) 3D zipper of NTB_2 formed from the extension of 2D zipper assisted by T3 dimer along the a-axis.

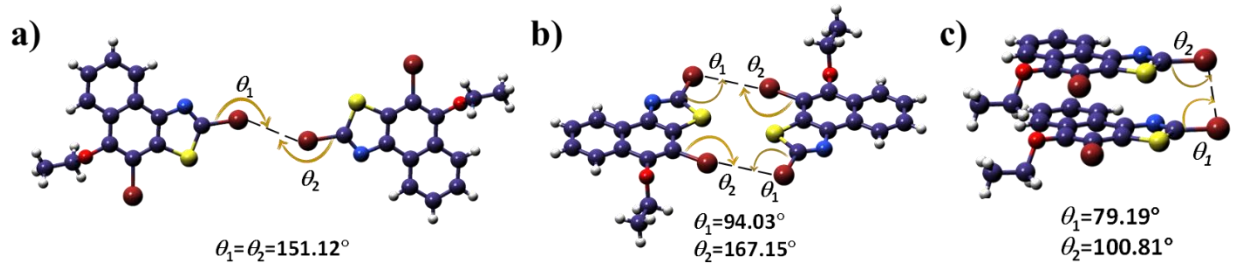

Figure 2.2: Angles between Br•••Br interaction in a) T1 dimer, b) T2 Dimer, C) T3 Dimer of NTB_2.

quantification of weak intermolecular interactions in NTB2 (Table 2.2). The ratio of the percents of C•••H and C•••C interactions defined a β-motif (ρ = 0.65) arrangement in NTB_2.[11] Noncovalent bond formation in NTB_2 was qualitatively assessed by QTAIM analysis (Figure 2.1c). Electron density (ρ(r)) and its Laplacian [$\nabla^2\rho(r)$] at the (3, −1) bond critical points (BCP) advocated the closed-shell nature of Br•••Br intermolecular interactions in crystalline NTB_2 (Table 2.3). Surprisingly, an atom efficient six atom quintuple interaction was observed and confirmed by (3, −1) BCP within the interacting atoms in T2. Self-complementary T2 held by Br•••S and type II

Table 2.2: Relative % of intermolecular interactions obtained from Hirshfeld analysis.

Interaction	C•••H	C•••C	Br•••Br	Br•••S	ρ=[(%C•••H)/(%C•••C)]
NTB_2	9.9	6.5	14.6	4.7	0.65

Table 2.3: Calculated topological properties of electron density function for the intermolecular interactions in crystalline NTB_2.

		Interactions	d, Å	ρ(r), eÅ^{-3}	∇^2ρ(r), eÅ^{-5}
NTB_2 Tetramer showing Br_4 synthon	Bond critical points (BCPs)	Br107•••Br27	3.844	0.005043	0.015602
		Br107•••Br81	3.851	0.005098	0.016174
		Br27•••Br81	3.654	0.006161	0.020621
		Br81•••Br53	3.844	0.005042	0.015600
		Br53•••Br27	3.851	0.005097	0.016173
	Ring critical points (RCPs)	Br27–Br53–Br81	–	0.002336	0.008072
		Br27–Br81–Br107	–	0.002336	0.008073

NTB_2 Tetramer showing zipper with 12 atom 13 interaction	Bond critical points (BCPs)	Br107•••Br27	3.844	0.005043	0.015602
		Br107•••Br81	3.851	0.005098	0.016174
		Br27•••Br81	3.654	0.006161	0.020621
		Br81•••Br53	3.844	0.005042	0.015600
		Br53•••Br27	3.851	0.005097	0.016173
		Br53•••S25	3.779	0.005460	0.016926
		Br54•••Br26	3.844	0.005029	0.016096
		Br80•••S106	3.844	0.005443	0.016914
		Br80•••B108	3.762	0.005030	0.016096
		S79•••S106	3.779	0.004671	0.015793
		S79•••Br107	3.762	0.005459	0.016925
		S52•••S25	3.779	0.004671	0.015792
		S52•••Br26		0.005443	0.016916
	Ring critical points (RCPs)	C22–S25–Br53–Br27	–	0.003366	0.011549
		C76–S79–Br107–Br81	–	0.003661	0.011549
		Br26–S52–C49–Br54	–	0.003542	0.011500
		Br80–S106–C103–Br108	–	0.003353	0.011499
		H44–Br53–Br81	–	0.001934	0.006527
		Br27–H98–Br107	–	0.001934	0.006528
		C42–H44–Br81–C76–N77–H47–C45	–	0.001256	0.005302
		Br27–Br53–Br81	–	0.002336	0.008072
		Br27–Br81–Br107	–	0.002336	0.008073
			–	0.003274	0.010593

		C12–C13–Br26–S52–S25 S25–S52–C39–C40–Br53 C66–C67–Br80–S106–S79 S79–S106–C93–C94–Br107 C67–C68–O78–C69–H71–Br80 H47–H63–C62–C64–C65–N77 C8–H9–H101–N23–C11–C10 C94–C95–O105–C96–H98–Br107 C22–N23–H101–C99–C96–H98–Br27 C92–C93–S106–C103–N104	– – – – – – – –	0.003283 0.003274 0.003283 0.008059 0.003209 0.003210 0.008028 0.001256 0.046174	0.010609 0.010593 0.010609 0.032140 0.012233 0.012234 0.032022 0.005302 0.025712
T3 Dimer	Bond critical points (BCPs)	Br27•••Br54	4.033	0.004397	0.019263

Br•••Br interaction extends via type I Br•••Br interaction giving rise to a set of noncovalent triangles (Figure 2.1c). Four bromine atoms of tetrameric NTB_2 unit form a noncovalent parallelogram (Br_4 synthon) which is evident from (3, +1) ring critical point (RCP) (Figure 2.1c). QTAIM analysis establishes the significance of Br•••Br interactions in devising the extended zipper assembly. All intermolecular interactions in NTB_2 existing beyond the sum of van der Waals radii were confirmed by presence of (3, −1) BCP (Figure 2.3, Table 2.3). Pendas' interacting quantum

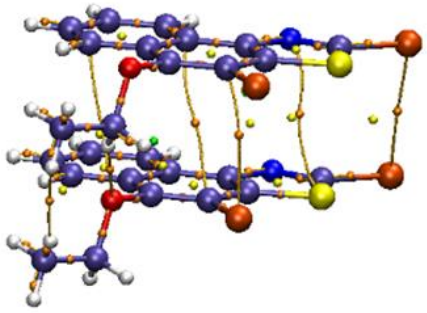

Figure 2.3: QTAIM electron density map showing Br•••Br interaction in T3 dimer of NTB_2.

atoms (IQA) approach was used to investigate the nature of Br•••Br and Br•••S interactions in driving the formation of extended zipper assembly. IQA partitions the total interatomic energy (E_t) into classical Coulombic component (E_{cl}) and an exchange-correlation component (E_{xc}). The total IQA interaction energies for Br•••Br and Br•••S interactions in T2, Br···Br interactions in Br_4 synthon, and near-orthogonal Br•••Br interaction in T3 were found to be stabilizing (Table 2.4). In all the examined cases, a major stabilizing component of interaction energy arises from the exchange-correlation term.

The nature of intermolecular noncovalent interactions in NTB_2 zipper was visualized using the NCI plot.[38] The attractive and repulsive interactions were distinguished by the sign of the second density Hessian eigenvalue (λ_2). The green isosurface represents weak attractive noncovalent interactions corresponding to Br•••Br and Br•••S intermolecular contacts (Figure 2.4). The zipping nature of the Br_4 synthon extending as linear infinite chain was attributed to noncovalent interactions confirmed from NCI and QTAIM analyses. The role of the electrostatic component in regulating the zipper assembly was established by computing the electrostatic surface potential (ESP) map of NTB_2 (Figure 2.5). From ESP, a region of positive potential (σ-hole), depicted as a cap of depleted electron density along the C•••Br covalent bond axis, and an orthogonal negative potential belt on the surface of halogen atoms are evident. Overlap between

Table 2.4: IQA interaction energies. Total noncovalent interaction energies and its components are shown. Energies are given in kcal/mol.

	Interactions	E_t	E_{xc}	E_{cl}
T2 Dimer	Br26-Br54	-5.45	-5.11	-0.33
	Br26-S52	-6.02	-4.74	-1.28
	S52-S25	0.53	-3.66	4.20
	Br53-S25	-6.00	-4.74	-1.25
	Br53-Br27	-5.30	-5.11	-0.19
Tetrahalo synthon	Br53-Br27	-4.92	-4.75	-0.18
	Br81-Br53	-4.48	-4.67	0.18
	Br107-Br27	-4.46	-4.65	0.19
	Br81-Br27	-6.19	-6.14	0.04
	Br107-Br81	-4.92	-4.75	-0.17
T3 Dimer	Br27-Br54	-3.72	-4.06	0.34

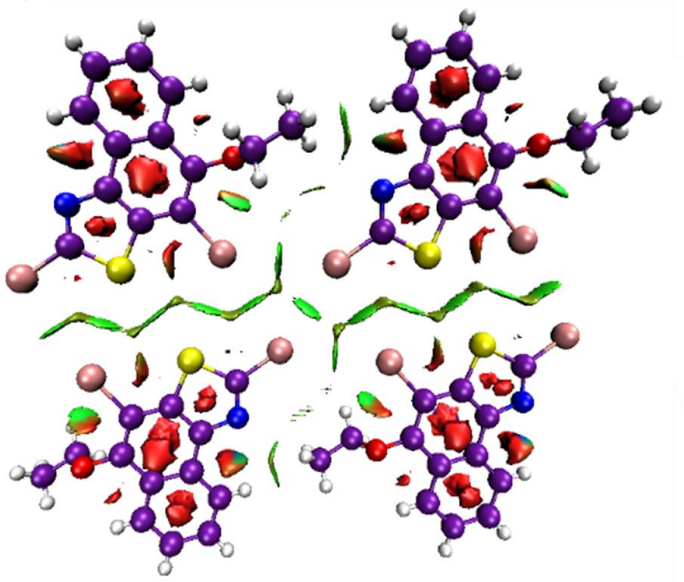

Figure 2.4: NCI plot showing weak stabilizing interactions in NTB_2 zipper represented as green discs.

the electrophilic and nucleophilic regions of interacting halogen atoms plays a pivotal role in assembling T2 in a self-complementary manner which results in unbounded 2D zipper assembly.

SAPT(0) analysis was employed to explore the stability of the intermolecular interactions[39] modeling molecular zippers of NTB_2. SAPT(0) provided a quantitative picture of the interactions by decomposing the total interaction energy into physically meaningful components (electrostatic, exchange, induction, and dispersion) (Table 2.5). The negative SAPT(0) (ESAPT(0)) values of −0.65, −3.30, and −26.85 kcal/mol show the stabilizing nature of T1, T2, and T3 dimers respectively, in amalgamating the 3D zipper assembly of NTB_2. The nature of X•••X interaction

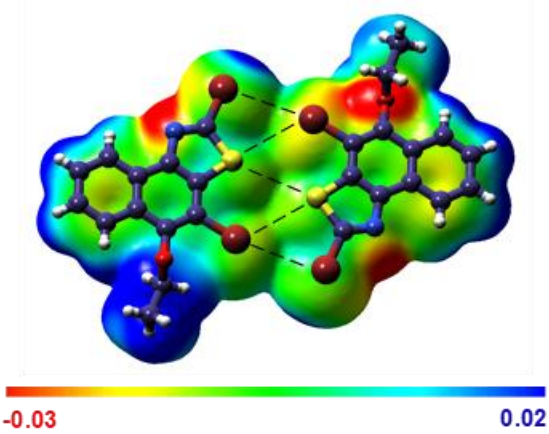

Figure 2.5: ESP Electrostatic potential in atomic units on the 0.001 isodensity surfaces of NTB_2 dimer. ESP values range from -0.03 a.u. (red) to +0.02 a.u. (blue).

from a molecular orbital perspective was probed using natural bond orbital (NBO) analysis.[40] The major orbital contribution with maximum magnitude of interaction energy comes from the interaction between lone pairs of Br and S atoms with the antibonding (BD*) C−X (X = Br and S) orbitals (Table 2.6). Significant stabilization energy observed for Br•••Br and Br•••S interactions establishes the combined effect of halogen interactions in guiding the 3D close packing. Intermolecular attractive interactions in molecular crystals are closely related to the permanent dipole moment of the monomer.[41] The multiple heteroatoms present in NTB_2 offer a net dipole moment of 2.72 D (Table 2.7). Molecules possessing high dipole moments (dipole moment >4.0 D) have a tendency to align in an antiparallel orientation which minimizes the net dipole moment.[42,43] T1 and T2 dimers have an antiparallel orientation which results in zero dipole moment forming a 2D self-complementary zipper assembly. Here the crystal packing of NTB_2 satisfies the minimum dipole moment requirement. Scanning electron microscopy (SEM) provided the possibility to unfold the details of the morphology. SEM images verified the presence of long fibers owing to the halogen bonded zippers (Figure 2.6).

The optical band gap of NTB_2 was determined from the experimental UV−vis−NIR absorption spectrum employing the Tauc method. The linear part of the $(\alpha h\nu)^2$ versus hν plot was extrapolated to the x-axis and a direct band gap of E_g = 3.45 eV was derived from the point of intersection with the horizontal x-axis (Figure 2.7). To theoretically determine the band gap and predict the semiconducting properties, first-principle calculations were performed within the

Table 2.5: Interaction Energies of Representative NTB_2 Dimers from SAPT(0) jun-cc-pvdz Calculations[a]

Dimer	E_{int}^{SAPT}	$E_{ele}^{(1)}$	$E_{dis}^{(2)}$	$E_{ind}^{(2)}$	$E_{ex}^{(1)}$
T1	-0.65	-0.77	-1.54	-0.23	1.90
T2	-3.30	-3.16	-1.54	-0.80	7.25
T3	-26.85	-11.94	-39.89	-2.56	27.55

[a]All energy values are provided in kcal/mol. E_{int}^{SAPT} = Total interaction energy; $E_{ele}^{(1)}$ = Electrostatic; $E_{dis}^{(2)}$ = Dispersion; $E_{ind}^{(2)}$ = Induction and $E_{ex}^{(1)}$ = Exchange repulsion energy. More details are given in Supporting Information.

Table 2.6: Selected donor-acceptor natural bond orbital interactions with their corresponding second-order perturbation stabilization energies in T1, T2 and T3 dimes of NTB_2. Energies are given in kcal/mol.

Dimer	Donor NBO	Acceptor NBO	E(2)
T1	LP(1) Br27	BD*(1) C49-Br54	0.33
	LP(2) Br27	BD*(1) C49-Br54	0.34
	LP(3) Br27	BD*(1) C49-Br54	0.17
T2	LP(2) Br27	BD*(1) C40-Br53	1.01
	LP(1) Br26	BD*(1) C39-S52	0.13
	LP(2) Br26	BD*(1) C39-S52	0.79
	LP(1) Br27	BD*(1) C40-Br53	0.13
	LP(1) S25	BD*(1) C49-S52	0.27
	LP(1) S25	BD*(1) C40-Br53	0.07
T3	LP(1) Br27	BD*(1) C40-Br53	0.07
	LP(1) Br27	BD*(1) C49-Br54	0.05
	LP(3) Br26	BD*(1) C40-Br53	0.06
	LP(2) Br27	BD*(1) C49-Br54	0.07
	LP(3) Br27	BD*(1) C49-Br54	0.06

framework of DFT. The calculations of total-energy and electronic structure have been performed using Plane-Wave Self-Consistent Field package, a component of the Quantum Espresso distribution. The exchange-correlation interactions are treated within the generalized gradient approximation of the Perdew−Burke− Ernzerhof type.[36] The calculated electronic band structure of NTB_2 is displayed in Figure 2.8a. The fundamental band gap is found to be a direct type with a

Table 2.7: Magnitudes of dipole moments for adjacent dimers in the crystal packing of NTB_2.

NTB_2	Dipole Moment (Debye)
Monomer	2.742
T1 Dimer	0.005
T2 Dimer	0.008
T3 Dimer	5.241
Tetramer	0.001

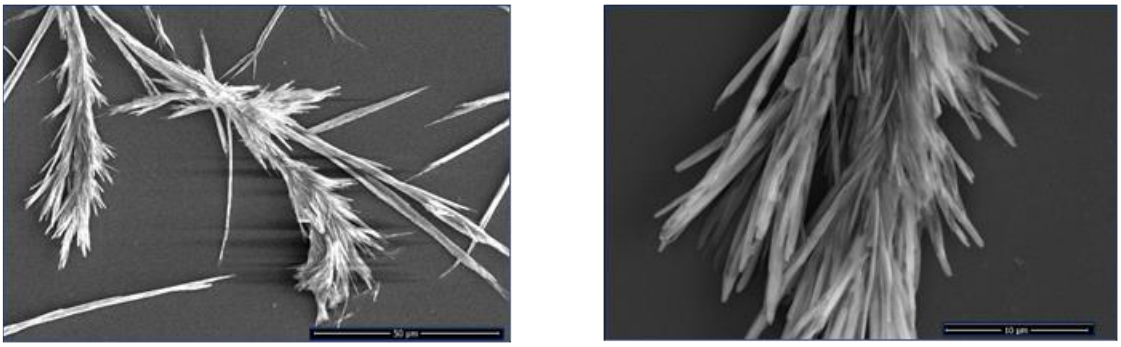

Figure 2.6: SEM images showing the surface fiber morphology of NTB_2.

value of E_g = 2.80 eV which falls under the semiconductor regime. The calculated band gap was smaller than the experimental value of 3.45 eV deduced from Tauc plot (Figure 2.7). The difference owes to the possible fact that DFT underestimates the band gap of bulk solids,[44–46] as the contribution of exchange-correlation to energy is unknown and must be approximated in DFT. The TDOS and PDOS obtained from DFT are plotted in Figure 2.8b. The greatest contributor toward the valence (VB) and conduction band (CB) is the valence p orbitals of carbon atoms as expected, followed by the contributions from the lone pairs of bromine atoms, citing the influence of halogen interactions in the semiconducting property. Bonding interactions of bromine 4p and sulfur 3p orbitals noticed in the lower energy levels (0.2−0.7 eV) of the VB (Figure 2.9a) is attributed to Br•••S interactions in NTB_2 zipper. The antibonding states of the CB are majorly composed of sulfur 3p orbitals. The overall contribution from hybridized orbitals to both the CB and VB is limited (Figure 2.9b). The bands are less dispersed at the top of the VBs and at the bottom of CB,

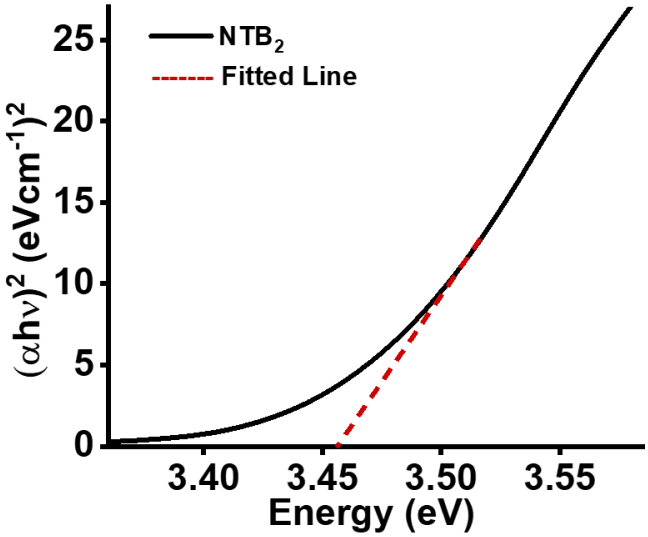

Figure 2.7: Tauc plot of NTB_2.

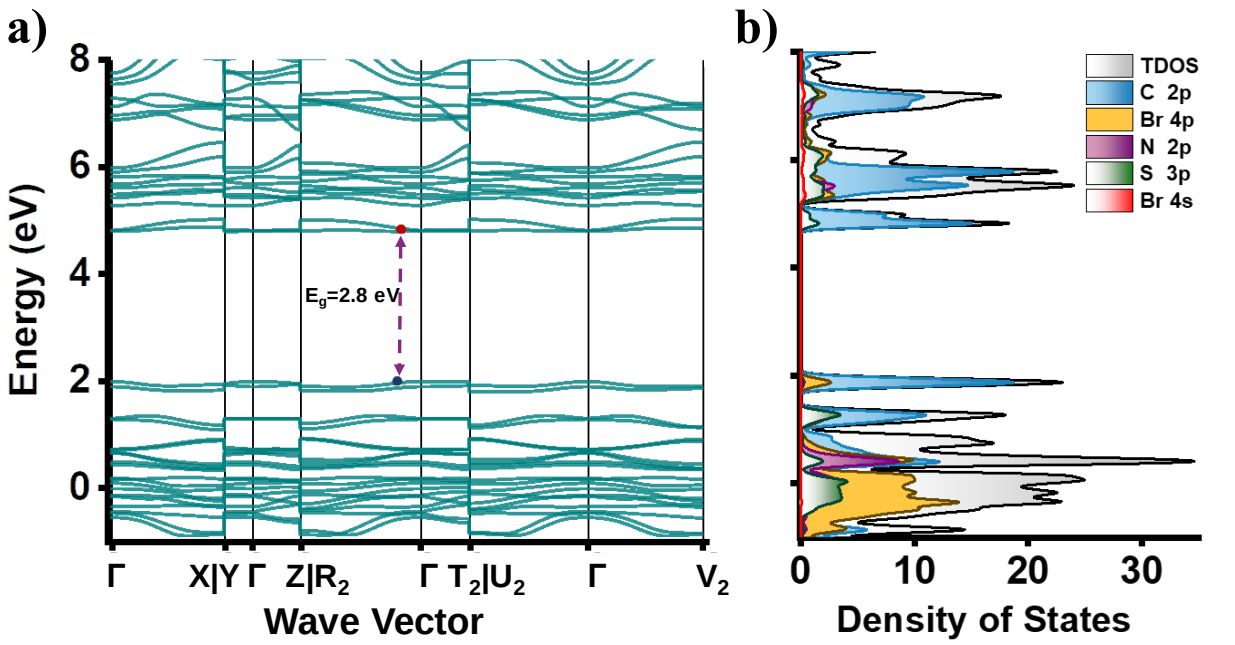

Figure 2.8: (a) Electronic band structure of NTB_2, HOMO and LUMO are plotted as blue and red filled circles respectively, the labeled points indicate Γ(0.0, 0.0, 0.0), R_2(0.8, −0.3, 0.2), T_2(0.0, −0.3, 0.1), U_2(0.8, −0.3, 0.0), V_2(−0.8, −0.1, 0.1), X(−0.9, −0.1, 0.0), and Y(0.0, 0.0, −0.2) positions in reciprocal space. (b) Total DOS spectrum of NTB_2 and valence orbital PDOS spectra of the constituent atoms from DFT calculations.

illustrating the localized nature (Figure 2.8a).[47] In order to probe the charge transport properties near the localized band edges, charge transfer coupling ($V_{e/h}$) and intramolecular reorganization

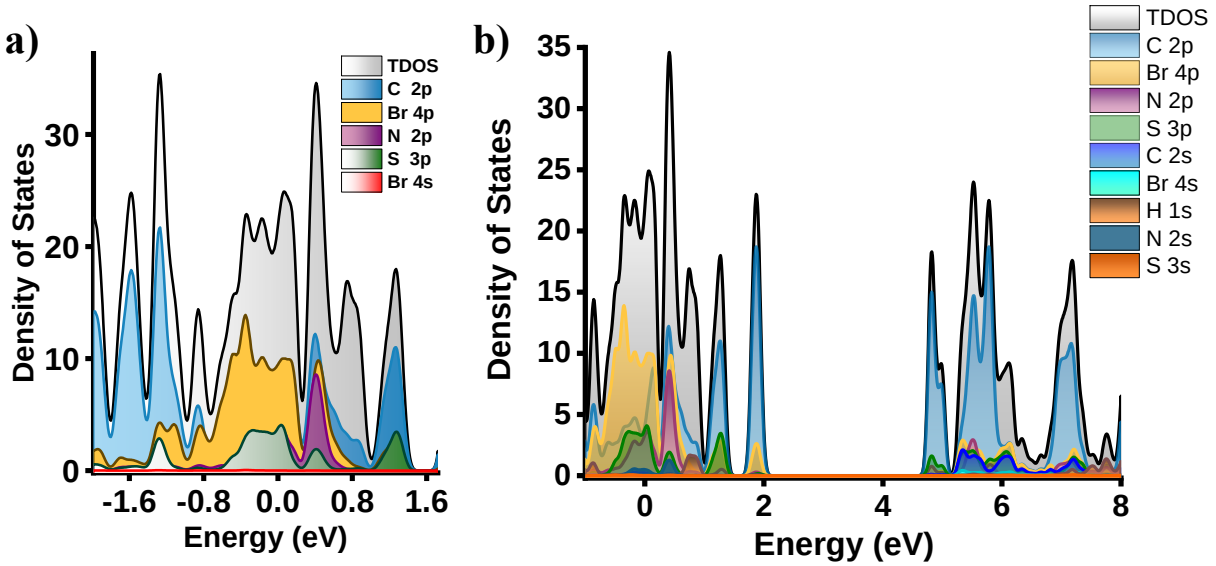

Figure 2.9: Total DOS spectrum of NTB_2 a) showing overlap of bromine 4p and sulphur 3p, b) PDOS spectra of p and s orbitals of Br, C, H, N and S atoms from DFT calculations.

Table 2.8: Electron and hole reorganization energy ($\lambda_{e/h}$) and charge transfer coupling values ($V_{e/h}$) of selected dimers of NTB_2.

Dimer		V_e (eV)	V_h (eV)
T1 Dimer	λ_e=-0.348 eV λ_h=-0.685 eV	-0.008	-0.005
T2 Dimer		-0.050	-0.006
T3 Dimer		-0.047	0.035

energies ($\lambda_{e/h}$) were calculated by employing the semiclassical Marcus theory of charge transfer.[48,49] The charge transfer couplings (V_e = 0.008−0.050 eV, V_h = 0.005− 0.035 eV) are negligible when compared to the electron and hole reorganization energies (λ_e = 0.348 eV and λ_h = 0.685 eV, $2V_{e/h} < \lambda_{e/h}$), ensuring NTB2 follows hopping transport over the localized sites near the band edges (Table 2.8).[50] The theoretical mobility calculation of crystalline NTB_2 displayed a higher electron mobility (μ_e = 0.0763 $cm^2V^{-1}s^{-1}$) compared to the hole mobility (μ_h = 0.0003 $cm^2V^{-1}s^{-1}$) on account of the high electron transfer coupling and low reorganization energy of the electron (Figure 2.10c, Table 2.8). The influence of zipper arrangement on the anisotropic variation of charge

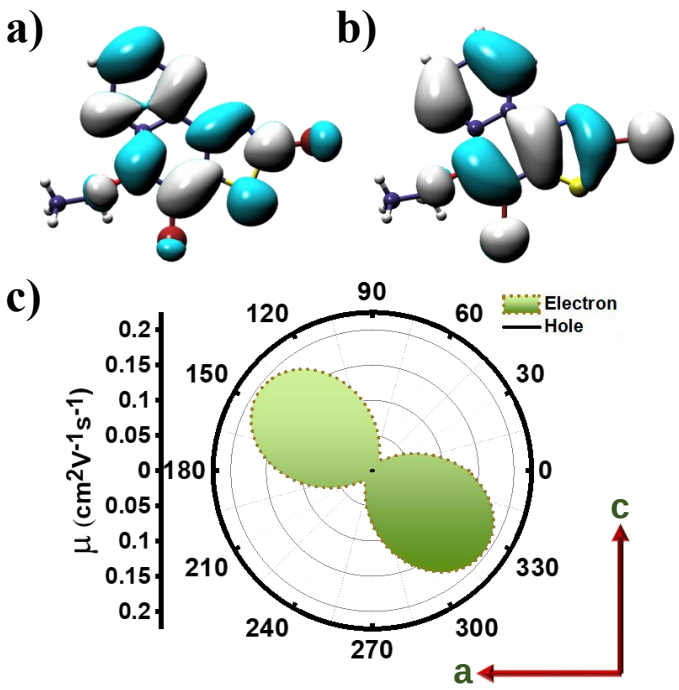

Figure 2.10: (a) LUMO and (b) HOMO (isosurface value 0.02) of NTB_2. (c) Anisotropic electron and hole mobility of NTB_2 along the stacking plane. The crystallographic a-axis is taken as the reference axis, and the ac-plane as the plane of interest.

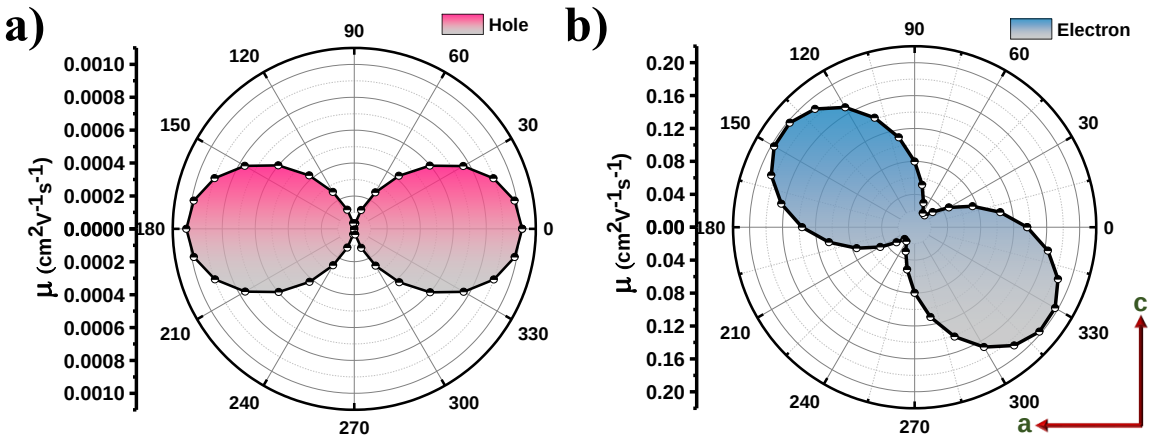

Figure 2.11: Anisotropic a) hole and b) electron moBilities of NTB_2 along the stacking plane. Crystallographic *a*-axis is taken as the reference axis and projected on *ac* plane.

transport in the crystal was analyzed**.** The a-axis, parallel to the π−π stacking direction was chosen as principal axis, and the *ac*-plane was chosen as the reference plane, upon which the anisotropic mobility of the crystal was projected. A difference in directionality of the hole and electron anisotropic mobility was observed (Figure 2.11), arising from the varied charge transfer coupling between the neighboring molecular units. The efficient orbital overlap of LUMO−LUMO wave function resulted in high electron coupling (V_e) in the T2 dimer.

2.3. Conclusion

In summary, we report the first crystalline evidence of hierarchical formation of 1D and 2D zippers crafted by precise atom-efficient, six-atom quintuple interactions, C−Br•••Br−C and C−Br•••S−C, in NTB_2. The probability of forming multiple interactions by incorporating two bromine atoms adjacent to sulfur atom in angular naphthothiazole was exploited to form a self-complementary 1D zipper mimicking DNA base pair interactions. The 1D zipper extending through type I X•••X interactions modeled a unique 12-atom, 13- interaction forming a Br_4 synthon. Multivalent interactions of bromine and sulfur atoms glued NTB_2 to form an infinite 2D halogen-bonded zipper. The 2D zipper was further extended by π−π stacking and a near-orthogonal X•••X interaction guiding the formation of the 3D zipper in NTB_2. QTAIM and NCI analyses manifested the exceptional role of noncovalent interhalogen interactions in molding the teeth of zipper. IQA elucidated the dominant contribution of the exchange-correlation component over the classical electrostatic component toward the stability of the zipper formed by virtue of Br_4 synthon. The

analysis further reinforces the role of quantum covalency in the origin of X•••X interactions. Furthermore, inspections from semiclassical Marcus theory of charge transfer projects a charge-filtering (selective electron transport) phenomenon in crystalline NTB_2. The semiconductor characteristics of the thiazole moiety can be tuned by the incorporation of halogen atoms, which is a promising design strategy for improved semiconducting performances.

2.4. Experimental Section

2.4.1. Synthesis of 4-(methoxymethyl)naphthalen-1-amine.

Stannous chloride (12.3 mmol) was dissolved in 3:2 ratio of ethanol and hydrochloric acid mixture. Added 1-methoxy-4-nitronapthalene (2.46 mmol) to the solution and was stirred for 4 hours at 90ºC. The reaction mixture was then cooled down to room temperature and extracted with dichloromethane. The crude mixture was used for the next reaction without further purification.

2.4.2. Synthesis of 4-bromo-5-(ethoxymethyl)naphtho[1,2-*d*]thiazol-2-amine.

Added 4-ethoxynapthalen-1-amine (crude, 0.23 mmol) and potassium thiocyanate (0.46 mmol) to a round bottom flask charged with glacial acetic acid and stirred for 5 minutes. Then slowly added Br_2 (0.33 mmol) dropwise using an addition funnel and the reaction was stirred for 6 hours at room temperature. After confirming the full consumption of reactant, added 10ml of saturated sodium thiosulphate solution to quench the excess bromine in the reaction mixture. The organic compound was extracted using dichloromethane and was purified using silica gel column chromatography to obtain 4-bromo-5-ethoxynaphtho[1,2-*d*]thiazol-2-amine in 34 % yield.

Mp: 232°C;

^{1}H NMR (500 MHz, $CDCl_3$, ppm): δ = 8.35(d, J = 5 Hz, 1H), 8.05 (d, J = 5 Hz, 1H), 7.49 (m, J = 30 Hz, 2H), 5.89 (s, 2H), 4.1 (m, J = 20 Hz, 2H), 1.49 (m, J = 15 Hz, 3H);

HRMS (ESI): m/z calculated for $C_{13}H_{11}BrN_2OS$: 322.9826, found: 322.9846

2.4.3. Synthesis of 2,4-dibromo-5-ethoxynaphtho[1,2-*d*]thiazole.

To a solution of 3 (1.3 mmol) in acetonitrile, *p*-toluenesulfonicacid (1.7 mmol), $CuBr_2$ (0.02 mmol), Tetra-n-butylammonium bromide (2.6 mmol) was added and stirred at room temperature for 4 hours. On completion of reaction, the reaction mixture was quenched by adding 15 ml of water, washed with Sodium bicarbonate extracted with ethyl acetate. The compound 4 was obtained as a white solid after purification by means of silica gel column chromatography, ethyl acetate: petroleum ether (1:9) with a yield of 18 %.

Mp: 286°C;

^{1}H NMR (500 MHz, $CDCl_3$, ppm): δ = 8.61 (d, J = 10 Hz, 1H), 8.13 (d, J = 10 Hz, 1H), 7.6 (m, J = 55 Hz, 2H), 4.17 (m, J = 20 Hz, 2H), 1.53 (t, J = 15 Hz, 3H);
^{13}C NMR (125 MHz, $CDCl_3$, ppm): δ = 150.52, 143.84, 134.69, 126.8, 123.18, 102.19, 69.91, 61.06, 14.72.

HRMS (ESI): m/z calculated for $C_{40}H_{42}Br_2NaO_8$ $[(M+Na)^+]$: 833.1139; found: 833.1110

2.5 Appendix

2.5.1. Materials and Methods

All chemicals were obtained from commercial suppliers and used as received without further purification. All reactions were carried out in oven-dried glassware prior to use and wherever necessary, were performed under dry nitrogen in dried, anhydrous solvents using standard gastight syringes, cannula, and septa. Solvents were dried and distilled by standard laboratory purification techniques. TLC analyses were performed on recoated aluminum plates of silica gel 60 F254 plates (0.25 mm, Merck) and developed TLC plates were visualized under short and long wavelength UV lamps. Flash column chromatography was performed using silica gel of 200-400 mesh employing a solvent polarity correlated with the TLC mobility observed for the substance of interest. Yields refer to chromatographically and spectroscopically homogenous substances. ^{1}H NMR spectra was measured on a 500 MHz Bruker avance DPX spectrometer. Internal standard used for ^{1}H NMR is tetramethyl silane (TMS). High resolution mass spectra (HRMS) were recorded on Thermo scientific Q exactive mass spectrometer using electrospray ionization (ESI) technique. Absorption spectra was recorded on Shimadzu UV-3600 UV-VIS-NIR spectrometer and the Kubelka-Munk transformed reflectance spectra in the crystalline state were measured in the diffuse reflectance mode.[51] The diffuse reflectance spectra was used to find band gap from Tauc plot. The Kubelka-Munk model is quite accurate when the particle size is smaller or similar to the wavelength of the excitation. The diffuse reflectance spectra allows no separation of the reflection, refraction and diffraction occurring from the crystalline samples. As a result, the diffuse reflectance spectra is not as sensitive compared to the UV-vis absorption spectra and can possibly be broader as compared to the typical absorbance and fluorescence excitation spectra.

2.5.2. X-ray Crystallography

High quality single crystals of NTB_2 were used for X-ray diffraction experiments. Single crystal was mounted using oil (Infineum V8512) on a glass fiber. All measurements were made on a CCD area detector with graphite monochromated Mo Kα radiation. The data was collected using Bruker APEXII detector and processed using APEX2 from Bruker. The data was collected using Bruker kappa ApexII-diffractometer equipped with APEXII CCDC detector and processed using APEX2 from Bruker. The structure was solved by direct method and expanded using Fourier technique. The non-hydrogen atoms were refined anisotropically. Hydrogen atoms were included in idealized

positions, but not refined. Their positions were constrained relative to their parent atom using the appropriate HFIX command in SHELX-2018.[52] All programs used during the crystal structure analysis are incorporated in the WINGX software.[53] The full validation of CIF and structure factor of NT crystals were performed using the checkCIF utility and found to be free of major alert levels. Three dimensional structure visualization and the exploration of the crystal packing of crystals under study were carried out using Mercury 4.0.[54]

2.5.3. Computational Analyses

The ground-state optimized structure, dipole moments, reorganization energies, and frontier molecular orbitals were calculated using density functional theory (DFT) at ωB97XD functional and Def2- TZVP basis set[55] in Gaussian 09 and 16 suite.[56]

2.5.4. Quantum Theory of Atoms and Molecules[57]

The wave function generation for NTB_2 molecule was carried out at ωB97XD/Def2-TZVP level of theory using Gaussian09 and Gaussian16. Quantum theory of atoms in molecules (QTAIM) analyses helps to understand the description of interatomic interaction in the single crystal X-ray structure. A bond is defined along the bond line between two nuclei, called a bond path, along which electron density is concentrated. The (3, -1) bond critical point (BCP) is a point along the bond path at the interatomic surface, where the shared electron density reaches a minimum. (3, +1) ring critical point (RCP) and (3, +3) cage critical point (CCP) represents critical points in the ring and cage respectively where the electron density is minimum. The physical characteristics of the critical points [the electron density at BCP, RCP and CCP, $\rho(r)$, and its Laplacian, $\nabla^2\rho(r)$ reveal the approximate measure of the amount of electron density built up in the bonding region and as such could be taken as characteristic of the bond. When $\nabla^2\rho(r)<0$ and is large in magnitude, $\rho(r)$ is also large which means that there is a concentration of electronic charge in the internuclear region. This is also an indication of a sharing of electronic charge between both nuclei that defines the covalent (polar) bond. When $\nabla^2\rho(r)>0$ there is a depletion of electronic charge in the internuclear region and it indicates a closed shell interaction. Using the AIMAll software package, the electron density was integrated over atomic basins according to the quantum theory of atoms in molecules using PROAIM, and thus the BCP, RCP, CCP data and the molecular graphs were obtained.

2.5.5. Hirshfeld Analyses[34]

Important intermolecular interactions within the structure of NTB_2 crystal were identified through Hirshfeld surface analysis using CrystalExplorer17. The Hirshfeld surface is defined as a set of points in 3D space where the ratio of promolecule and procrystal electron densities is equal to 0.5. The exploration of intermolecular contacts is provided by mapping normalized contact distances (d_{norm}), which is a function of a closest distance from the point to the nuclei interior (d_i) and exterior (d_e) to the surface as well as on the van der Waals radii (r_{vdw}). 2D fingerprint plots derived from the Hirshfeld surface analyses, by plotting the fraction of points on the surface as the function of d_i and d_e, provides a visual summary of intermolecular contacts within the crystal.

2.5.6. Electrostatic Surface Potential[58]

Electrostatic surface potential (ESP) map illustrates the charge distribution of molecules in three dimension. These maps allow us to visualize variably charged regions of a molecule. Knowledge of the charge distributions can be used to determine how molecules interact with one another. Gaussian supports the cube keyword to generate the cubes separately from the formatted checkpoint file (generated from energy calculation with ωB97XD/Def2-TZVP level of theory) using the cubegen utility program. This allows for the generation of electrostatic surface potential mapping of the molecule.

2.5.7. Non Covalent Interaction[35]

NCI analysis employs an index based on electron density and its derivatives to identify noncovalent interactions. A two-dimensional plot of reduced electron density (s) against electron density (ρ) and the critical points are associated with the troughs appearing in the plot. Reduced electron density is given by:

$$s = \frac{1}{2(3\pi^2)^{1/3}\rho^{4/3}} |\nabla\rho|$$

Noncovalent interactions occur in the real space points where these troughs appear. The sign of second derivative of $\rho(\nabla^2\rho)$ is analyzed to distinguish attractive and repulsive interactions. The noncovalent interaction regions are represented in the plot as discs with color ranging from blue (attractive) to red (repulsive) as in the VIBGYOR spectrum.

2.5.8. Natural Bond Orbital Analysis[59,60]

The natural bond orbital (NBO) analyses was performed at the ωB97XD/Def2-TZVP level of theory, by means of the Gaussian 16 calculation package. The orbital donor-acceptor interactions are assessed by probing all possible interactions between occupied (donor) Lewis-type NBOs and unoccupied (acceptor) non-Lewis NBOs by second-order perturbation theory. For each donor NBO (i) and acceptor NBO (j), the stabilization energy E(2) associated with delocalization from the filled NBOs into the unoccupied non-Lewis orbitals is estimated.

2.5.9. Symmetry Adapted Perturbation Theory (SAPT)[37]

SAPT(0) analysis was employed to determine the noncovalent interaction energies of dimer molecules. The SAPT module of the psi4 code was employed, with jun-cc-pVDZ basis set. SAPT(0) calculations provide the contributing components of interaction energy. The results obtained from SAPT(0) analysis is a second order perturbation expansion constituting first order electrostatic and exchange energy parts and second order dispersion, induction and their exchange counterparts as the perturbation terms

$$E_{int}^{Sapt(0)} = E_{elc}^{(1)} + E_{ex}^{(1)} + E_{ind}^{(2)} + E_{ind-ex}^{(2)} + E_{dis}^{(2)} + E_{dis-ex}^{(2)}$$

2.5.10. Interacting Quantum Atoms (IQA):[61]

IQA approach was done on NTB_2 using AIMALL software to understand the nature of intermolecular interactions. Hamiltonian is partitioned into physical atomic and interatomic contributions. The energy decomposition computed using partitioned Hamiltonian is consistent with the topological method of quantum theory of atoms in molecules contribution values determine the nature of intermolecular or intramolecular interactions.

The total interatomic energy (E_t^{AB}) is the summation of interparticle [electron (e) and nucleus (n)] interaction energies, which is given by

$$E_t^{AB} = E_{nn}^{AB} + E_{en}^{AB} + E_{ne}^{AB} + E_{ee}^{AB}$$

where the electron-electron interaction is the summation of exchange (E_X^{AB}), correlation (E_C^{AB}) and coulomb (E_{Coul}^{AB}) potentials:

$$E_{ee}^{AB} = E_X^{AB} + E_C^{AB} + E_{coul}^{AB}$$

Now, as per IQA, the classical component (E_{cl}^{AB}) is the union of all the electrostatic terms

$$E_{cl}^{AB} = E_{nn}^{AB} + E_{en}^{AB} + E_{ne}^{AB} + E_{Coul}^{AB}$$

and the exchange-correlation component consists of all the quantum terms

$$E_{XC}^{AB} = E_X^{AB} + E_C^{AB}$$

Thus, total interatomic interaction energy is decomposed into classical and quantum terms separately

$$E_t^{AB} = E_{cl}^{AB} + E_{XC}^{AB}$$

2.5.11. Charge Transport and Mobility Calculations

Electron and hole transfer coupling values were calculated by employing the CATNIP Tool version 1.9.[62] with post processed Gaussian 16 output files. The charge transport simulation was carried out based on the first-principles quantum mechanics calculations and Marcus theory.[63] The charge transfer rate (k_i), representing the rate of hole/electron hopping from a monomer to the ith neighbor was obtained through Marcus-Hush equation:

$$k_i = \frac{{V_{e/h}}^2}{\hbar}\left(\frac{\pi}{\lambda_{e/h} k_B T}\right)^{\frac{1}{2}} \exp\left(-\frac{\lambda_{e/h}}{4 k_B T}\right)$$

where V_e and V_h are the electron and hole transfer coupling between the monomers of a dimer, k_B is the Boltzmann constant and T is the temperature (300 K). The intramolecular reorganization energy necessary for a neutral molecule to convert into an anion, electron reorganizing energy (λ_e) was found to be lower than the energy needed for the molecule to reorganize itself to a cation, hole reorganizing energy (λ_h). The $\lambda_{e/h}$ were found using the following formula:

$$\lambda_h = (E_0^* - E_0) + (E_+^* - E_+)$$

$$\lambda_e = (E_0^* - E_0) + (E_-^* - E_-)$$

E_0 and $E_{\pm}^*$ are the lowest energies of neutral and cationic/anionic species respectively. E_0^* is the energy of the neutral molecule at cation geometry for λ_h and anion geometry for λ_e. $E_{\pm}^*$ is the energy of the anionic/cationic state at neutral geometry. Drift mobility (μ) was calculated employing Einstein's relation:

$$\mu = \frac{1}{6}\frac{e}{k_B T}\sum_i r_i^2 k_i P_i$$

The anisotropic mobility was calculated using the following formula:

$$\mu_\phi = \frac{e}{2k_B T}\sum_i k_i r_i^2 P_i \cos^2\gamma_i cos^2(\theta_i - \phi)$$

where γ_i is the angle between the charge hopping pathway and plane of interest, ϕ is the orientation angle of the transport channel relative to the reference axis and θ_i is the angles between the projected hopping paths of different dimers and the reference axis. The charge hopping probability (P_i) is given by:

$$P_i = \frac{k_i}{\sum_i k_i}$$

2.5.12. UV-vis Absorption Spectroscopy

Absorption spectra was recorded on Shimadzu UV-3600 UV-vis-NIR spectrometer at a wavelength range of 200-800 nm, and the Kubelka-Munk transformed reflectance spectra in the crystalline state were measured in the diffuse reflectance mode.[51] The optical band gap (E_g) of NTB_2 was calculated by the Tauc[64] method using the equation below,

$$(\alpha.h\nu)^{1/\gamma} = B(h\nu - E_g)$$

where α is the absorption coefficient, h is the Planck constant, ν is the photon's frequency, E_g is the band gap energy, and B is a constant. The γ factor indicates the nature of electron transition with a value of ½ for direct band gap and a value of 2 for indirect band gap.

2.5.13. Band Structure and Density of States (DOS)

Calculations based on DFT was implemented in the Quantum Espresso (QE) package.[65] Total energy and electronic structure calculations have been performed using Plane-Wave Self-Consistent Field package, a component of the Quantum Espresso distribution. The exchange-correlation interactions are treated within the generalized gradient approximation of the Perdew-Burke-Ernzerhof type.[66,67] The interaction between the valence electron and the ionic core was

represented by ultrasoft pseudopotentials. Van der Waals (vdW) interactions were corrected using the DFT-D method.[68,69] The kinetic energy cutoff for wavefunction was set to 50 Ry, which was obtained after convergence test. A k-mesh of 4×4×4 was adopted to sample the first Brillouin zone. Convergence threshold for self-consistent calculations was set to 10^{-8}. After a self-consistent calculation, a non-self-consistent calculation was performed in same conditions and with a k-mesh of 8×8×8. To analyze the data, QE components such as dos, projwfc and bands were used to compute total density of states (TDOS), partial density of states (PDOS) and band structure. The high symmetry k points of the Brillouin zone for band structure, were calculated using SeeK-path: the k-path finder and visualizer.[70–72]

2.5.14. Scanning Electron Microscopy (SEM)

For SEM measurements, 1 mM NTB_2 in acetonitrile were drop casted and air dried on the flat surface of cylindrical copper stubs. The surface morphology of all the samples was analyzed by using FE-SEM (Nova NanoSEM 450, FEI).

2.6. Reference

(1) Landschulz, W. H.; Johnson, P. F.; McKnight, S. L. The Leucine Zipper: A Hypothetical Structure Common to a New Class of DNA Binding Proteins. *Science* **1988**, *240*, 1759–1764.

(2) Bisson, A. P.; Carver, F. J.; Hunter, C. A.; Waltho, J. P. Molecular Zippers. *Journal of the American Chemical Society* **1994**, *116*, 10292–10293.

(3) Kortmann, J.; Narberhaus, F. Bacterial RNA Thermometers: Molecular Zippers and Switches. *Nature Reviews Microbiology 2012 10:4* **2012**, *10*, 255–265.

(4) Meng, L.; Liu, C.; Lü, J.; Zhao, Q.; Deng, S.; Wang, G.; Qiao, J.; Zhang, C.; Zhen, L.; Lu, Y.; Li, W.; Zhang, Y.; Pestell, R. G.; Fan, H.; Chen, Y.-H.; Liu, Z.; Yu, Z. Small RNA Zippers Lock MiRNA Molecules and Block MiRNA Function in Mammalian Cells. *Nature Communications* **2017**, *8*, 13964.

(5) Zhou, M.; Bentley, D.; Ghosh, I. Helical Supramolecules and Fibers Utilizing Leucine Zipper-Displaying Dendrimers. *Journal of the American Chemical Society* **2004**, *126*, 734–735.

(6) Fukushima, T.; Horike, S.; Inubushi, Y.; Nakagawa, K.; Kubota, Y.; Takata, M.; Kitagawa,

S.; Fukushima, T.; Horike, S.; Nakagawa, K.; Kitagawa, S.; Kubota, Y.; Takata, M. Solid Solutions of Soft Porous Coordination Polymers: Fine-Tuning of Gas Adsorption Properties. *Angewandte Chemie International Edition* **2010**, *49*, 4820–4824.

(7) Teng, P.; Niu, Z.; She, F.; Zhou, M.; Sang, P.; Gray, G. M.; Verma, G.; Wojtas, L.; van der Vaart, A.; Ma, S.; Cai, J. Hydrogen-Bonding-Driven 3D Supramolecular Assembly of Peptidomimetic Zipper. *Journal of the American Chemical Society* **2018**, *140*, 5661–5665.

(8) Sisson, A. L.; Sakai, N.; Banerji, N.; Fürstenberg, A.; Vauthey, E.; Matile, S. Zipper Assembly of Vectorial Rigid-Rod π-Stack Architectures with Red and Blue Naphthalenediimides: Toward Supramolecular Cascade n/p-Heterojunctions. *Angewandte Chemie International Edition* **2008**, *47*, 3727–3729.

(9) Kim, H. W.; Jung, J.; Han, M.; Lim, S.; Tamada, K.; Hara, M.; Kawai, M.; Kim, Y.; Kuk, Y. One-Dimensional Molecular Zippers. *Journal of the American Chemical Society* **2011**, *133*, 9236–9238.

(10) Lin, Y.; Fan, H.; Li, Y.; Zhan, X. Thiazole-Based Organic Semiconductors for Organic Electronics. *Advanced Materials* **2012**, *24*, 3087–3106.

(11) Ramakrishnan, R.; Niyas, M. A.; Lijina, M. P.; Hariharan, M. Distinct Crystalline Aromatic Structural Motifs: Identification, Classification, and Implications. *Accounts of Chemical Research* **2019**, *52*, 3075–3086.

(12) Niyas, M. A.; Ramakrishnan, R.; Vijay, V.; Hariharan, M. Structure-Packing-Property Correlation of Self-Sorted Versus Interdigitated Assembly in TTF·TCNQ-Based Charge-Transport Materials. *Chemistry - A European Journal* **2018**, *24*, 12318–12329.

(13) Tang, M. L.; Bao, Z. Halogenated Materials as Organic Semiconductors. *Chemistry of Materials* **2011**, *23*, 446–455.

(14) Clark, T.; Hennemann, M.; Murray, J. S.; Politzer, P. Halogen Bonding: The σ-Hole. *Journal of Molecular Modeling* **2007**, *13*, 291–296.

(15) Meazza, L.; Foster, J. A.; Fucke, K.; Metrangolo, P.; Resnati, G.; Steed, J. W. Halogen-Bonding-Triggered Supramolecular Gel Formation. *Nature Chemistry* **2013**, *5*, 42–47.

(16) Rama Krishna, G.; Devarapalli, R.; Lal, G.; Malla Reddy, C. Mechanically Flexible Organic Crystals Achieved by Introducing Weak Interactions in Structure: Supramolecular Shape Synthons. **2016**.

(17) Hein, R.; Li, X.; Beer, P. D.; Davis, J. J. Enhanced Voltammetric Anion Sensing at Halogen and Hydrogen Bonding Ferrocenyl SAMs. *Chemical Science* **2021**.

(18) Niyas, M. A.; Ramakrishnan, R.; Vijay, V.; Sebastian, E.; Hariharan, M. Anomalous Halogen–Halogen Interaction Assists Radial Chromophoric Assembly. *Journal of the American Chemical Society* **2019**, *141*, 4536–4540.

(19) Liu, C.-Z.; Koppireddi, S.; Wang, H.; Zhang, D.-W.; Li, Z.-T. Halogen Bonding Directed Supramolecular Quadruple and Double Helices from Hydrogen-Bonded Arylamide Foldamers. *Angewandte Chemie, International Edition* **2019**, *58*, 226–230.

(20) Parker, A. J.; Stewart, J.; Donald, K. J.; Parish, C. A. Halogen Bonding in DNA Base Pairs. *J. Am. Chem. Soc* **2012**, *134*.

(21) Politzer, P.; Murray, J. S.; Clark, T. Halogen Bonding: An Electrostatically-Driven Highly Directional Noncovalent Interaction. *Physical Chemistry Chemical Physics* **2010**, *12*, 7748–7757.

(22) Bartashevich, E.; Troitskaya, E.; Pendas, A. M.; Tsirelson, V. Understanding the Bifurcated Halogen Bonding N···Hal···N in Bidentate Diazaheterocyclic Compounds. *Computational & Theoretical Chemistry* **2015**, *1053*, 229–237.

(23) Novak, M.; Foroutan-Nejad, C.; Marek, R. Asymmetric Bifurcated Halogen Bonds. *Physical Chemistry Chemical Physics* **2015**, *17*, 6440–6450.

(24) Wang, C.; Danovich, D.; Mo, Y.; Shaik, S. On The Nature of the Halogen Bond. *Journal of Chemical Theory and Computation* **2014**, *10*, 3726–3737.

(25) Stone, A. J. Are Halogen Bonded Structures Electrostatically Driven?. *Journal of the American Chemical Society* **2013**, *135*, 7005–7009.

(26) Cavallo, G.; Metrangolo, P.; Milani, R.; Pilati, T.; Priimagi, A.; Resnati, G.; Terraneo, G. The Halogen Bond. *Chemical Reviews (Washington, DC, United States)* **2016**, *116*, 2478–2601.

(27) Sessler, J. L.; Lawrence, C. M.; Jayawickramarajah, J. Molecular Recognition via Base-Pairing. *Chemical Society Reviews* **2007**, *36*, 314–325.

(28) Yoshida, S.; Yano, T.; Nishiyama, Y.; Misawa, Y.; Kondo, M.; Matsushita, T.; Igawa, K.; Tomooka, K.; Hosoya, T. Thiazolobenzyne: A Versatile Intermediate for Multisubstituted Benzothiazoles. *Chemical Communications* **2016**, *52*, 11199–11202.

(29) Batsanov, S. S. Van Der Waals Radii of Elements. *Inorganic Materials (Translation of Neorganicheskie Materialy)* **2001**, *37*, 871–885.

(30) Bondi, A. Van Der Waals Volumes and Radii. *The Journal of Physical Chemistry* **1964**, *68*, 441–451.

(31) Lieberman, H. F.; Davey, R. J.; Newsham, D. M. T. Br···Br and Br···H Interactions in Action: Polymorphism, Hopping, and Twinning in 1,2,4,5-Tetrabromobenzene. *Chemistry of Materials* **2000**, *12*, 490–494.

(32) Balmohammadi, Y.; Khavasi, H. R.; Naghavi, S. S. Existence of Untypical Halogen-Involving Interactions in Crystal Packings: A Statistical and First-Principles Study. *CrystEngComm* **2020**, *22*, 2756–2765.

(33) Vologzhanina, A. V.; Buikin, P. A.; Korlyukov, A. A. Peculiarities of Br···Br Bonding in Crystal Structures of Polybromides and Bromine Solvates. *CrystEngComm* **2020**, *22*, 7361–7370.

(34) Spackman, M. A.; Jayatilaka, D. Hirshfeld Surface Analysis. *CrystEngComm* **2009**, *11*, 19–32.

(35) Contreras-García, J.; Johnson, E. R.; Keinan, S.; Chaudret, R.; Piquemal, J.-P.; Beratan, D. N.; Yang, W. NCIPLOT: A Program for Plotting Noncovalent Interaction Regions. *Journal of Chemical Theory and Computation* **2011**, *7*, 625–632.

(36) Bader, R. F. W. A Quantum Theory of Molecular Structure and Its Applications. *Chemical Reviews* **1991**, *91*, 893–928.

(37) Szalewicz, K. Symmetry-Adapted Perturbation Theory of Intermolecular Forces. *Wiley Interdisciplinary Reviews: Computational Molecular Science* **2012**, *2*, 254–272.

(38) Johnson, E. R.; Keinan, S.; Mori-Sánchez, P.; Contreras-García, J.; Cohen, A. J.; Yang, W. Revealing Noncovalent Interactions. *Journal of the American Chemical Society* **2010**, *132*, 6498–6506.

(39) Mohan, A.; Sasikumar, D.; Bhat, V.; Hariharan, M. Metastable Chiral Azobenzenes Stabilized in a Double Racemate. *Angewandte Chemie International Edition* **2020**, *59*, 3201–3208.

(40) Reed, A. E.; Curtiss, L. A.; Weinhold, F. Intermolecular Interactions from a Natural Bond Orbital, Donor—Acceptor Viewpoint. *Chemical Reviews* **1988**, *88*, 899–926.

(41) Wuerthner, F. Dipole-Dipole Interaction Driven Self-Assembly of Merocyanine Dyes: From Dimers to Nanoscale Objects and Supramolecular Materials. *Accounts of Chemical Research* **2016**, *49*, 868–876.

(42) Vijay, V.; Ramakrishnan, R.; Hariharan, M. Halogen–Halogen Bonded Donor-Acceptor Stacks Foster Orthogonal Electron and Hole Transport. *Crystal Growth & Design* **2021**, *21*, 200–206.

(43) Dey, A.; Desiraju, G. R. Correlation between Molecular Dipole Moment and Centrosymmetry in Some Crystalline Diphenyl Ethers. *Chemical Communications* **2005**, No. 19, 2486.

(44) Govaerts, K.; Saniz, R.; Partoens, B.; Lamoen, D. Van Der Waals Bonding and the Quasiparticle Band Structure of SnO from First Principles. *Physical Review B* **2013**, *87*, 235210.

(45) Burke, K. Perspective on Density Functional Theory. *The Journal of Chemical Physics* **2012**, *136*, 150901.

(46) Christensen, N. E.; Svane, A.; Peltzer Y Blancá, E. L. Electronic and Structural Properties of SnO under Pressure. *Physical Review B - Condensed Matter and Materials Physics* **2005**, *72*, 014109.

(47) Sze, S.M. and Ng, K. K. *Physics of Semiconductor Devices*; 2006.

(48) Deng, W. Q.; Goddard, W. A. Predictions of Hole Mobilities in Oligoacene Organic Semiconductors from Quantum Mechanical Calculations. *Journal of Physical Chemistry B* **2004**, *108*, 8614–8621.

(49) Sebastian, E.; Philip, A. M.; Benny, A.; Hariharan, M. Null Exciton Splitting in Chromophoric Greek Cross (+) Aggregate. *Angewandte Chemie International Edition* **2018**, *57*, 15696–15701.

(50) Giannini, S.; Carof, A.; Blumberger, J. Crossover from Hopping to Band-Like Charge Transport in an Organic Semiconductor Model: Atomistic Nonadiabatic Molecular Dynamics Simulation. *Journal of Physical Chemistry Letters* **2018**, *9*, 3116–3123.

(51) Zhang, Y.; Sun, J.; Zhuang, G.; Ouyang, M.; Yu, Z.; Cao, F.; Pan, G.; Tang, P.; Zhang, C.; Ma, Y. Heating and Mechanical Force-Induced Luminescence on-off Switching of Arylamine Derivatives with Highly Distorted Structures. *Journal of Materials Chemistry C* **2014**, *2*, 195–200.

(52) Sheldrick, G. M. Crystal Structure Refinement with SHELXL. *Acta Crystallographica Section C: Structural Chemistry* **2015**, *71*, 3–8.

(53) Farrugia, L. J. WinGX Suite for Small-Molecule Single-Crystal Crystallography. *Journal of Applied Crystallography* **1999**, *32*, 837–838.

(54) Macrae, C. F.; Sovago, I.; Cottrell, S. J.; Galek, P. T. A.; McCabe, P.; Pidcock, E.; Platings, M.; Shields, G. P.; Stevens, J. S.; Towler, M.; Wood, P. A. Mercury 4.0 : From Visualization to Analysis, Design and Prediction. *Journal of Applied Crystallography* **2020**, *53*, 226–235.

(55) Kozuch, S.; Martin, J. M. L. Halogen Bonds: Benchmarks and Theoretical Analysis. *Journal of Chemical Theory and Computation* **2013**, *9*, 1918–1931.

(56) Frisch, M. J.; Trucks, G. W.; Schlegel, H. B.; Scuseria, G. E.; Robb, M. a.; Cheeseman, J. R.; Scalmani, G.; Barone, V.; Petersson, G. a.; Nakatsuji, H.; Li, X.; Caricato, M.; Marenich, a. V.; Bloino, J.; Janesko, B. G.; Gomperts, R.; Mennucci, B.; Hratchian, H. P.; Ortiz, J. V.; Izmaylov, a. F.; Sonnenberg, J. L.; Williams; Ding, F.; Lipparini, F.; Egidi, F.; Goings, J.; Peng, B.; Petrone, A.; Henderson, T.; Ranasinghe, D.; Zakrzewski, V. G.; Gao, J.; Rega, N.; Zheng, G.; Liang, W.; Hada, M.; Ehara, M.; Toyota, K.; Fukuda, R.; Hasegawa, J.; Ishida, M.; Nakajima, T.; Honda, Y.; Kitao, O.; Nakai, H.; Vreven, T.; Throssell, K.; Montgomery Jr., J. a.; Peralta, J. E.; Ogliaro, F.; Bearpark, M. J.; Heyd, J. J.; Brothers, E. N.; Kudin, K. N.; Staroverov, V. N.; Keith, T. a.; Kobayashi, R.; Normand, J.; Raghavachari, K.; Rendell, a. P.; Burant, J. C.; Iyengar, S. S.; Tomasi, J.; Cossi, M.; Millam, J. M.; Klene, M.; Adamo, C.; Cammi, R.; Ochterski, J. W.; Martin, R. L.; Morokuma, K.; Farkas, O.; Foresman, J. B.; Fox, D. J. G16_C01. 2016, p Gaussian 16, Revision C.01, Gaussian, Inc., Wallin.

(57) Bader, R. F. W. A Quantum Theory of Molecular Structure and Its Applications. *Chemical Reviews* **1991**, *91*, 893–928.

(58) Wang, H.; Wang, W.; Jin, W. J. σ-Hole Bond vs π-Hole Bond: A Comparison Based on Halogen Bond. *Chemical Reviews (Washington, DC, United States)* **2016**, *116*, 5072–5104.

(59) Reed, A. E.; Curtiss, L. A.; Weinhold, F. Intermolecular Interactions from a Natural Bond Orbital, Donor-Acceptor Viewpoint. *Chemical Reviews* **1988**, *88*, 899–926.

(60) Weinhold, F. Natural Bond Orbital Analysis: A Critical Overview of Relationships to Alternative Bonding Perspectives. *Journal of Computational Chemistry* **2012**, *33*, 2363–2379.

(61) Blanco, M. A.; Pendás, A. M.; Francisco, E. Interacting Quantum Atoms: A Correlated Energy Decomposition Scheme Based on the Quantum Theory of Atoms in Molecules. *Journal of Chemical Theory and Computation* **2005**, *1*, 1096–1109.

(62) GitHub - JoshuaSBrown/QC_Tools: This small repository provides functionality for calculating the charge transfer integrals between two molecules.

(63) Deng, W.-Q.; Sun, L.; Huang, J.-D.; Chai, S.; Wen, S.-H.; Han, K.-L. Quantitative Prediction of Charge Mobilities of π-Stacked Systems by First-Principles Simulation. *Nature Protocols* **2015**, *10*, 632–642.

(64) Tauc, J.; Grigorovici, R.; Vancu, A. Optical Properties and Electronic Structure of

Amorphous Germanium. *physica status solidi (b)* **1966**, *15*, 627–637.

(65) Giannozzi, P.; Baroni, S.; Bonini, N.; Calandra, M.; Car, R.; Cavazzoni, C.; Ceresoli, D.; Chiarotti, G. L.; Cococcioni, M.; Dabo, I.; Dal Corso, A.; De Gironcoli, S.; Fabris, S.; Fratesi, G.; Gebauer, R.; Gerstmann, U.; Gougoussis, C.; Kokalj, A.; Lazzeri, M.; Martin-Samos, L.; Marzari, N.; Mauri, F.; Mazzarello, R.; Paolini, S.; Pasquarello, A.; Paulatto, L.; Sbraccia, C.; Scandolo, S.; Sclauzero, G.; Seitsonen, A. P.; Smogunov, A.; Umari, P.; Wentzcovitch, R. M. QUANTUM ESPRESSO: A Modular and Open-Source Software Project for Quantum Simulations of Materials. *Journal of Physics Condensed Matter* **2009**, *21*.

(66) Perdew, J. P.; Ruzsinszky, A.; Csonka, G. I.; Vydrov, O. A.; Scuseria, G. E.; Constantin, L. A.; Zhou, X.; Burke, K. Erratum: Restoring the Density-Gradient Expansion for Exchange in Solids and Surfaces (Physical Review Letters (2008) 100 (136406)). *Physical Review Letters*. American Physical Society January 2009, p 039902.

(67) Perdew, J. P.; Burke, K.; Ernzerhof, M. Generalized Gradient Approximation Made Simple. *Physical Review Letters* **1996**, *77*, 3865–3868.

(68) Grimme, S. Semiempirical GGA-Type Density Functional Constructed with a Long-Range Dispersion Correction. *Journal of Computational Chemistry* **2006**, *27*, 1787–1799.

(69) Barone, V.; Casarin, M.; Forrer, D.; Pavone, M.; Sambi, M.; Vittadini, A. Role and Effective Treatment of Dispersive Forces in Materials: Polyethylene and Graphite Crystals as Test Cases. *Journal of Computational Chemistry* **2009**, *30*, 934–939.

(70) Hinuma, Y.; Pizzi, G.; Kumagai, Y.; Oba, F.; Tanaka, I. Band Structure Diagram Paths Based on Crystallography. *Computational Materials Science* **2017**, *128*, 140–184.

(71) Togo, A.; Tanaka, I. $\texttt{Spglib}$: A Software Library for Crystal Symmetry Search. *arXiv:1808.01590 [cond-mat]* **2018**, 1–11.

(72) Hjorth Larsen, A.; JØrgen Mortensen, J.; Blomqvist, J.; Castelli, I. E.; Christensen, R.; Dułak, M.; Friis, J.; Groves, M. N.; Hammer, B.; Hargus, C.; Hermes, E. D.; Jennings, P. C.; Bjerre Jensen, P.; Kermode, J.; Kitchin, J. R.; Leonhard Kolsbjerg, E.; Kubal, J.; Kaasbjerg, K.; Lysgaard, S.; Bergmann Maronsson, J.; Maxson, T.; Olsen, T.; Pastewka, L.; Peterson, A.; Rostgaard, C.; SchiØtz, J.; Schütt, O.; Strange, M.; Thygesen, K. S.; Vegge, T.; Vilhelmsen, L.; Walter, M.; Zeng, Z.; Jacobsen, K. W. The Atomic Simulation Environment - A Python Library for Working with Atoms. *Journal of Physics Condensed Matter*. Institute of Physics Publishing June 2017.

Chapter 3

The Effect of Single-Atom Substitution on Structure and Band Gap in Organic Semiconductors

Abstract: We systematically altered the molecular structure of 5-methoxynaphtho[1,2-*d*]thiazole (NTH) by replacing the terminal hydrogen atom with halogens (Cl, Br, I) to study the effect of single-atom substitution in modulating the crystal packing and optical band gap. The parent compound (NTH) and Br and I derivatives of NTH crystallized in the same space group, wherein only Br- and I-substituted molecular crystals displayed isostructural interaction topologies. The crystal-packing similarities in structurally equivalent motifs were established using the numerical descriptors isostructurality (I_s) and cell similarity (π) indices. An energy framework analysis was implemented to obtain a qualitative picture of the 3D topology displaying the predominant interactions in supramolecular architectures of the NTH derivatives. A decrease in optical band gap from 3.48 to 3.07 eV was observed with an increasing atomic number of halogens in NTH derivatives, signifying the direct role of halogen atoms in the electronic properties of organic crystals. The reduction of the optical band gap in 5-methoxynaphtho[1,2-*d*]thiazole derivatives was visualized from the band structure and projected density of states obtained by employing DFT calculations. The outcome suggests the potential of halogenation in tailoring the optoelectronic properties of organic functional materials.

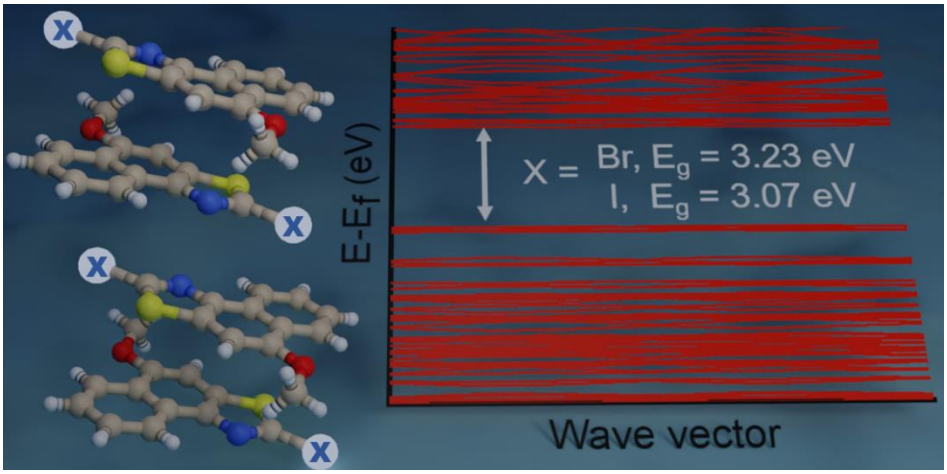

3.1. Introduction

The past two decades have witnessed enormous growth in the field of electronics and technology. The introduction of band structure engineering in organic semiconducting materials has attracted intense interest.[1,2] Organic semiconductors serve as energy-efficient materials[3] in fabricating organic photovoltaics (OPVs),[4] organic field-effect transistors (OFET),[5] and organic light-emitting diodes (OLEDs)[6] by fine-tuning the energy levels of the frontier molecular orbitals.[7] Small-molecule-based OPVs have high open circuit voltage, high mobility, and more easily controlled synthetic routes to produce diverse technologies comparable to those of polymer-based OPVs.[8] The optoelectronic properties can be tailored by regulating the packing arrangements, which are governed by the chemical composition and intermolecular interactions of the crystalline solids.[9] Halogenation is a widely adapted strategy to alter the properties of optoelectronic devices by reducing the highest occupied molecular orbital (HOMO)−lowest unoccupied molecular orbital (LUMO) gap of π-conjugated materials.[10] The halogen atom exhibits a resonance-donating effect due to the existence of lone pairs and an electron-withdrawing effect due to electronegativity.[11] The band gaps in halogenated graphene derivatives were reported to be lowered with a decrease in the electronegativity of halogen substituents.[12]

The molecular packing in organic crystals dramatically influences the functional properties, but it is hard to speculate because of the intricate intermolecular interactions.[13] The retention of the packing arrangement despite single-atom/ functional-group substitution serves as a powerful tool for engineering biomimetic molecular assemblies.[14] In this regard, the phenomenon of isostructurality becomes essential to the prediction of the crystal structure and the synthesis of functional supramolecular assemblies.[15] Isostructurality is an effective tool to decipher the functional group's influence (shape, size, and electronic properties) in solid-state architecture.[16] Isostructurality in organic molecules is often manifested by an exchange of a few atoms or groups such as Cl/CH_3, Br/I, O−H/N−H, and C/N between structurally similar molecules.[17–19] Similar closepacking effects, van der Waals radii of atoms or groups, and more directional and anisotropic intermolecular interactions are imperative in constructing isostructural crystals. Optical band gap tuning in isostructural organic solids with detailed crystallographic studies on the structure-property relations remains elusive. Naphthalene is one of the most extensively used building blocks to construct conjugated materials for blue OLEDs.[20,21] Electron-accepting thiazole moieties and naphthalene-based organic materials have been used as semiconductors in organic electronics.[22,23] Our continuous efforts in exploring the origin of distinct crystalline supramolecular

architectures[13,24] of small organic molecules and their potential application as functional materials[25] motivated us to design a series of halogenated naphthothiazoles,[26] illustrating a systematic trend in optical band gap reduction, in the order of increasing atomic number of halogen atoms (Scheme 3.1). We designed novel bipolar naphthalene-based wide-band-gap semiconducting materials fused with an electron-withdrawing thiazole moiety and electron-donating halogen (Cl, Br, I) atom. Band-gap lowering in isostructural Br- and I-substituted crystals with an increase in the atomic number of halogen atoms conferred the effect of single-atom replacement on the optoelectronic properties of organic molecules at a molecular and supramolecular level.

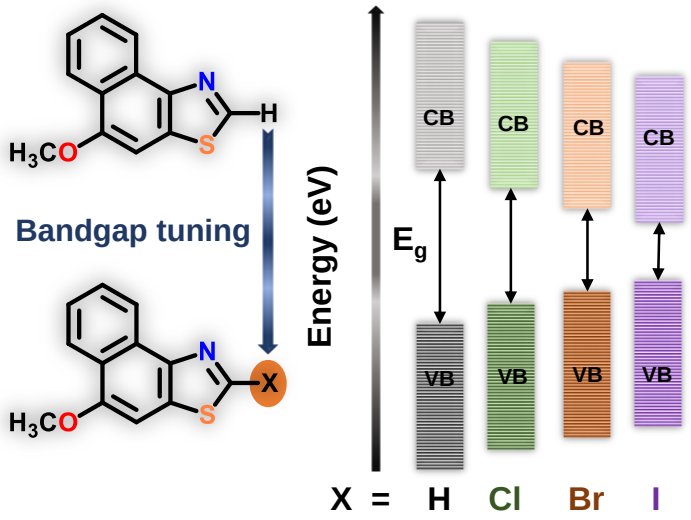

Scheme 3.1: Chemical structure and schematic representation of modulation in band gap via halogenation in 5- Methoxynaphtho[1,2-*d*]thiazole.

3.2. Results and Discussion

A Sandmeyer reaction on 5-methoxynaphtho[1,2-*d*]thiazol-2- amine followed by hydrogen and halogen substitution yielded 5- methoxynaphtho[1,2-*d*]thiazole (NTH), 2-chloro-5-methoxynaphtho[1,2-*d*]thiazole (NTC), 2-bromo-5-methoxynaphtho- [1,2-*d*]thiazole (NTB), and 2-iodo-5-methoxynaphtho[1,2-*d*]thiazole (NTI), respectively (Scheme 3.2).[27] Single crystals of naphthothiazole (NT) derivatives were obtained through slow evaporation from ethyl acetate. NTH, NTC, NTB, and NTI yielded solvent-free monoclinic crystal systems with space groups $P2_1/n$, Pn, $P2_1/n$, and $P2_1/n$, respectively (Table 3.1). Though NTH, NTB, and NTI crystallize in the same space group, only NTI and NTB crystals were found to have similar lattice parameters (Table 3.1). Qualitative single-crystal X-ray structure analyses were performed to study the interac-

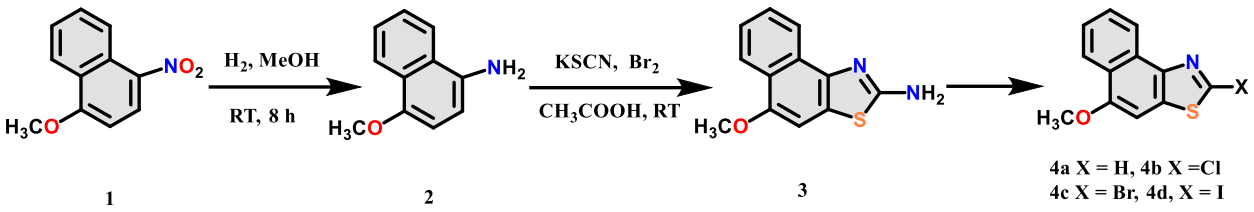

Scheme 3.2: Reaction scheme for the synthesis of NTH, NTC, NTB and NTI.

tions directing the packing arrangements of NTs. The packing arrangement in NTH is assisted by C−H•••N (d = 2.66 Å), π−π (d = 4.07 Å), and S•••C (d = 3.00 Å) interactions (Figure 3.2). Interactions such as Cl•••S (d = 3.55 Å), Cl•••O (d = 3.13 Å), π−π (d = 3.90 Å), and N•••C (d = 3.21 Å) supported the packing in NTC (Figure 3.2). The crystalline packing in NTB is facilitated by Br•••C (d = 3.62 Å), π−π (d = 3.46 Å), S•••C (d = 3.53 Å), C−H•••H−C (d = 2.41 Å), and C−H•••N (d = 2.77 Å) interactions (Figure 3.2). Weak interactions such as I•••C (d = 3.71 Å), π−π (d = 3.48 Å), S•••C (d = 3.48 Å), C−H•••H−C (d = 2.39 Å), and C−H•••N (d = 2.75 Å) aided the packing arrangement in NTI (Figure 3.2). Hirshfeld surface (HS),[28] Bader's quantum theory of atoms in molecules (QTAIM),[29] and noncovalent interaction (NCI)[30] analyses were performed to gain insight into the packing motifs and quantification of weak intermolecular interactions in crystalline NT derivatives. From the HS analysis, the ratio (ρ) of %C•••H to %C•••C interactions indicates that NTH (ρ = 1.24), NTC (ρ = 1.05), NTB (ρ = 1.4), and NTI (ρ = 1.4) exhibit a γ-packing motif (Table 3.2). All NTs had a dominant presence of H•••H interactions. Similar percentage contributions of the same interatomic contacts existed between NTB and NTI, possibly due to isostructurality in crystal packing. On comparison of the packing of NTs, it was found that NTI and NTB had similar packings composed of antiparallel stacked dimers. A close inspection of the intermolecular arrangement divulged identical packing motifs due to similar molecular features classifying NTI and NTB as isostructural crystals (Figure 3.3). However, the packing and lattice parameters of NTH and NTC were dissimilar, signifying they are not isostructural.

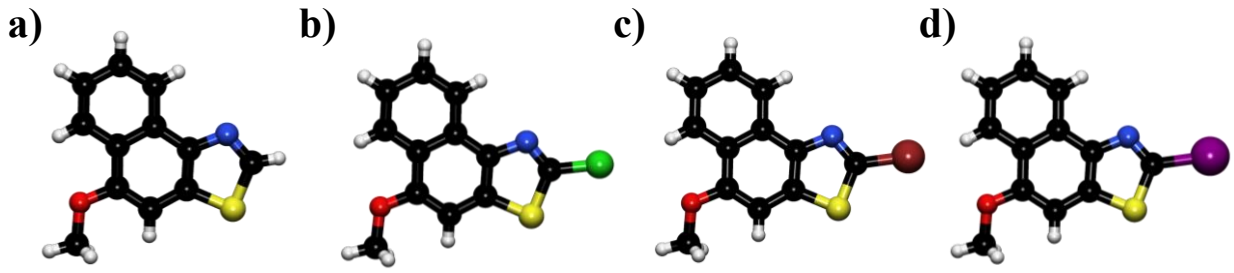

Figure 3.1: Crystal structure of a) NTH, b) NTC, c) NTB and d) of NTI.

Table 3.1. Crystallographic data and refinement process for NT derivatives.

Parameters	NTH	NTC	NTB	NTI
Formula	$C_{12}H_9NOS$	$C_{12}H_8ClNOS$	$C_{12}H_8BrNOS$	$C_{12}H_8INOS$
Formula weight	215.26	249.70	294.16	341.15
Color	Colorless	Colorless	Colorless	Colorless
Crystal system	Monoclinic	Monoclinic	Monoclinic	Monoclinic
Space group, Z	$P2_1/n$, 4	Pn, 4	$P2_1/n$, 4	$P2_1/n$, 4
a (Å)	4.068	10.517	7.7447	7.8661
b (Å)	14.469	3.9053	13.387	13.4536
c (Å)	17.030	26.075	10.8438	10.9374
α, deg	90	90	90	90
β, deg	94.047	93.255	95.757	95.314
γ, deg	90	90	90	90
Volume, $Å^3$	1000.1	1069.2	1118.6	1152.50
R factor	4.30	5.62	4.22	1.83
Temp, K	296	296	296	296
$d_{calculated}$ (mg/m^3)	1.430	1.551	1.747	1.966
No. of reflections collected	11663	14351	15748	14736
No. of unique reflections	1756	5020	1971	2030
$2\theta_{max}$, deg	25	28.072	24.997	24.997
No. of parameters	137	291	146	145
R1, wR2, (I > 2s(I))	0.0433,0.0920	0.0562,0.1023	0.0422,0.0742	0.0183,0.0456
R1, wR2 (all data)	0.0817,0.1097	0.1126,0.1199	0.0850,0.0892	0.0206,0.0474
Goodness of fit	1.041	0.983	1.046	1.080

CCDC number	2109608	2109609	2109612	2109614

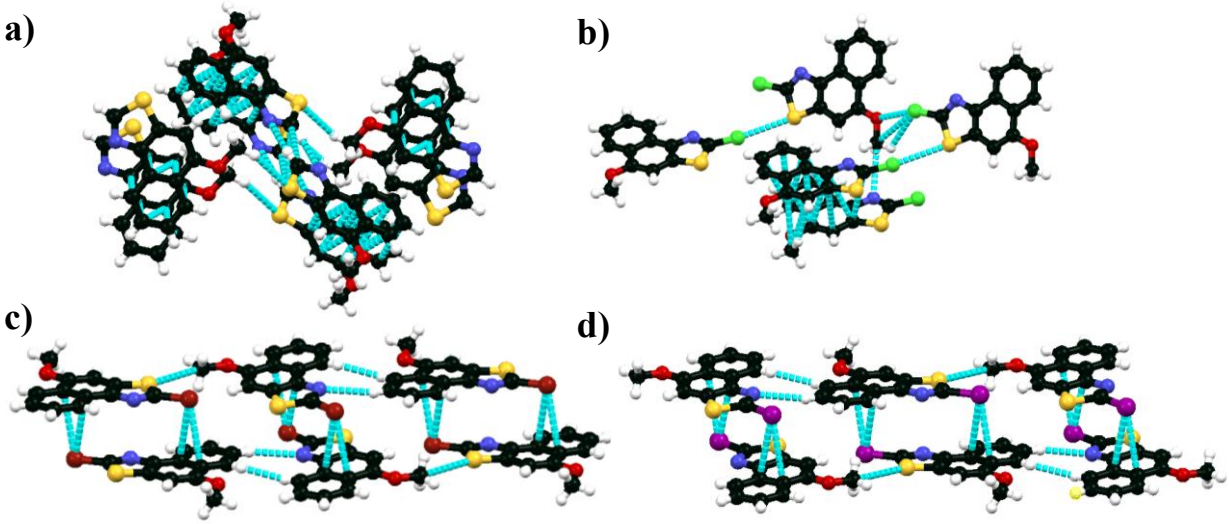

Figure 3.2: Interactions governing packing in a) NTH, b) NTC, c) NTB and d) NTI.

The essential condition governing isostructurality of materials is the similarity of the unit cells described by the cell similarity index (π),[31] comparing the lattice cell parameters of the crystals:

$$\pi = \left| \frac{a + b + c}{a' + b' + c'} - 1 \right|$$

where *a*, *b*, *c* and *a'*, *b'*, *c'* are orthogonalized lattice parameters of the two related crystals with $a + b + c > a' + b' + c'$. The similarity of two-unit cells can be endorsed when the value of π approaches zero. π-value relating NTI and NTB crystals was found to be 0.008, confirming isostructurality of the crystals. . Isostructurality can be further announced by a numerical descriptor,

Table 3.2. Relative % intermolecular interactions obtained from Hirshfeld analysis.

Interaction	C•••C	C•••H	S•••H	N•••H	X•••S	H•••H	ρ=[(%C•••H) /(%C•••C)]
NTH	11.7	14.5	13.3	7	0.0	42.2	1.2
NTC	11.1	11.7	12.2	6.2	2.6	28.7	1.0
NTB	7.7	10.5	10	5.1	0.1	27.4	1.3
NTI	7.6	10.7	10.1	5.2	0.2	25.8	1.4

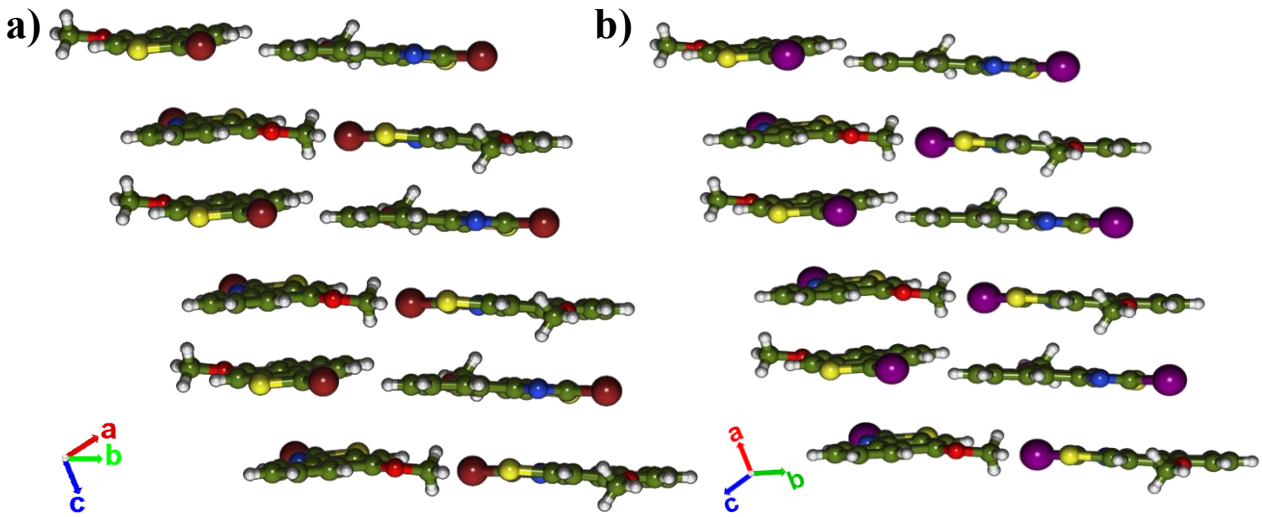

Figure 3.3: Isostructural packing arrangements in (a) NTI and (b) NTB.

isostructurality index (I_s),[31] calculated as follows:

$$I_s(n) = \left| \frac{[\sum (\Delta R_i)^2]^{1/2}}{n} - 1 \right| \times 100\%$$

where n represents the number of related non-hydrogen atoms and ΔR_i represents the distance differences between the atomic coordinates of two crystals. An I_s value approaching 100% correlates to high structural similarity between the selected crystal systems. The close relationship of NTI and NTB is demonstrated by an isostructurality index of 99.99%. The almost indistinguishable molecular overlay diagram (Figure 3.4) suggests the near-identity of NTB and NTI.

The aromatic ring interactions were quantitatively assessed using the aromatic analyzer component in Mercury 4.0.[32] A machine-learning algorithm is used to estimate the contribution of aromatic interactions to the stability of the crystal structure, by generating a model using DFT

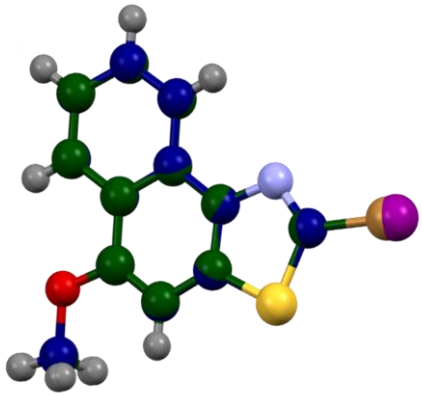

Figure 3.4: Molecular overlays of NTI (blue) and NTB (green).

energies and molecular descriptors including atom−atom and centroid−centroid distances. The model deals with the geometric description of aromatic interactions comprising the position of two phenyl rings relative to each other. The outcome of the model is a score that ranges from 0 to 10, classifying the strength of aromatic interactions as strong (7−10),[33] moderate (3−7), and weak (0−3). The implementation of the aromatic analyzer in NT derivatives revealed that the strength of aromatic interactions depends primarily on the degree of stacking between the aromatic rings. The molecular pairs with strong, moderate, and weak aromatic stabilization between neighboring stacks for NTH, NTC, NTB, and NTI are charted in Figures 3.5−3.8 and Tables 3.3-3.6, respectively. The result establishes the role of strong aromatic ring stabilization of the core in the isostructural crystal packing of NTI and NTB with approximately equal scores (7−10) for the neighboring stacks (Figures 3.7, 3.8 and Tables 3.5, 3.6).

In addition, we examined the supramolecular architectures in NTI and NTB crystals in terms of intermolecular interaction energies by utilizing an energy framework analysis in CrystalExplorer 17.5[34] using the CE-B3LYP/DGDZZP method.[35] The values of interaction energies determined between molecular pairs in each crystal form were used to construct the 3D topology of interactions termed as energy frameworks.[36] The total intermolecular interaction energies formulated from the crystal geometry consist of polarization, dispersion, electrostatic, and exchange-repulsion terms (Figure 3.9). Energies between molecular pairs are signified as cylinders

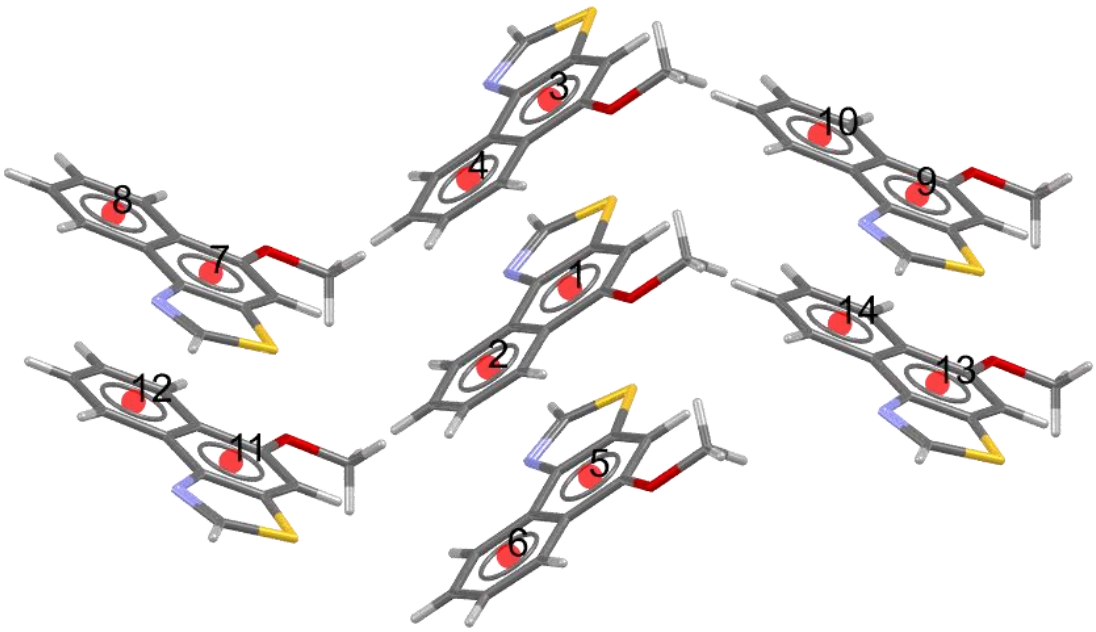

Figure 3.5: Role of aromatic ring stabilization NTH.

Table 3.3: List of strong and moderate aromatic interactions in NTH using aromatic analyzer component in Mercury 4.0.

Centroid 1	Centroid 2	Distance	Score	Profile
1	3	4.07	9.5	Strong
1	5	4.07	9.5	Strong
2	4	4.07	9.4	Strong
2	6	4.07	9.4	Strong
1	4	3.68	8.6	Strong
2	5	3.68	8.6	Strong
1	6	5.62	5.4	Moderate
2	3	5.62	5.4	Moderate
1	10	6.01	5.3	Moderate
1	14	5.91	5.3	Moderate
2	7	6.01	5.3	Moderate
2	11	5.91	5.3	Moderate

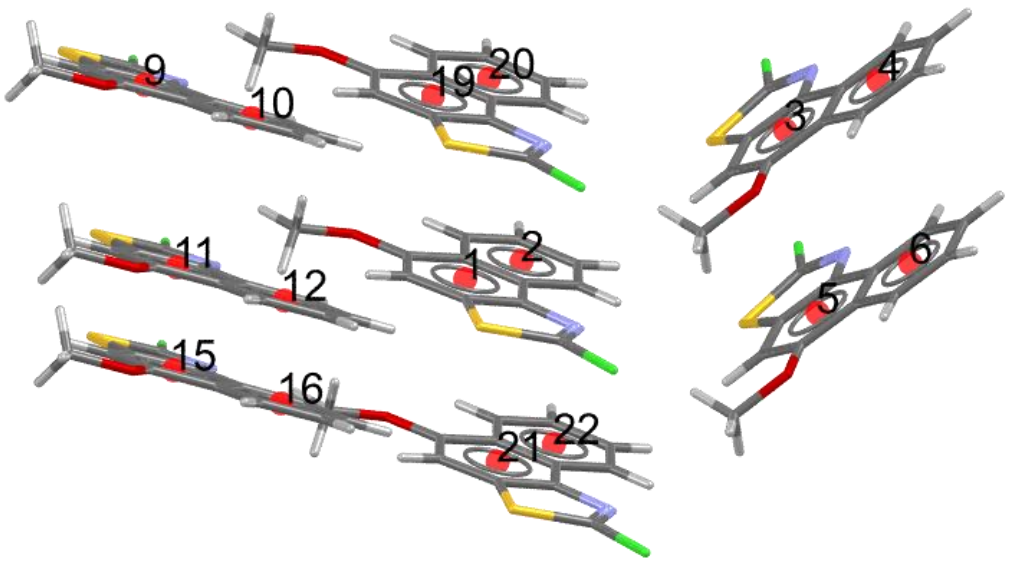

Figure 3.6: Role of aromatic ring stabilization NTC.

Table 3.4: List of strong and moderate aromatic interactions in NTC using aromatic analyzer component in Mercury 4.0.

Centroid 1	Centroid 2	Distance	Score	Profile
1	19	3.91	9.8	Strong
1	21	3.91	9.8	Strong
2	20	3.91	9.8	Strong
2	22	3.91	9.8	Strong
1	20	4.37	8.5	Strong
2	21	4.37	8.5	Strong
1	22	4.81	7.4	Strong
2	19	4.81	7.4	Strong
2	12	6.08	5.8	Moderate
2	3	6.14	5	Moderate
2	5	6.19	4.8	Moderate
1	16	6.53	4.3	Moderate
1	12	6.77	3.5	Moderate
2	10	6.87	3.2	Moderate

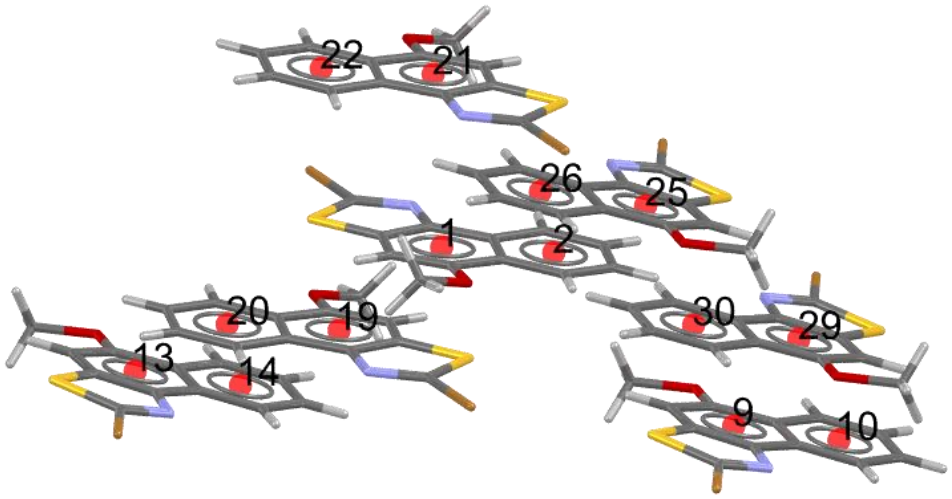

Figure 3.7: Role of aromatic ring stabilization NTB.

Table 3.5: List of strong and moderate aromatic interactions in NTB using aromatic analyzer component in Mercury 4.0.

Centroid 1	Centroid 2	Distance	Score	Profile
1	21	3.71	10	Strong
1	22	4.61	8.4	Strong
2	21	4.61	8.4	Strong
1	14	5.43	7.1	Strong
2	9	5.43	7.1	Strong
1	19	6.06	4.5	Moderate
2	22	6.38	3.9	Moderate
2	26	6.49	3.1	Moderate
2	30	6.49	3.1	Moderate

joining the centroids of pairs of molecules, with the width of cylinders being proportional to the magnitude of interaction energies. The strongest interactions in NTH and NTC are experienced between the parallel stacked dimers with stabilization energies of −37.7 and −43.8 kJ/mol, respectively (Figures 3.10-3.13), exhibiting favorable electrostatic and dispersion components (Figure 3.14). The analysis shows a remarkable similarity in the interaction modes, leading not only to the crystallographic isostructurality but also to isostructurality in terms of interaction

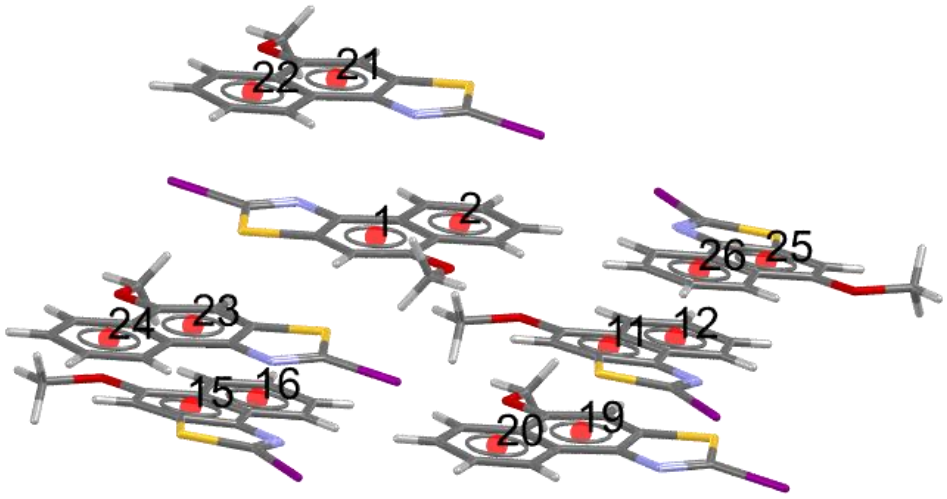

Figure 3.8: Role of aromatic ring stabilization NTI.

Table 3.6: List of strong and moderate aromatic interactions in NTI using aromatic analyzer component in Mercury 4.0.

Centroid 1	Centroid 2	Distance	Score	Profile
1	21	3.75	10	Strong
1	22	4.68	8	Strong
2	21	4.68	8	Strong
1	16	5.43	7.1	Strong
2	11	5.43	7.1	Strong
1	23	6.22	4	Moderate
2	22	6.46	3.6	Moderate
2	26	6.6	3.1	Moderate
2	20	6.49	3.1	Moderate

topologies, clearly evidenced in the electrostatic and dispersion components of NTB and NTI (Figure 3.9). A comparison of total energy frameworks indicated similar packing modes in isostructural NT crystals, where antiparallel stacked dimers of NTI and NTB displayed net higher magnitudes of interaction energy of −65.9 and −63.9 kJ/mol, respectively (Figures 3.15-3.18). Molecules possessing a high dipole moment (dipole moment >4 D) typically assemble in an antiparallel orientation to promote cancellation of molecular dipole moments.[37,38] NTI and NTB with net dipole moments of 3.42 and 3.65 D adopt an antiparallel arrangement (Figure 3.3a,b and Table 3.7) in comparison to the unsubstituted NTH (2.73 D), through π−π stacking achieving the design goal of dipole minimization. Even though NTC possesses the highest net dipole moment of 3.69 D among the NT derivatives, NTC is not oriented in an antiparallel mode The distinct packing in NTC in comparison to isostructural NTB and NTI can be due to the presence of Cl•••S interactions confirmed from QTAIM (Table 3.8) and Penda's interacting quantum atoms (IQA)[39] analysis (Figure 3.19 and Table 3.9).

To quantitatively comprehend the optical band gaps (E_g) of NT derivatives, UV−vis reflectance spectra of the crystals were transformed into Tauc plots by using Kubelka−Munk[40] functions.[41,42] The optical band gap of the parent crystal (NTH) is 3.48 eV, while the band gaps of

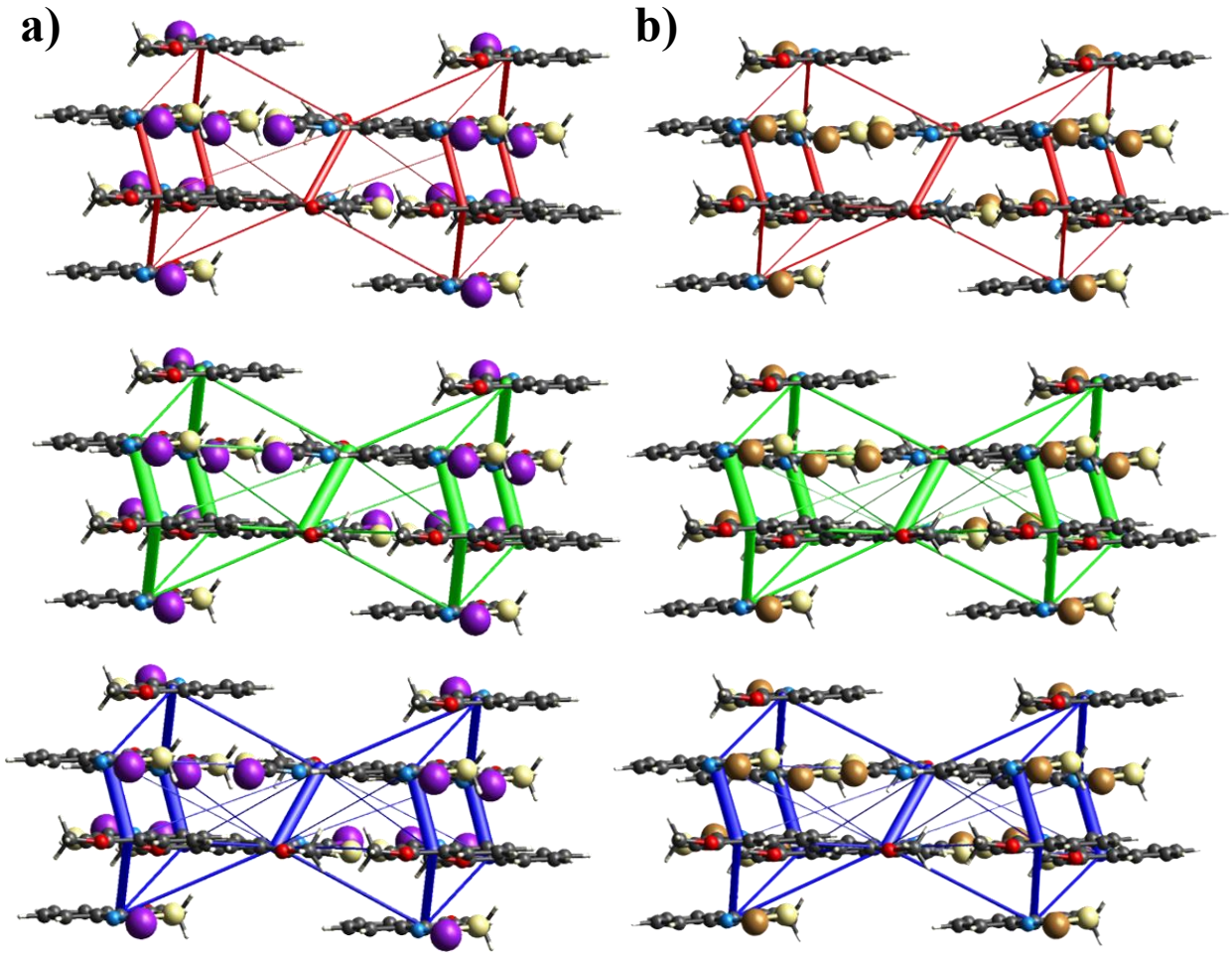

Figure 3.9: Energy framework for separate electrostatic (red), dispersion (green) and total energies (blue) for (a) NTI and (b) NTB. The energy scale factor is 50.

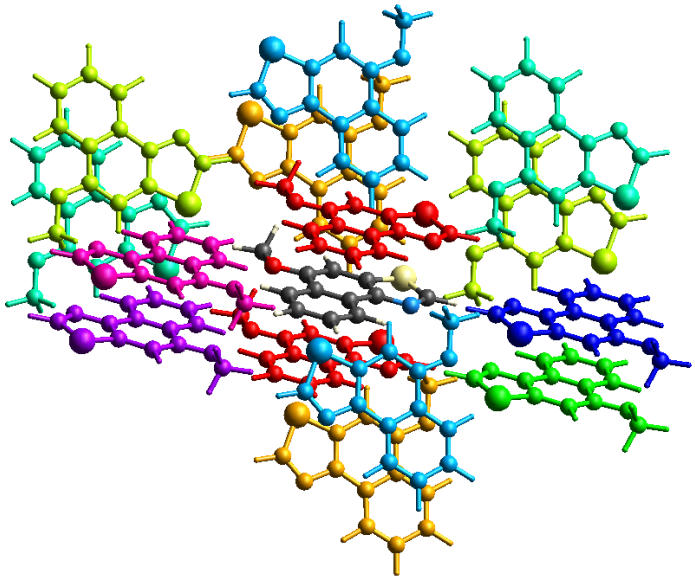

Figure 3.10: Selected molecular pairs to calculate interaction energies of NTH.

	N	Symop	R	Electron Density	E_ele	E_pol	E_dis	E_rep	E_tot
	1	x, y, z	4.07	B3LYP/DGDZVP	-14.6	-3.6	-57.9	49.8	-37.7
	0	-x+1/2, y+1/2, -z+1/2	7.35	B3LYP/DGDZVP	-9.0	-1.9	-18.3	14.8	-17.8
	1	x+1/2, -y+1/2, z+1/2	9.86	B3LYP/DGDZVP	-1.4	-0.4	-6.2	7.0	-2.9
	0	-x, -y, -z	9.40	B3LYP/DGDZVP	-5.1	-0.5	-6.5	4.9	-8.4
	1	x+1/2, -y+1/2, z+1/2	10.10	B3LYP/DGDZVP	-1.0	-0.5	-6.2	6.4	-2.9
	2	-x+1/2, y+1/2, -z+1/2	7.76	B3LYP/DGDZVP	-4.4	-0.7	-13.7	11.4	-10.0
	1	-x, -y, -z	9.10	B3LYP/DGDZVP	-18.0	-2.7	-11.8	17.9	-20.3
	0	-x, -y, -z	8.68	B3LYP/DGDZVP	-5.3	-0.6	-16.1	11.4	-13.0
	1	-x, -y, -z	9.66	B3LYP/DGDZVP	-2.3	-0.2	-8.2	4.2	-7.1

Figure 3.11: Intermolecular interaction energies of molecular pairs (NTH).

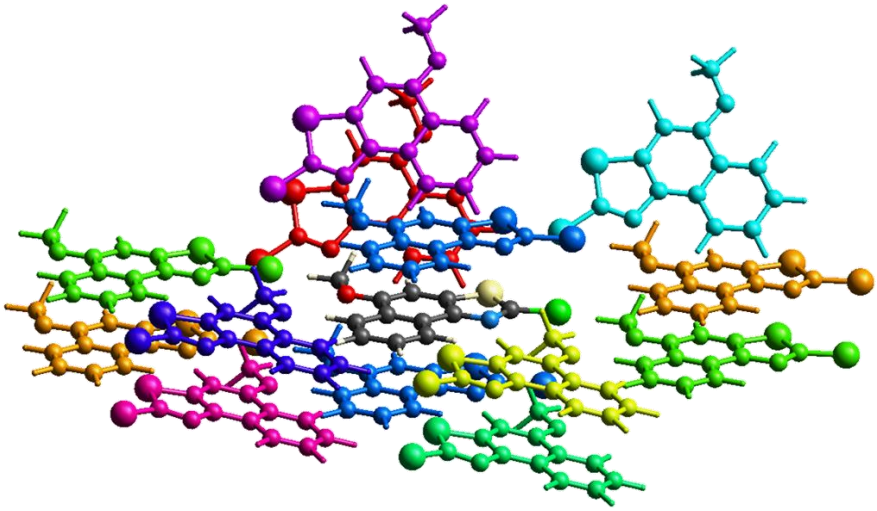

Figure 3.12: Selected molecular pairs to calculate interaction energies of NTC.

	N	Symop	R	Electron Density	E_ele	E_pol	E_dis	E_rep	E_tot
	1	-	7.46	B3LYP/DGDZVP	-11.6	-2.5	-22.2	18.8	-21.8
	2	x, y, z	11.22	B3LYP/DGDZVP	-1.5	-0.2	-4.4	3.3	-3.5
	1	-	8.22	B3LYP/DGDZVP	-7.9	-1.9	-13.8	11.4	-14.7
	2	x, y, z	10.52	B3LYP/DGDZVP	-6.6	-0.3	-9.9	14.3	-6.9
	1	-	7.16	B3LYP/DGDZVP	-10.7	-1.5	-18.4	18.4	-17.0
	1	-	10.08	B3LYP/DGDZVP	-2.0	-0.1	-6.4	10.1	-1.5
	2	x, y, z	3.91	B3LYP/DGDZVP	-20.2	-3.2	-68.7	64.1	-43.8
	1	-	10.75	B3LYP/DGDZVP	-2.5	-0.5	-11.8	7.8	-8.5
	1	-	7.40	B3LYP/DGDZVP	-8.7	-1.6	-16.2	13.7	-16.1
	1	-	9.97	B3LYP/DGDZVP	-2.8	-0.5	-11.5	5.5	-9.9

Figure 3.13: Intermolecular interaction energies of molecular pairs (NTC).

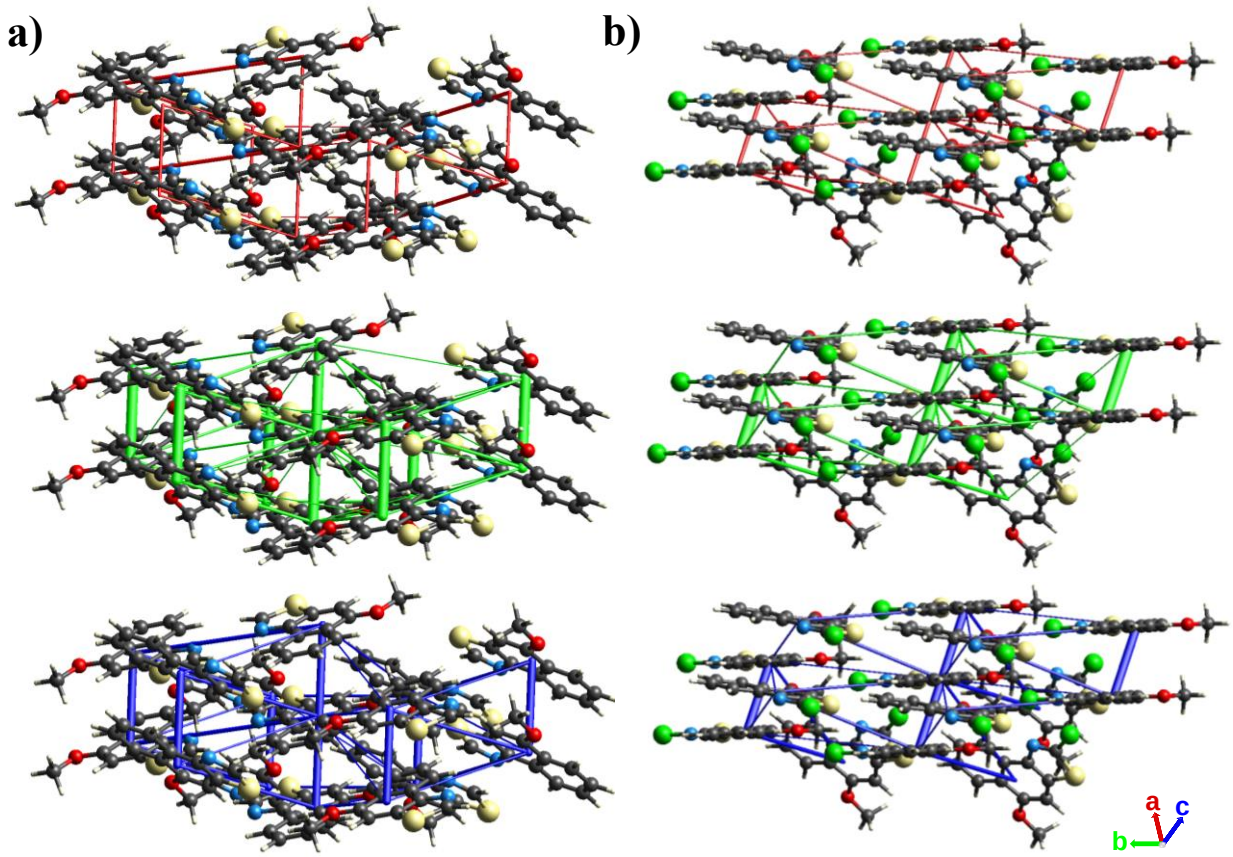

Figure 3.14: Energy framework for separate electrostatic (red), dispersion (green) and total energy (blue) for a) NT and b) NTC.

the halogenated derivatives systematically decreased to 3.33 eV for NTC, 3.23 eV for NTB, and 3.07 eV for NTI (Figure 3.20). The electronegativity decreases with an increase in the size of the halogens, influencing the energy levels and absorption spectra of conjugated materials. Functionalizing the conjugated molecule with halogens lowers the LUMO level with respect to the parent molecule, ascribed to the inductive effect of halogens. The increase in the size of the halogen

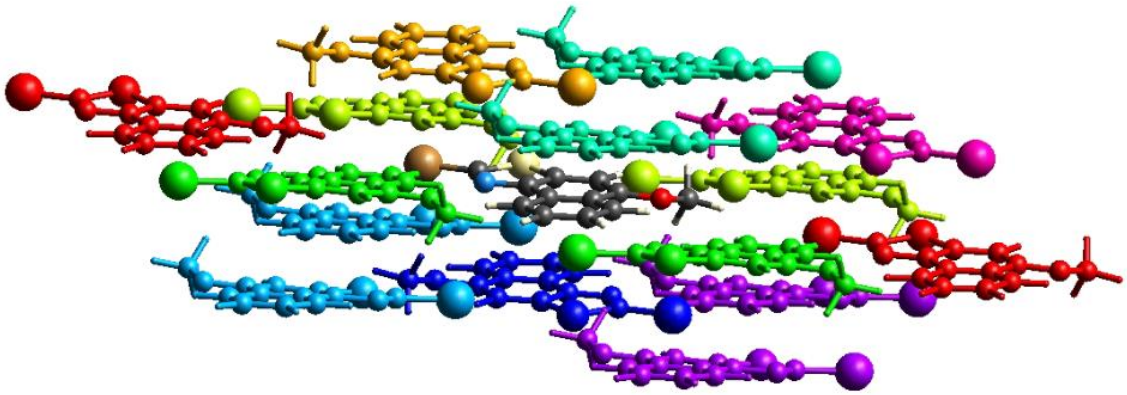

Figure 3.15: Selected molecular pairs to calculate interaction energies of NTB.

	N	Symop	R	Electron Density	E_ele	E_pol	E_dis	E_rep	E_tot
	2	x, y, z	12.68	B3LYP/DGDZVP	0.2	-0.2	-2.8	1.4	-1.5
	1	-x, -y, -z	4.07	B3LYP/DGDZVP	-18.9	-1.7	-52.7	48.5	-37.2
	2	x+1/2, -y+1/2, z+1/2	9.09	B3LYP/DGDZVP	-3.4	-0.8	-11.4	10.7	-7.5
	2	x+1/2, -y+1/2, z+1/2	9.35	B3LYP/DGDZVP	-6.8	-1.5	-16.9	15.7	-13.4
	2	-x+1/2, y+1/2, -z+1/2	8.51	B3LYP/DGDZVP	-10.2	-1.2	-17.6	15.1	-17.6
	2	-x+1/2, y+1/2, -z+1/2	8.73	B3LYP/DGDZVP	-3.5	-0.2	-7.5	6.9	-6.1
	1	-x, -y, -z	3.69	B3LYP/DGDZVP	-37.3	-3.4	-82.4	80.6	-63.9
	2	-x+1/2, y+1/2, -z+1/2	11.00	B3LYP/DGDZVP	-3.0	-0.5	-5.9	3.2	-6.7
	1	-x, -y, -z	10.91	B3LYP/DGDZVP	-6.6	-1.2	-15.7	8.8	-16.1

Figure 3.16: Intermolecular interaction energies of molecular pairs (NTB).

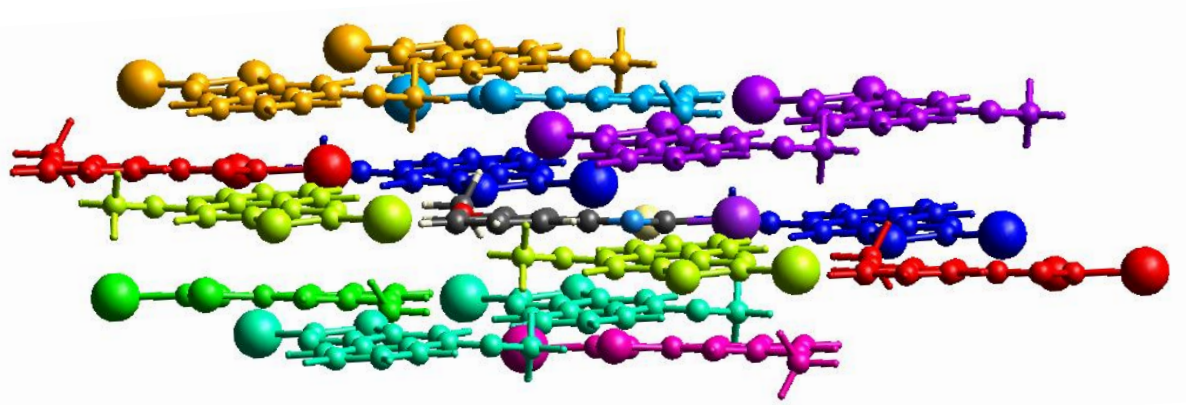

Figure 3.17: Selected molecular pairs to calculate interaction energies of NTI.

	N	Symop	R	Electron Density	E_ele	E_pol	E_dis	E_rep	E_tot
	2	x, y, z	12.87	B3LYP/DGDZVP	0.9	-0.4	-4.1	2.9	-1.1
	2	-x+1/2, y+1/2, -z+1/2	11.90	B3LYP/DGDZVP	-3.0	-0.5	-5.5	2.7	-6.6
	2	x+1/2, -y+1/2, z+1/2	9.66	B3LYP/DGDZVP	-7.1	-1.5	-17.7	16.2	-14.0
	1	-x, -y, -z	12.08	B3LYP/DGDZVP	-6.0	-1.1	-15.2	7.7	-15.7
	2	-x+1/2, y+1/2, -z+1/2	9.15	B3LYP/DGDZVP	-10.1	-1.3	-17.6	14.9	-17.7
	1	-x, -y, -z	4.29	B3LYP/DGDZVP	-38.8	-3.3	-85.9	84.9	-65.9
	2	x+1/2, -y+1/2, z+1/2	8.97	B3LYP/DGDZVP	-4.7	-0.9	-13.3	13.0	-9.2
	2	-x+1/2, y+1/2, -z+1/2	8.24	B3LYP/DGDZVP	-5.4	-0.3	-10.1	12.5	-6.9
	1	-x, -y, -z	3.78	B3LYP/DGDZVP	-26.8	-1.9	-60.4	64.9	-42.2

Figure 3.18: Intermolecular interaction energies of molecular pairs (NTI).

Table 3.7: Magnitudes of dipole moments (Debye) for monomer and antiparallel stacked dimers in the crystal packing of NTs.

NT derivatives	Monomer	Anti-parallel dimer
NTH	2.72	-
NTC	3.69	-
NTB	3.65	0.00
NTI	3.41	0.00

Table 3.8: Calculated topological properties of electron density function for the intermolecular interactions in crystalline NTC.

		Interactions	d, Å	$\rho(r)$, eÅ^{-3}	$\nabla^2\rho(r)$, eÅ^{-5}
NTC trimer showing Cl•••S, Cl••• Cl and Cl•••O interactions.	Bond critical points (BCPs)	Cl21•••S48	3.553	0.005478	0.020702
		Cl21•••Cl45	3.770	0.004427	0.014898
		O71•••Cl45	3.136	0.007468	0.031625

atom allows the delocalization of the π-electron cloud due to the availability of empty d orbitals.[10,43] The reduction in energy values from NTB to NTI clearly reflects the influence of single-atom substitution in band-gap modulation. In order to theoretically visualize the contribution of halogen atoms to the conduction and valence bands in NTs, density functional theory calculations within the local density approximation were performed using the Quantum Espresso package. Theoretical

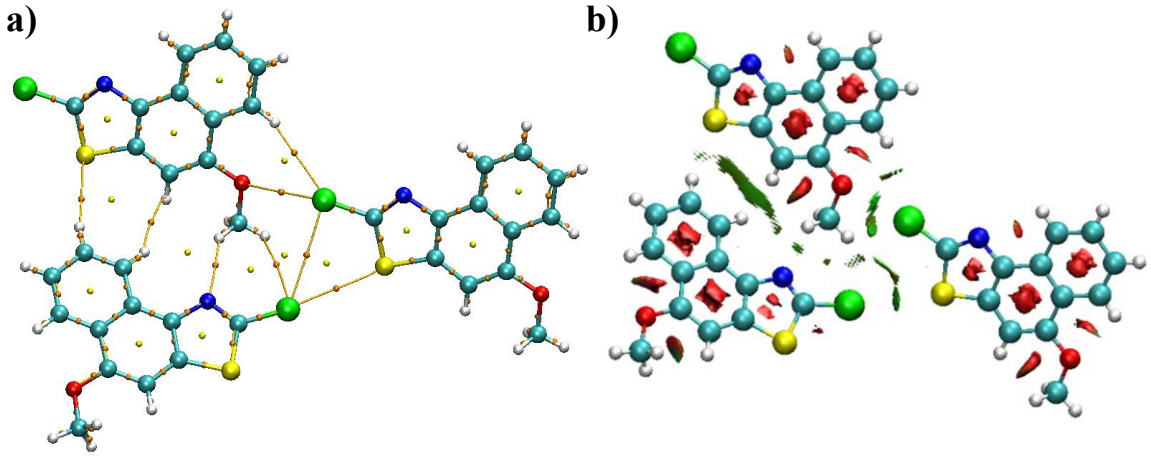

Figure 3.19: QTAIM electron density map and NCI plot showing weak stabilizing interactions in NTC.

Table 3.9: IQA interaction energies. Total noncovalent interaction energies and its components of NTC are shown. Energies are given in kcal/mol.

	Interactions	E_t	E_{xc}	E_{cl}
NTC trimer	Cl21•••S48	-8.26	-4.96	-3.30
	Cl21•••Cl45	-0.41	3.08	-3.49
	O71•••Cl45	10.53	15.63	-5.09

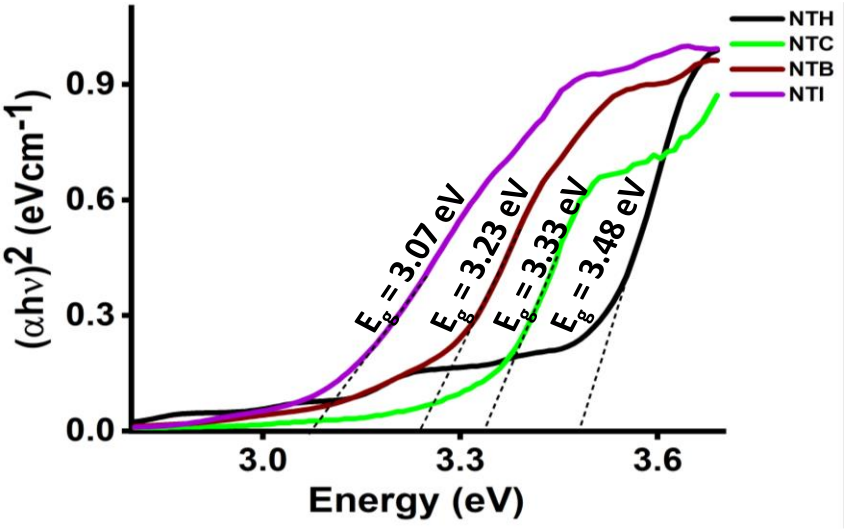

Figure 3.20: Tauc plot showing a reduction in the optical band gap of NTs from 3.48 to 3.07 eV.

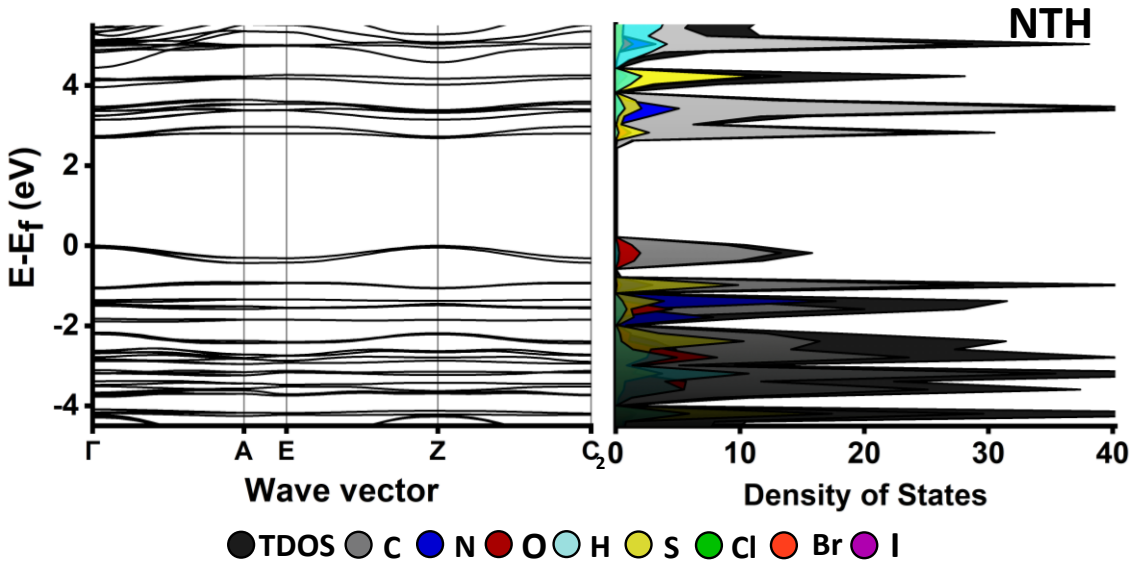

Figure 3.21: Electronic band structure and projected density of states (states/eV) of NTH.

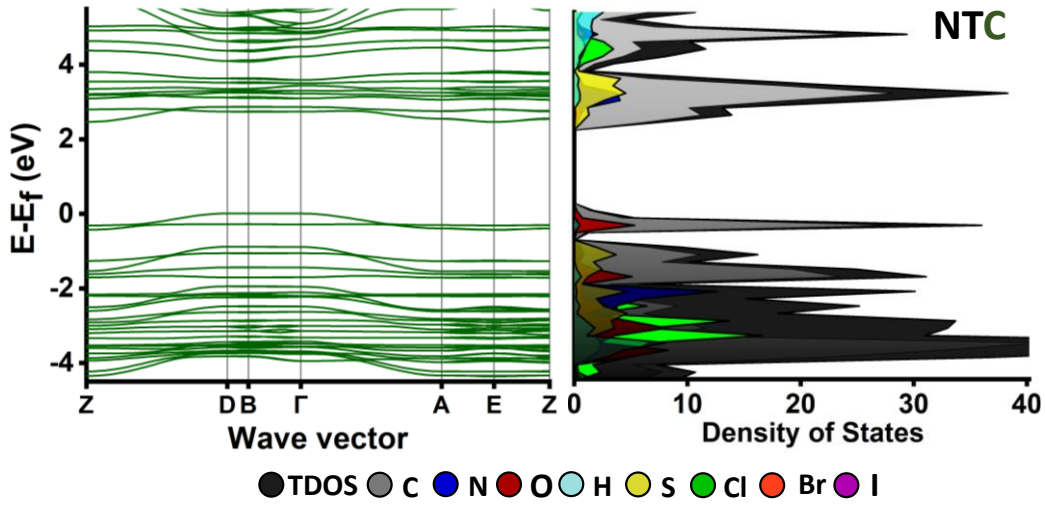

Figure 3.22: Electronic band structure and projected density of states (states/eV) of NTC.

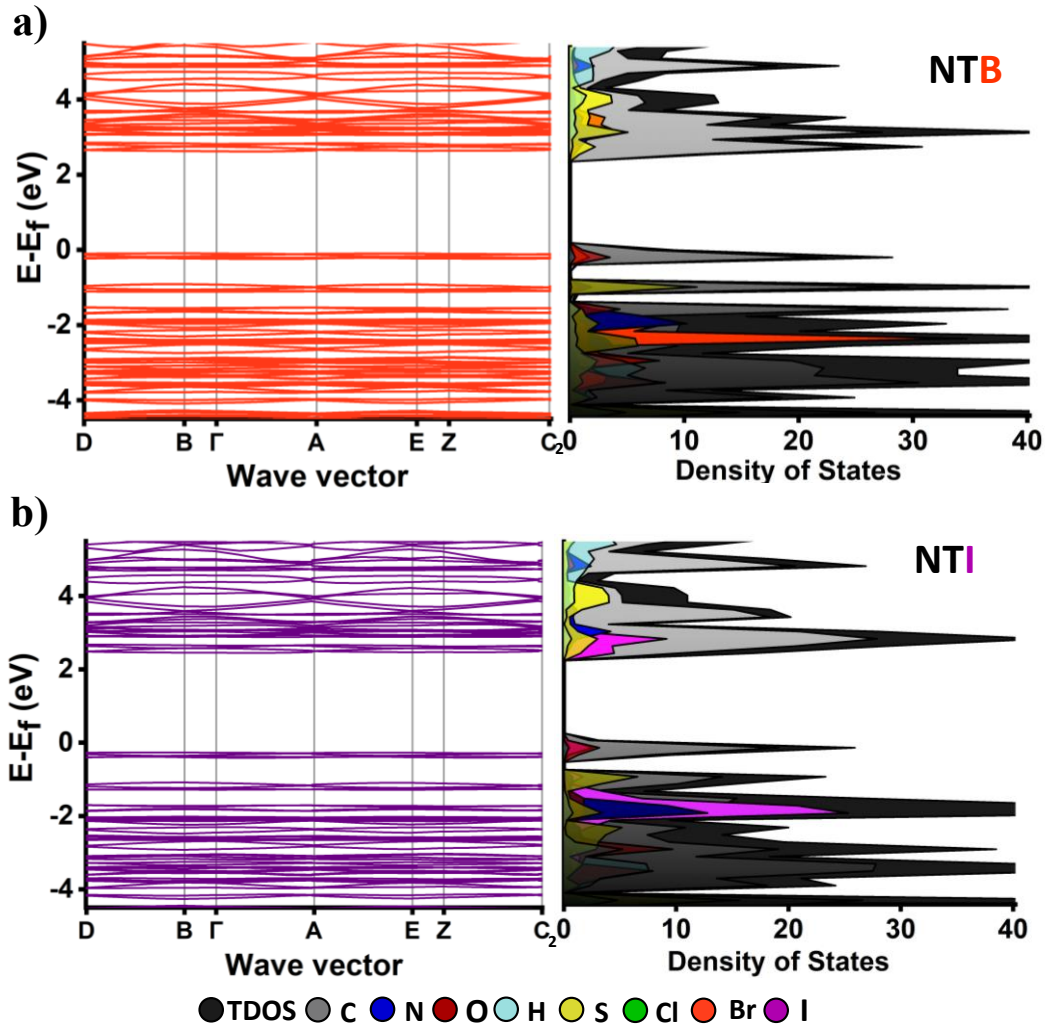

Figure 3.23: Electronic band structure and projected density of states (states/eV) of a) NTB and b) NTI.

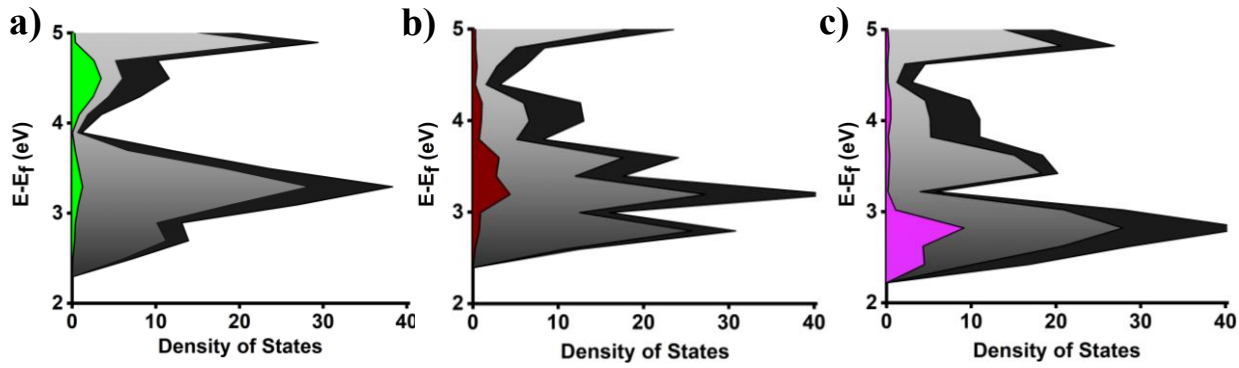

Figure 3.24: Close view of conduction bands from projected density of states (states/eV) of (a) NTC, (b) NTB and (c) NTI.

band gaps obtained for NTH, NTC, NTB, and NTI of 2.7, 2.5, 2.4, and 2.3 eV, respectively, reflected a trend similar to that obtained from experimental values. The deviation between experimental and calculated band gaps is due to the limitation of DFT methods.[44] The band gap of NTH is tweaked by singleatom substitution and decreases as the atomic number of the halogen substituents increases. Isostructurality in NTB and NTI crystals is manifested as very similar band structure characteristics (Figure 3.23) with unique band gaps. Projected density of state (PDOS) calculations were executed to determine the character of frontier orbitals in NTs. The inspection of PDOS into the elemental contribution unveiled that the major contribution arises from carbon atoms in NTs. The halogen atoms Cl, Br, and I in NTC, NTB, and NTI have a higher DOS near the valence band edges (Figures 3.22 and 3.23). A gradual shift of the halogen contribution (I > Br > Cl) toward the conduction band edge and increment in DOS confirmed the effect of halogen atoms in the reduction of the band gap (Figure 3.24). The trend in band gap observed in NTs reinforces the idea that halogen substitution leads to lowering of the band gap with increase in the atomic number of substituted halogens in organic semiconductors.[10,12]

3.3. Conclusions

In summary, the effect of halogen substitution in naphthothiazole portrayed the efficient tuning of the optical band gap for constructing optoelectronic materials following the trend NTH > NTC > NTB > NTI. Even with their isostructural packing, the bromine- and iodine-substituted derivatives exhibit a reduction in band gap with an increase in the atomic number. A structural similarity analysis quantitatively supported the existence of isostructurality between Br- and I-

substituted molecular crystals. Pairwise intermolecular interactions derived from energy framework analyses revealed the comparable contribution of electrostatic and dispersion components to the total interaction energy in the isostructural crystals. Isostructurality circumvents the atomic size and the functional group variation to regulate the molecular architecture in NTB and NTI. The projected density of states explains the substantial contribution of halogen atoms to the energy levels in band edges. The effective role of halogen atoms as chemical tailoring scissors in band engineering emerges as a rational design for organic semiconductors at the molecular and supramolecular level.

3.4. Experimental Section

3.4.1. Synthesis of 4-methoxynaphthalen-1-amine (2)

1-methoxy-4-nitronapthalene (2.46 mmol) was dissolved in methanol and catalytic amount of Pd/C was added to the round bottom flask. The reaction mixture was purged with hydrogen and was stirred for 8 hours at room temperature. The reaction mixture was then extracted with dichloromethane. The crude mixture was used for the next reaction without further purification.

3.4.2. Synthesis of 5-methoxynaphtho[1,2-*d*]thiazol-2-amine (3)

Dissolved 4-methoxynaphthalen-1-amine (crude, 0.23 mmol) and potassium thiocyanate (0.46 mmol) in a round bottom flask charged with glacial acetic acid and stirred for 5 minutes. Then slowly added Br_2 (catalytic amount) and the reaction was stirred for 6 hours at room temperature. After confirming the full consumption of reactant, added 10ml of saturated sodium thiosulphate solution to quench the excess bromine in the reaction mixture. The organic compound was extracted using dichloromethane and was purified using silica gel column chromatography (petroleum ether: ethyl acetate = 3:1) to obtain compound 3 in 34 % yield.

M.p. = 225°C

^{1}H NMR (500 MHz, $CDCl_3$, ppm) δ = 8.35 (d, J = 8 Hz, 1H), 8.19 (d, J = 8.5 Hz, 1H), 7.50 (t, J = 8 Hz, 1H), 7.74 (t, J = 8 Hz, 1H), 6.96 (s, 1H), 5.13 (s, 2H), 3.94 (s, 3H).

^{13}C NMR (500 MHz, $CDCl_3$, ppm) δ = 166.3, 143.84, 134.69, 133.10, 128.14, 126.06, 124.94, 123.57, 122.60, 95.63, 55.95

HRMS (APCI) m/z calculated for $C_{12}H_{10}N_2OS$ $[(M+H)^+]$; 231.0514; found 231.0586.

3.4.3. Synthesis of 5-methoxynaphtho[1,2-*d*]thiazole (4a)

To a freshly prepared saturated solution of tertiary-butyl nitrite (1.3 mmol) in tetrahydrofuran, 5-methoxynaphtho[1,2-*d*]thiazol-2-amine dissolved in tetrahydrofuran was added dropwise using an addition funnel over one hour. The reaction mixture was heated at reflux for additional 3 hours before cooling it down to room temperature. After confirming the complete consumption of reactant, the reaction mixture was diluted with ethyl ether and washed three times with sodium thiosulphate in brine. The mixture was further separated and purified employing silica gel column

chromatography using a mixture of petroleum ether and ethyl acetate (99:1) and white solid material was obtained with a yield of 38%.

M.p. = 87°C

^{1}H NMR (500MHz, $CDCl_3$, 300 K), δ = 9.024 (s, 1H), 8.81 (d, J = 8 Hz, 1H), 8.28 (d, J = 8 Hz, 1H), 7.68 (t, J = 15 Hz, 1H), 7.56 (t, J = 15 Hz, 1H), 7.17 (d, J = 12.5 Hz, 1H), 4.01 (s, 3H).

^{13}C NMR (500 MHz, $CDCl_3$, 300 K): δ = 154.98, 150.15, 131.24, 128.27, 126.41, 125.26, 124.19, 123.68, 122.78, 96.13, 56.00.

HRMS (APCI) m/z calculated for $C_{12}H_9NOS$ [$(M+H)^+$]: 216.0405; found, 216.0474.

3.4.4. Synthesis of 2-chloro-5-methoxynaphtho[1,2-*d*]thiazole (4b)

To a round bottom flask charged with a mixture of tertiary butyl nitrite (0.97 mmol), copper (II) chloride (0.78 mmol), and acetonitrile, 5-methoxynaphtho[1,2-*d*]thiazol-2-amine (0.65 mmol) was added as fractions while stirring. After complete addition, the reaction mixture was further stirred for 2 hours and stirred 1 more hour at 65°C. After confirming the complete consumption of reactant using thin layer chromatography, the crude mixture was filtered out. The filtrate was then poured into 6N HCl and extracted using diethyl ether. The compound 4b was separated and purified from the crude residue using silica gel column chromatography (petroleum ether: ethyl acetate = 99:1) with a yield of 46 %.

M.p. = 130°C.

^{1}H NMR (400 MHz, $CDCl_3$) δ = 8.55 (d, J = 8 Hz, 1H), 8.23 (d, J = 8 Hz, 1H), 7.60 (m, J = 16 Hz, 1H), 7.51 (m, J = 16 Hz, 1H), 7.00 (s, 1H), 3.975 (s, 3H).

^{13}C NMR (500 MHz, $CDCl_3$) δ = 153.43, 147.30, 140.84, 132.27, 127.29, 124.97, 123.98, 122.45, 121.58, 94.73, 54.89.

HRMS (APCI) m/z calculated for $C_{12}H_8ClNOS$ [$(M+H)^+$]: 250.7120; found, 250.0085.

3.4.4. Synthesis of 2-bromo-5-methoxynaphtho[1,2-*d*]thiazole (4c)

To a solution of 5-methoxynaphtho[1,2-*d*]thiazol-2-amine (1.3 mmol) in acetonitrile, p-Toluenesulfonic acid (1.7 mmol), CuBr2 (0.02 mmol), Tetra-n-butylammonium bromide (2.6 mmol) was added and stirred at room temperature for 4 hours. On completion of reaction, the

reaction mixture was quenched by adding 15 ml of water, washed with Sodium bicarbonate extracted with ethyl acetate. The compound 4c was obtained as a white solid after purification by means of silica gel column chromatography, ethyl acetate: petroleum ether (1:99) with a yield of 50 %.

M.p. = 143°C.

^{1}H NMR (400 MHz, $CDCl_3$) δ = 8.59 (d, J = 8.5 Hz, 1H), 8.24 (d, J = 8.5 Hz, 1H), 7.61 (t, J = 14.5 Hz, 1H), 7.51 (t, J = 15.5 Hz, 1H), 7.03 (s, 1H), 3.981 (s, 3H).

^{13}C NMR (500 MHz, $CDCl_3$) δ = 154.47, 143.39, 134.74, 133.10, 128.14, 126.06, 124.94, 123.57, 122.60, 95.63, 55.95.

HRMS (APCI) m/z calculated for $C_{12}H_8BrNOS$ $[(M+H)^+]$: 295.9490; found, 295.9554.

3.4.4. Synthesis of 2-iodo-5-methoxynaphtho[1,2-*d*]thiazole (4d)

To a solution of 5-methoxynaphtho[1,2-*d*]thiazol-2-amine (0.5 mmol) in acetonitrile, p-Toluenesulfonic acid (1.3 mmol) was added and stirred at 0 °C for 10 minutes. After complete dissolution, a saturated aqueous solution of the mixture of sodium nitrate (0.86 mmol) and potassium iodide (1.08) was added dropwise over a period of 15 minutes and reaction mixture was kept stirring for 5 hours. On completion of reaction, the reaction mixture was quenched by adding distilled water, further washed with Sodium bicarbonate until the pH reached about 9, followed by the addition of saturated aqueous solution of sodium thiosulphate. The precipitate obtained was filtered, dried, and extracted with dichloromethane. The compound 4d was obtained as a white solid after purification by means of silica gel column chromatography, ethyl acetate: petroleum ether (1:49) with a yield of 42 %.

M.p. = 130°C.

^{1}H NMR (400 MHz, $CDCl_3$) : δ = 8.63 (d, J = 8 Hz, 1H), 8.23 (d, J = 8.5 Hz, 1H), 7.60 (m, J = 15 Hz, 1H), 7.51 (m, J = 16 Hz, 1H), 7.06 (s, 1H), 3.97 (s, 3H).

^{13}C NMR (500 MHz, $CDCl_3$) δ = 154.43, 145.74, 136.89, 127.95, 126.04, 124.76, 123.55, 122.55, 97.94, 95.36, 55.92.

HRMS (APCI) m/z calculated for $C_{12}H_8INOS$ $[(M+H)^+]$: 341.9371; found, 341.9435.

3.5. Appendix

3.5.1: Materials and Methods

Same as discussed in section 2.6.1 (Chapter 2)

3.5.2: Energy Framework

The intermolecular interaction energies in NT derivatives was estimated by the CE-B3LYP method using the DGDZVP basis set in CrystalExplorer package.[36,45] The components of interaction energies are scaled using the optimized scale factors for the CEB3LYP method given by $K_{electrostatic}$ = 1.057, $K_{polarization}$ = 0.740, $K_{dispersion}$ = 0.871, and $K_{repulsion}$ = 0.618. Further, the intermolecular interaction topologies were visualized using the energy frameworks tool in CrystalExplorer. The intermolecular interaction energies of molecular pairs and interaction topologies represent molecular clusters around a central molecule in the crystal structures that make direct interactions. They are color-coded according to the colors given to their respective rows of the interaction energy table.

3.5.3: Band Structure and Density of States (DOS)

The calculations were based on density functional theory (DFT) as implemented in the Quantum Espresso (QE)[31] package within the local density approximation (LDA).[46,47] Total energy and electronic structure calculations have been performed using the plane-wave self-consistent field package, a component of the Quantum Espresso distribution. Projector augmented wave (PAW) type pseudopotentials were used. van der Waals (vdW) interactions were corrected using the DFT-D method.[48,49] The kinetic energy cutoff for the wave function was set to 50 Ry, which was obtained after a convergence test. k meshes of 6 × 6 × 6 for NTH and 8 × 8 × 8 for NTC, NTB, and NTI were adopted to sample the first Brillouin zone. The convergence threshold for selfconsistent calculations was set to 10−8 . After a self-consistent calculation, a non-self-consistent calculation was performed under the same conditions and with a k mesh of 10 × 10 × 10. To analyze the data, QE components such as dos, projwfc, and bands were used to compute the total density of states (TDOS), the partial density of states (PDOS), and the band structure. The high-symmetry k points of the Brillouin zone for the band structure were calculated using SeeK-path: a k-path finder and visualizer.[50,51]

3.6 REFERENCES

(1) Ortstein, K.; Hutsch, S.; Hambsch, M.; Tvingstedt, K.; Wegner, B.; Benduhn, J.; Kublitski, J.; Schwarze, M.; Schellhammer, S.; Talnack, F.; Vogt, A.; Bäuerle, P.; Koch, N.; Mannsfeld, S. C. B.; Kleemann, H.; Ortmann, F.; Leo, K. Band Gap Engineering in Blended Organic Semiconductor Films Based on Dielectric Interactions. *Nature Materials* **2021**, *20*, 1407–1413.

(2) Schwarze, M.; Tress, W.; Beyer, B.; Gao, F.; Scholz, R.; Poelking, C.; Ortstein, K.; Günther, A. A.; Kasemann, D.; Andrienko, D.; Leo, K. Band Structure Engineering in Organic Semiconductors. *Science* **2016**, *352*, 1446–1449.

(3) Woods-Robinson, R.; Han, Y.; Zhang, H.; Ablekim, T.; Khan, I.; Persson, K. A.; Zakutayev, A. Wide Band Gap Chalcogenide Semiconductors. *Chemical Reviews* **2020**, *120*, 4007–4055.

(4) Sariciftci, N. S.; Smilowitz, L.; Heeger, A. J.; Wudl, F. Photoinduced Electron Transfer from a Conducting Polymer to Buckminsterfullerene. *Science* **1992**, *258*, 1474–1476.

(5) Sirringhaus, H.; Brown, P. J.; Friend, R. H.; Nielsen, M. M.; Bechgaard, K.; Langeveld-Voss, B. M. W.; Spiering, A. J. H.; Janssen, R. A. J.; Meijer, E. W.; Herwig, P.; de Leeuw, D. M. Two-Dimensional Charge Transport in Self-Organized, High-Mobility Conjugated Polymers. *Nature* **1999**, *401*, 685–688.

(6) Burroughes, J. H.; Bradley, D. D. C.; Brown, A. R.; Marks, R. N.; Mackay, K.; Friend, R. H.; Burns, P. L.; Holmes, A. B. Light-Emitting Diodes Based on Conjugated Polymers. *Nature* **1990**, *347*, 539–541.

(7) Kotadiya, N. B.; Lu, H.; Mondal, A.; Ie, Y.; Andrienko, D.; Blom, P. W. M.; Wetzelaer, G. J. A. H. Universal Strategy for Ohmic Hole Injection into Organic Semiconductors with High Ionization Energies. *Nature Materials* **2018**, *17*, 329–334.

(8) Chen, Y.; Wan, X.; Long, G. High Performance Photovoltaic Applications Using Solution-Processed Small Molecules. *Accounts of Chemical Research* **2013**, *46*, 2645–2655.

(9) Salzmann, I.; Heimel, G.; Oehzelt, M.; Winkler, S.; Koch, N. Molecular Electrical Doping of Organic Semiconductors: Fundamental Mechanisms and Emerging Dopant Design Rules. *Accounts of Chemical Research* **2016**, *49*, 370–378.

(10) Tang, M. L.; Bao, Z. Halogenated Materials as Organic Semiconductors. *Chemistry of Materials* **2011**, *23*, 446–455.

(11) Clayden. *Organic Chemistry.*; Oxford University Press, 2001.

(12) Zbořil, R.; Karlický, F.; Bourlinos, A. B.; Steriotis, T. A.; Stubos, A. K.; Georgakilas, V.; Šafářová, K.; Jančík, D.; Trapalis, C.; Otyepka, M. Graphene Fluoride: A Stable Stoichiometric Graphene Derivative and Its Chemical Conversion to Graphene. *Small* **2010**, *6*, 2885–2891.

(13) Ramakrishnan, R.; Niyas, M. A.; Lijina, M. P.; Hariharan, M. Distinct Crystalline Aromatic Structural Motifs: Identification, Classification, and Implications. *Accounts of Chemical Research* **2019**, *52*, 3075–3086.

(14) García-Arriaga, M.; Hobley, G.; Rivera, J. M. Isostructural Self-Assembly of 2′-Deoxyguanosine Derivatives in Aqueous and Organic Media. *Journal of the American Chemical Society* **2008**, *130*, 10492–10493.

(15) Kitaigorodsky, A. I. *Molecular Crystals and Molecules*; 1974; Vol. 9.

(16) Dey, A.; Desiraju, G. R. Supramolecular Equivalence of Ethynyl, Chloro, Bromo and Iodo Groups. A Comparison of the Crystal Structures of Some 4-Phenoxyanilines. *CrystEngComm* **2004**, *6*, 642–646.

(17) Ebenezer, S.; Muthiah, P. T.; Butcher, R. J. Design of a Series of Isostructural Co-Crystals with Aminopyrimidines: Isostructurality through Chloro/Methyl Exchange and Studies on Supramolecular Architectures. *Crystal Growth and Design* **2011**, *11*, 3579–3592.

(18) Gelbrich, T.; Threlfall, T. L.; Hursthouse, M. B. XPac Dissimilarity Parameters as Quantitative Descriptors of Isostructurality: The Case of Fourteen 4,5′-Substituted Benzenesulfonamido-2-Pyridines Obtained by Substituent Interchange Involving CF3/I/Br/Cl/F/Me/H. *CrystEngComm* **2012**, *14*, 5454–5464.

(19) Cinčić, D.; Friščić, T.; Jones, W. Structural Equivalence of Br and I Halogen Bonds: A Route to Isostructural Materials with Controllable Properties. *Chemistry of Materials* **2008**, *20*, 6623–6626.

(20) Zou, S. J.; Shen, Y.; Xie, F. M.; Chen, J. De; Li, Y. Q.; Tang, J. X. Recent Advances in Organic Light-Emitting Diodes: Toward Smart Lighting and Displays. *Materials Chemistry Frontiers* **2020**, *4*, 788–820.

(21) Wei, B.; Xu, H.; Zhao, N.; Gao, X.; Ye, Y.; Wang, Y.; Yao, D.; Zhang, X.; Liu, X. Deep-Blue Organic Light-Emitting Diodes Based on Multi-Tert-Butyl Modified Naphthylene. *Journal of Industrial and Engineering Chemistry* **2021**, *102*, 44–50.

(22) Yan, L.; Popescu, F.; Rao, M. R.; Meng, H.; Perepichka, D. F. A Wide Band Gap

Naphthalene Semiconductor for Thin-Film Transistors. *Advanced Electronic Materials* **2017**, *3*, 1–8.

(23) Lin, Y.; Fan, H.; Li, Y.; Zhan, X. Thiazole-Based Organic Semiconductors for Organic Electronics. *Advanced Materials* **2012**, *24*, 3087–3106.

(24) Niyas, M. A.; Ramakrishnan, R.; Vijay, V.; Sebastian, E.; Hariharan, M. Anomalous Halogen–Halogen Interaction Assists Radial Chromophoric Assembly. *Journal of the American Chemical Society* **2019**, *141*, 4536–4540.

(25) Niyas, M. A.; Ramakrishnan, R.; Vijay, V.; Hariharan, M. Structure-Packing-Property Correlation of Self-Sorted Versus Interdigitated Assembly in TTF·TCNQ-Based Charge-Transport Materials. *Chemistry - A European Journal* **2018**, *24*, 12318–12329.

(26) John, A. T.; Narayanasamy, A.; George, D.; Hariharan, M. Atom-Efficient Halogen-Halogen Interactions Assist One-, Two-, and Three-Dimensional Molecular Zippers. *Journal of Physical Chemistry C* **2021**, *125*, 10716–10722.

(27) Ioka, S.; Saitoh, T.; Iwano, S.; Suzuki, K.; Maki, S. A.; Miyawaki, A.; Imoto, M.; Nishiyama, S. Synthesis of Firefly Luciferin Analogues and Evaluation of the Luminescent Properties. *Chemistry - A European Journal* **2016**, *22*, 9330–9337.

(28) Spackman, M. A.; Jayatilaka, D. Hirshfeld Surface Analysis. *CrystEngComm* **2009**, *11*, 19–32.

(29) Bader, R. F. W. A Quantum Theory of Molecular Structure and Its Applications. *Chemical Reviews* **1991**, *91*, 893–928.

(30) Contreras-García, J.; Johnson, E. R.; Keinan, S.; Chaudret, R.; Piquemal, J.-P.; Beratan, D. N.; Yang, W. NCIPLOT: A Program for Plotting Noncovalent Interaction Regions. *Journal of Chemical Theory and Computation* **2011**, *7*, 625–632.

(31) Kálmán, A.; Párkányi, L.; Argay, G. Classification of the Isostructurality of Organic Molecules in the Crystalline State. *Acta Crystallographica Section B Structural Science* **1993**, *49*, 1039–1049.

(32) CF, M.; I, S.; SJ, C.; PTA, G.; P, M.; E, P.; M, P.; GP, S.; JS, S.; M, T.; PA, W. Mercury 4.0: From Visualization to Analysis, Design and Prediction. *Journal of applied crystallography* **2020**, *53*, 226–235.

(33) Burley, S. K.; Petsko, G. A. Aromatic-Aromatic Interaction: A Mechanism of Protein Structure Stabilization. *Science* **1985**, *229*, 23–28.

(34) Spackman, P. R.; Turner, M. J.; McKinnon, J. J.; Wolff, S. K.; Grimwood, D. J.; Jayatilaka,

D.; Spackman, M. A. CrystalExplorer: A Program for Hirshfeld Surface Analysis, Visualization and Quantitative Analysis of Molecular Crystals. *Journal of Applied Crystallography* **2021**, *54*, 1006.

(35) Mackenzie, C. F.; Spackman, P. R.; Jayatilaka, D.; Spackman, M. A. CrystalExplorer Model Energies and Energy Frameworks: Extension to Metal Coordination Compounds, Organic Salts, Solvates and Open-Shell Systems. *IUCrJ* **2017**, *4*, 575–587.

(36) Turner, M. J.; Thomas, S. P.; Shi, M. W.; Jayatilaka, D.; Spackman, M. A. Energy Frameworks: Insights into Interaction Anisotropy and the Mechanical Properties of Molecular Crystals. *Chemical Communications* **2015**, *51*, 3735–3738.

(37) Whitesell, J. K.; Davis, R. E.; Saunders, L. L.; Wilson, R. J.; Feagins, J. P. Molecular Dipole Interactions Organization. *J Am Chem Soc* **1991**, *113*, 3267–3270.

(38) Dey, A.; Desiraju, G. R. Correlation between Molecular Dipole Moment and Centrosymmetry in Some Crystalline Diphenyl Ethers. *Chemical Communications* **2005**, No. 19, 2486.

(39) Blanco, M. A.; Pendás, A. M.; Francisco, E. Interacting Quantum Atoms: A Correlated Energy Decomposition Scheme Based on the Quantum Theory of Atoms in Molecules. *Journal of Chemical Theory and Computation* **2005**, *1*, 1096–1109.

(40) Nobbs, J. H. Kubelka-Munk Theory and the Prediction of Reflectance. *Review of Progress in Coloration and Related Topics* **2008**, *15*, 66–75.

(41) Tauc, J.; Grigorovici, R.; Vancu, A. Optical Properties and Electronic Structure of Amorphous Germanium. *physica status solidi (b)* **1966**, *15*, 627–637.

(42) Makuła, P.; Pacia, M.; Macyk, W. How To Correctly Determine the Band Gap Energy of Modified Semiconductor Photocatalysts Based on UV–Vis Spectra. *The Journal of Physical Chemistry Letters* **2018**, *9*, 6814–6817.

(43) Yang, F.; Li, C.; Lai, W.; Zhang, A.; Huang, H.; Li, W. Halogenated Conjugated Molecules for Ambipolar Field-Effect Transistors and Non-Fullerene Organic Solar Cells. *Materials Chemistry Frontiers* **2017**, *1*, 1389–1395.

(44) Burke, K. Perspective on Density Functional Theory. *The Journal of Chemical Physics* **2012**, *136*, 150901.

(45) Mackenzie, C. F.; Spackman, P. R.; Jayatilaka, D.; Spackman, M. A. CrystalExplorer Model Energies and Energy Frameworks: Extension to Metal Coordination Compounds, Organic Salts, Solvates and Open-Shell Systems. *urn:issn:2052-2525* **2017**, *4*, 575–587.

(46) Hohenberg, P.; Kohn, W. Inhomogeneous Electron Gas. *Physical Review* **1964**, *136*, B864–B871.

(47) Kohn, W.; Sham, L. J. Self-Consistent Equations Including Exchange and Correlation Effects. *Physical Review* **1965**, *140*, A1133.

(48) Grimme, S. Semiempirical GGA-Type Density Functional Constructed with a Long-Range Dispersion Correction. *Journal of Computational Chemistry* **2006**, *27*, 1787–1799.

(49) Barone, V.; Casarin, M.; Forrer, D.; Pavone, M.; Sambi, M.; Vittadini, A. Role and Effective Treatment of Dispersive Forces in Materials: Polyethylene and Graphite Crystals as Test Cases. *Journal of Computational Chemistry* **2009**, *30*, 934–939.

(50) Hinuma, Y.; Pizzi, G.; Kumagai, Y.; Oba, F.; Tanaka, I. Band Structure Diagram Paths Based on Crystallography. *Computational Materials Science* **2017**, *128*, 140–184.

(51) Togo, A.; Tanaka, I. $\texttt{Spglib}$: A Software Library for Crystal Symmetry Search. **2018**.

Chapter 4

Resonance-Assisted Hydrogen Bonding and π−π Stacking Modulates the Charge Transfer Coupling in Crystalline Naphthothiazoles

Abstract: Supramolecular chemistry employs noncovalent interactions to coax π-conjugated molecules into ordered functional assemblies. Herein, we report 5-methoxynaphtho[1,2-*d*]thiazol-2-amine (NTN) and 4-bromo-5-methoxynaphtho[1,2-*d*]thiazol-2- amine (NTNB) assembled into π-stacked columns integrated by lateral resonance-assisted hydrogen bonds (RAHBs) orthogonal to the π−π stacking direction. Quantum theory of atoms in molecules (QTAIM) and interacting quantum atoms (IQA) analyses were utilized to characterize the presence and stability of intermolecular RAHBs in NTN and NTNB. In contrast to the parallel packing of NTN, bromine substitution promoted antiparallel packing in NTNB with noticeable π−π stacking and orbital overlap favoring efficient charge transfer coupling (Ve/h). Antiparallel stacking in NTNB exhibits a dipole moment minimization and aromaticity gain. The relevance of aromaticity in stabilizing π−π stacked systems is highlighted by the aromaticity gain in antiparallel stacked dimers of NTNB and can be extended to estimate the nature and strength of noncovalent interactions. Crystal packing plays a crucial role in regulating the charge transport properties, as can be observed from higher electron and hole transfer coupling along the π−π stacked and RAHB dimer, respectively, in NTN. However, in NTNB maximum electron and hole transfer coupling occurs selectively

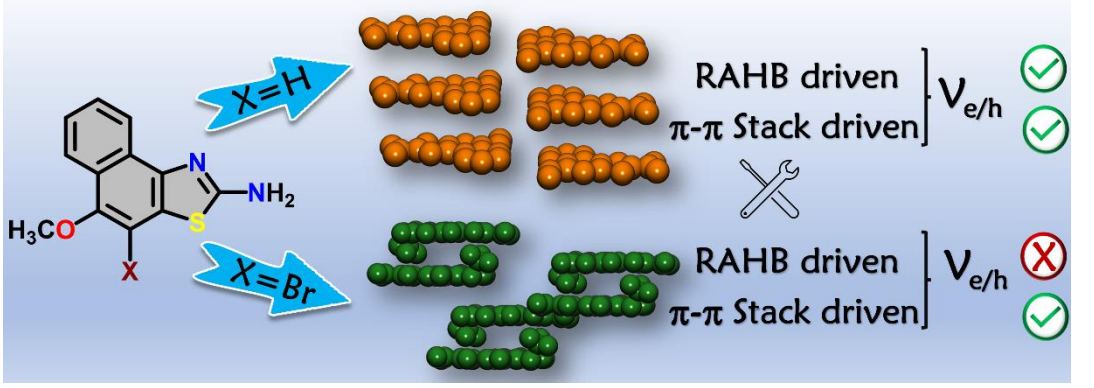

along the π−π stacked antiparallel dimer. The anisotropic mobility plots from a combination of first-principles quantum chemical calculations and the Marcus−Hush formalism confirm that both RAHB and π−π stacked dimers contribute to the mobility in NTN, but NTNB exclusively benefits from the π−π stacked dimer. Modulating noncovalent interactions for charge carrier transport can harness the innate potential of organic molecules to engineer novel optoelectronic materials.

4.1. Introduction

The design of small organic chromophores with precise control of intermolecular interactions plays an imperative role in the odyssey of organic electronics.[1] The solid-state packing[1] of molecules in organic semiconductors is pivotal for charge generation and transport in devices such as organic field-effect transistors (OFETs),[2] organic photovoltaics (OPVs),[3] and organic light-emitting diodes (OLEDs).[4] Charge transport at the molecular level strongly depends upon two factors: the reorganization energy and the electronic coupling.[5] The electronic coupling (transfer integral) is predominantly correlated to the molecular packing mode.[6,7] Crystal engineering aims to comprehend the intermolecular interactions controlling crystal packing and plays a vital role in designing organic optoelectronic materials. Herringbone or brickstone molecular arrangements with strong π−π stacking were found to exhibit enhanced carrier mobility in organic semi-conductors.[8–11] Continuous efforts were made to increase face-to-face contacts to boost charge transport by promoting π−π stacking in fused aromatic units.[12] Long-range charge transport along hydrogen bonds (HBs) has been theoretically predicted in diketopyrrolopyrrole and perylene diimide pigments.[10,13] The hydrogen-bonding interaction encourages strong intermolecular electronic coupling by enhancing electron delocalization and resonance and accordingly alters the charge transport properties.[13] Resonance-assisted hydrogen bonds (RAHBs) proposed by Gilli et al. are stronger than conventional HBs due to the extra stabilization arising from the partial delocalization of the π-electrons within the HB motif.[14,15] The π-delocalization results in enhancement of positive charge on the HB donor and negative charge on the HB acceptor, establishing an electrostatic interaction as a major contributor to the total HB energy.

In addition, aromaticity can be employed in the framework of crystal engineering to design efficient supramolecular synthons.[16,17] [Anti]aromaticity gain or loss was found to modulate the strength of hydrogen bonds,[18] enhance charge transport behavior in n-type nonaromatic organic dyes upon forming HB,[19] enable conductivity in electronic devices,[20] and enhance the basicity of

organic superbases.[21] The study of charge transport properties in DNA base pair stacks has gained considerable attention in the scientific community.[22–24] Exploring continuous π−π stacked hydrogen-bonded chromophoric assemblies mimicking the nonhelical structure of DNA base-pair stacks[25–27] could beget intriguing charge transport properties. Getmanenko, Risko, and co-workers reported theoretical evidence for ambipolar mobility along edge-to-edge contacts in 7,7,8,8-tetracyanoquinodimethane (TCNQ) and dithieno[3,2-a:2′,3′-c]phenazine (DTPhz).[28] The inter play of hydrogen bonding and π−π stacking interactions influences charge transfer in small organic cocrystals exhibiting ambipolar charge transport.[29] Naphthalene- and thiazole-based molecular systems have been exploited as potential materials in the field of organic electronics and act as lead compounds in the development of pharmaceutical drugs.[30–32] Our ongoing interest in probing the origin of supramolecular structural motifs with emergent properties[33–35] employing weak interactions motivated us to design novel naphthothiazole[36,37] derivatives. To investigate the role of RAHB and π−π stacking interactions in charge transfer coupling, we integrated HB acceptor and donor sites to design novel 5-methoxynaphtho-[1,2-*d*]thiazol-2-amine (NTN) and 4-bromo-5-methoxynaphtho[1,2-*d*]thiazol-2-amine(NTNB) polyheteroatomic aro- matic systems whose molecular packing is predominantly driven by RAHB and π−π stacking interactions.

4.2. Results and Discussion

Cyclization of 4-methoxynaphthalen-1-amine with potassium thiocyanate in the presence of a catalytic amount of bromine and excess bromine afforded 5-methoxynaphtho[1,2-*d*]thiazol-2-amine (NTN) and 4-bromo-5-methoxynaphtho[1,2-*d*]- thiazol-2-amine (NTNB), respectively (Figure 4.1 and Scheme 4.1). Single crystals of NTN and NTNB with space groups $P2_1/c$ and $P2_1/n$, respectively, were obtained through slow evaporation from ethyl acetate under ambient conditions (Table 4.1). The novel crystalline NT derivatives (NTN and NTNB) obtained were characterized by spectroscopic and analytical techniques. Close-packing analyses of NT derivatives were executed to gain an inclusive understanding of the structure−property relationship. Intermolecular N−H•••C (d = 2.71 Å) to C−H•••C (d = 2.86 Å) and aromatic C•••C (d = 3.53−3.62 Å) interactions guide the propagation of a three-dimensional (3D) crystalline assembly in NTN. Interactions such as C−H•••H−C (d = 2.10 Å), S•••π (d = 3.29−3.49 Å), aromatic C•••C (d = 3.50−3.58 Å), Br•••N (d = 3.89 Å), and Br•••H (d = 3.40 Å) dictate the

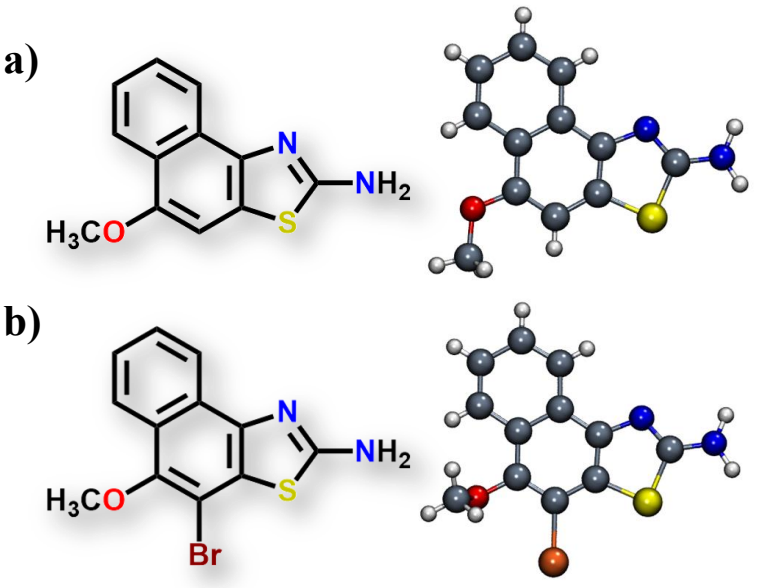

Figure 4.1: Chemical and X-ray molecular structures of (a) NTN and (b) NTNB.

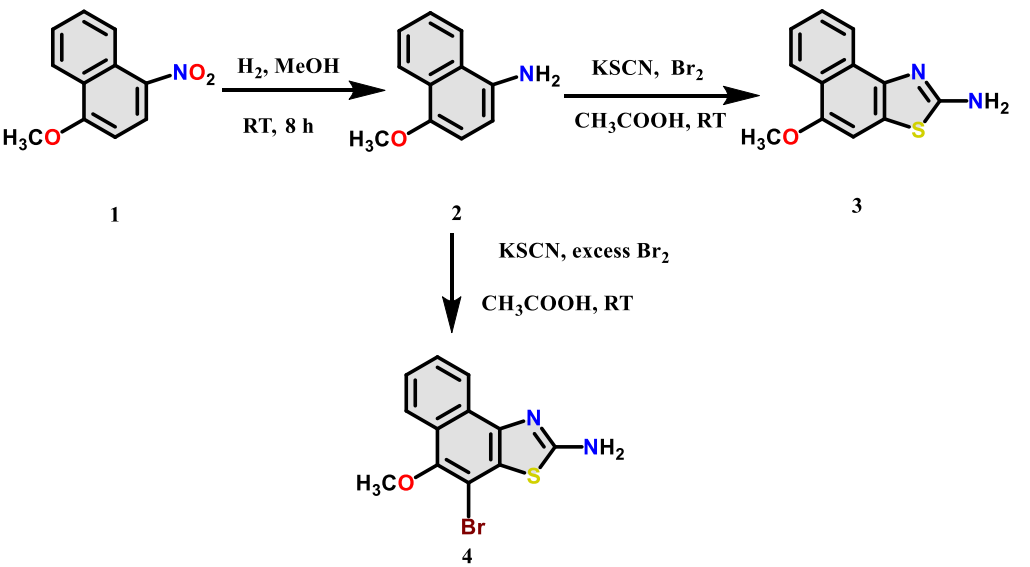

Scheme 4.1: Reaction scheme for the synthesis of NTN (3) and NTNB (4).

packing arrangement in NTNB. Essential features of the NT molecular crystals are the presence of strong intermolecular N−H•••N RAHBs (Figure 4.2).[14,15,38] In a RAHB system, the proton donor and acceptor groups are connected through a chain of delocalized conjugated double bonds, stabilizing the molecular unit. According to the RAHB rules, the strengthening of a N− H•••N bond is associated with shortening and lengthening of all single- and double-bond distances, respectively. The N•••H intermolecular contacts that are considered here are less than their sum of van der Waals radii by 0.4 Å. The RAHB concept can be extended to any heteroconjugated system with an HB donor (D) and acceptor (A) connected by a conjugated chain with an odd

Table 4.1: Crystallographic data and refinement parameters for NTN and NTNB.

Parameters	NTN	NTNB
Formula	$C_{12}H_{10}N_2OS$	$C_{12}H_9BrN_2OS$
Formula weight	230.28	309.18
Color	Light grey	Light pink
Crystal system	Monoclinic	Monoclinic
Space group, Z	P 2_1/c	P 2_1/n
a (Å)	12.675(7)	9.5834(10)
b (Å)	5.049(2)	9.2690(9)
c (Å)	17.452(9)	13.3700(14)
α, deg	90	90
β, deg	109.963(16)	96.673(4)
γ, deg	90	90
Volume, $Å^3$	1049.75	1179.59
R factor	3.26	4.15
Temp, K	293(2)	296(2)
$d_{calculated}$ (mg/m^3)	1.457	1.741
No. of reflections collected	8226	10452
No. of unique reflections	1834	2075
$2\theta_{max}$, deg	25.000	24.997
No. of parameters	154	162
R1, wR2, (I > 2s(I))	0.0326, 0.0809	0.0415, 0.1075
R1, wR2 (all data)	0.0411, 0.0899	0.0560, 0.1164
Goodness of fit	1.045	1.051
CCDC number	2181541	2181542

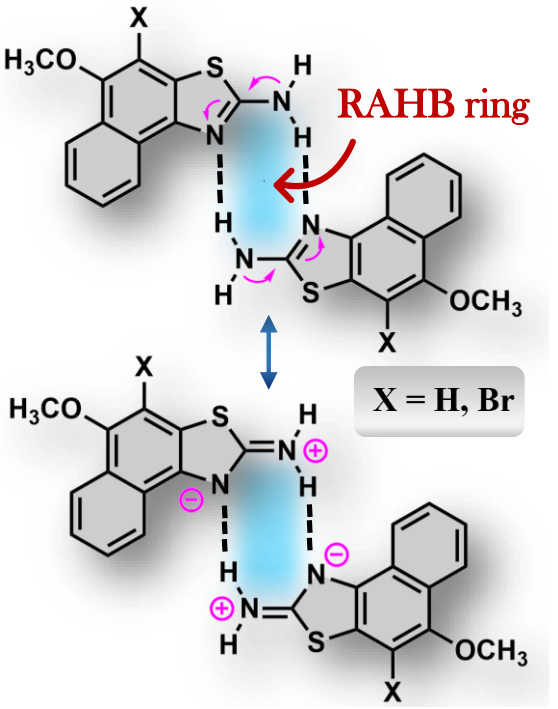

Figure 4.2: Resonance-assisted intermolecular hydrogen bonding in NT derivatives.

number of atoms n, where n = 2N +1 (N is a positive integer, including zero).[38] The RAHB fragments in NT crystals fall into the category mentioned above with N = 0. Fourier transform infrared (FT-IR) spectroscopy was used to characterize the intermolecular hydrogen bonding in NTN and NTNB. Characteristic peaks between 3500 and 3310 cm^{-1} in FT-IR spectra indicate an N−H stretching vibration. The 1650−1580 cm^{-1} band is associated with N−H bending. The peak at 680 cm−1 in NTNB corresponds to C−Br stretching.

Bader's quantum theory of atoms in molecules (QTAIM) approach was used to characterize the strength and nature of intermolecular HB motifs. Table 4.2 summarizes the topological parameters for N−H•••N interactions in the NT crystals (Figure 4.3). A positive value of the Laplacian ($\nabla^2\rho > 0$) $|-V/G| < 1$ suggests that the RAHBs are closed-shell in nature. The results from QTAIM are visualized by noncovalent interaction (NCI) analyses, where the attractive interactions are distinguished by green disks in the area of the ring critical point (RCP), bond critical point (BCP), and cage critical point (CCP) (Figure 4.4). The interacting quantum atoms (IQA) method was employed to investigate the nature of interactions involved in the RAHB ring. The intermolecular N−H•••N interaction has stabilizing total IQA interaction energy values of −100.44 and −99.45 kcal/mol for NTN and NTNB, respectively (Table 4.3). The exceptionally

Table 4.2: Calculated topological properties of electron density function for the intermolecular interactions in crystalline NTN and NTNB.

		Interactions	d, Å	ρ(r), eÅ^{-3}	$\nabla^2\rho(r)$, eÅ^{-5}
NTN	Bond critical points (BCPs)	N47•••H25	2.071	0.02211	0.07229
		N21•••H51		0.02211	0.07229
NTNB	Bond critical points (BCPs)	N46•••H25	2.085	0.02141	0.07013
		N20•••H51		0.02141	0.07012

high value of the stabilization energy of the HB in the NT crystals is a possible consequence of RAHB.[39] The total IQA value is partitioned into an exchange-correlation component and a classical Coulombic component. In both NT crystals the major stabilization to the RAHB arises from electrostatics. Crystalline NTN exhibits a one-dimensional (1D) dimeric slip-stacked assembly involving a symmetric pair of intermolecular N−H•••N (d = 2.07 Å) HBs. Crystalline NTNB displays an antiparallel cofacial stacked assembly possessing intermolecular N−H•••N (d = 2.08 Å) HBs. Symmetry-adapted perturbation theory (SAPT(0))[40] energy decomposition analysis was performed to gain insights into the nature of interactions stabilizing the crystalline

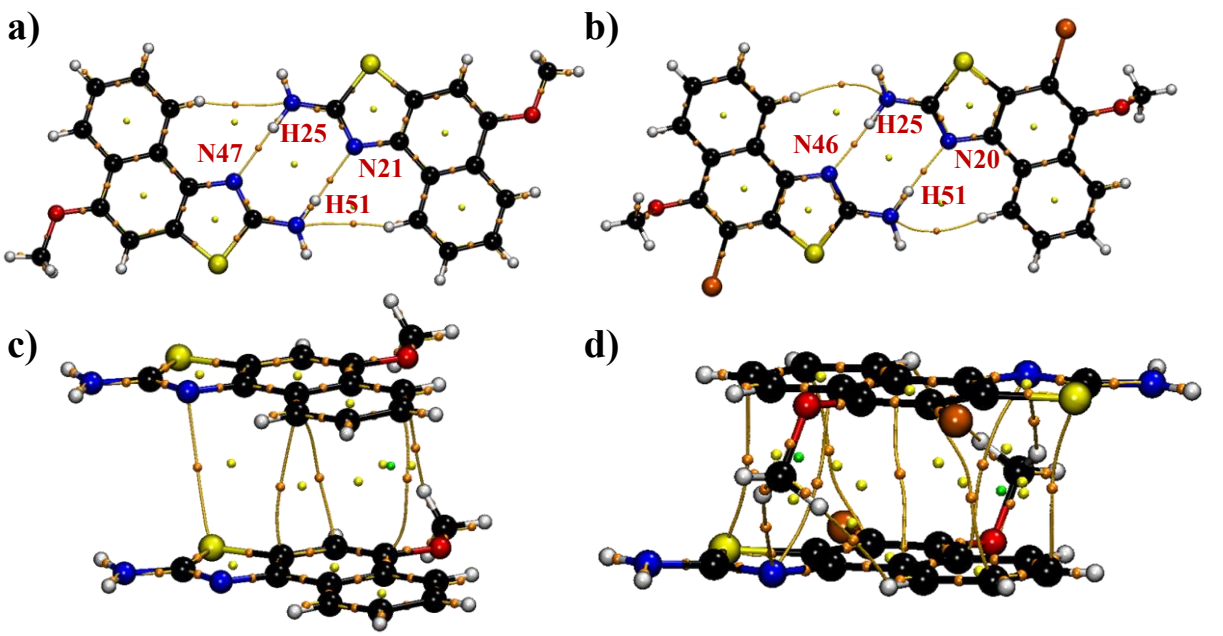

Figure 4.3: QTAIM electron density map showing N•••H interactions in RAHB dimer of a) NTN b) NTNB and π-π stack of c) NTN d) NTNB.

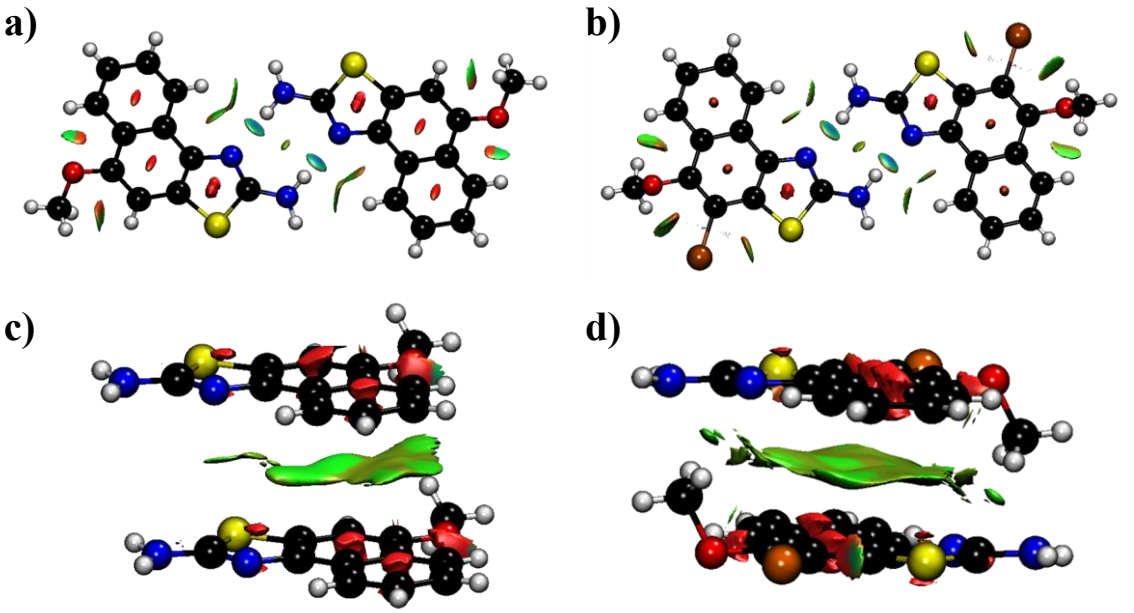

Figure 4.4: NCI plot showing weak stabilizing interactions represented as green discs in RAHB dimers of a) NTN b) NTNB and π-π stack stacked dimers of c) NTN d) NTNB.

packing in NTN and NTNB. The method decomposes the total interaction energy into electrostatic, dispersion, induction, and exchange repulsion energy components. Negative SAPT(0) values of −14.01 and −12.63 kcal/mol show the stabilizing nature of RAHB dimers in the solidstate packing of NTN and NTNB (Table 4.4), respectively.

The centrosymmetric dimers of NTN and NTNB are connected through amine groups by two equivalent N−H···N HBs classified as the $R_2^2(8)$ motif (Figure 4.5) according to the graph theory assignments.[41] The HB motifs are generally depicted as $R_d^a(r)$, where R is the ring motif, a is the number of HB acceptors, d is the number of HB donors, and r is the number of atoms in the ring

Table 4.3: IQA interaction energies. Total noncovalent interaction energies and its components of NTN and NTNB are shown. Energies are given in kcal/mol.

Molecule	Interactions	E_t	E_{xc}	E_{cl}
NTN	N47•••H25	-100.48	-10.14	-90.34
	N21•••H51	-100.45	-10.14	-90.31
NTNB	N46•••H25	-99.46	-9.64	-89.82
	N20•••H51	-99.45	-9.64	-89.81

Table 4.4: Interaction energies of representative NTN and NTNB hydrogen bonded dimers from SAPT(0) aug-cc-pvdz calculations.

Molecule	E_{int}^{SAPT}	$E_{ele}^{(1)}$	$E_{dis}^{(2)}$	$E_{ind}^{(2)}$	$E_{ex}^{(1)}$
NTN	-14.01	-17.66	-8.36	-6.00	18.01
NTNB	-12.63	-16.02	-8.16	-5.58	16.02
All energy values are provided in kcal/mol. E_{int}^{SAPT} = Total interaction energy; $E_{ele}^{(1)}$ = Electrostatic; $E_{dis}^{(2)}$ = Dispersion; $E_{ind}^{(2)}$ = Induction and $E_{ex}^{(1)}$ = Exchange repulsion energy.					

motif. Hirshfeld surface (HS)[42] and two-dimensional (2D) fingerprint analyses (Figures 4.6 and 4.7) were performed to gain insight into the packing motifs and quantification of weak intermolecular interactions in crystalline NT derivatives. Table 4.5 shows the percentage of intermolecular interactions in crystalline NTs. The ratio (ρ) of %C•••H to %C•••C interactions defines the packing modes adopted by the crystalline assembly. The NTN crystal possesses a herringbone packing arrangement (ρ = 4.52), while NTNB (ρ = 1.77) has a γ-packing motif (Figure 4.5).[33,43] A dominating presence of H•••H interactions is observed from the HS analysis in the crystal packing of NTs. An electrostatic surface potential (ESP) map was generated to visualize the charge distribution in NT crystals (Figure 4.8). The color gradient from red to blue in ESP correlates to the varying intensities of the electrostatic potential energy values from negative to positive. A red region on the aryl rings

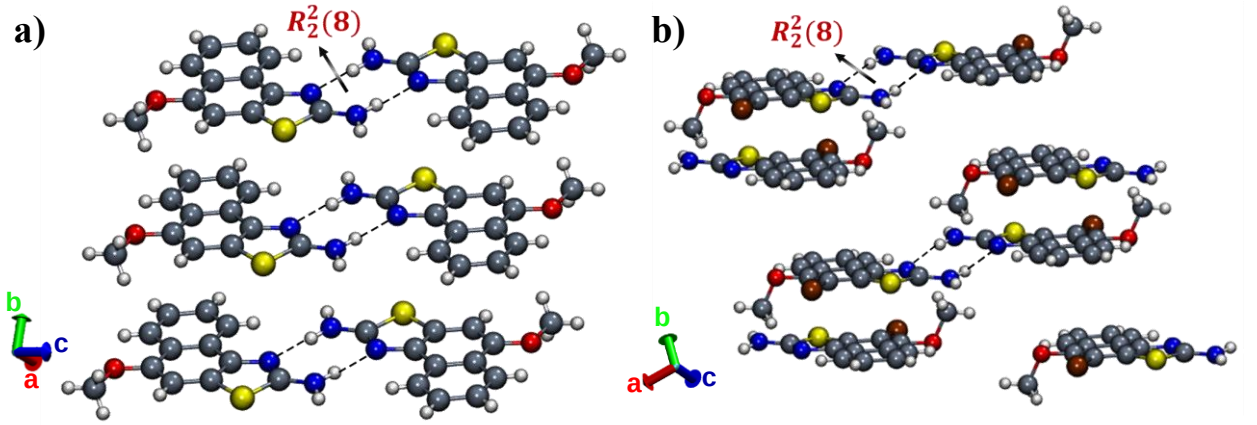

Figure 4.5: Packing arrangement in crystalline (a) NTN and (b) NTNB derivatives.

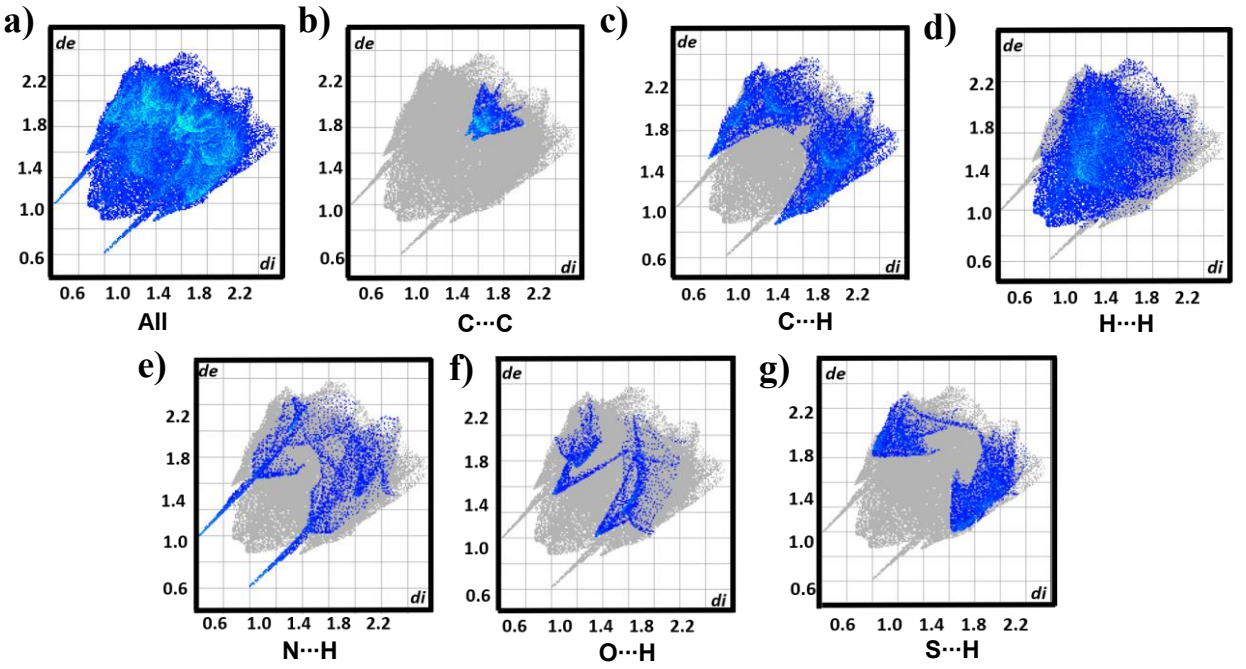

Figure 4.6: 2-dimensional fingerprint plots showing a) total b) C•••C c) C•••H d) H•••H e) N•••H f) O•••H g) S•••H interactions in NTN.

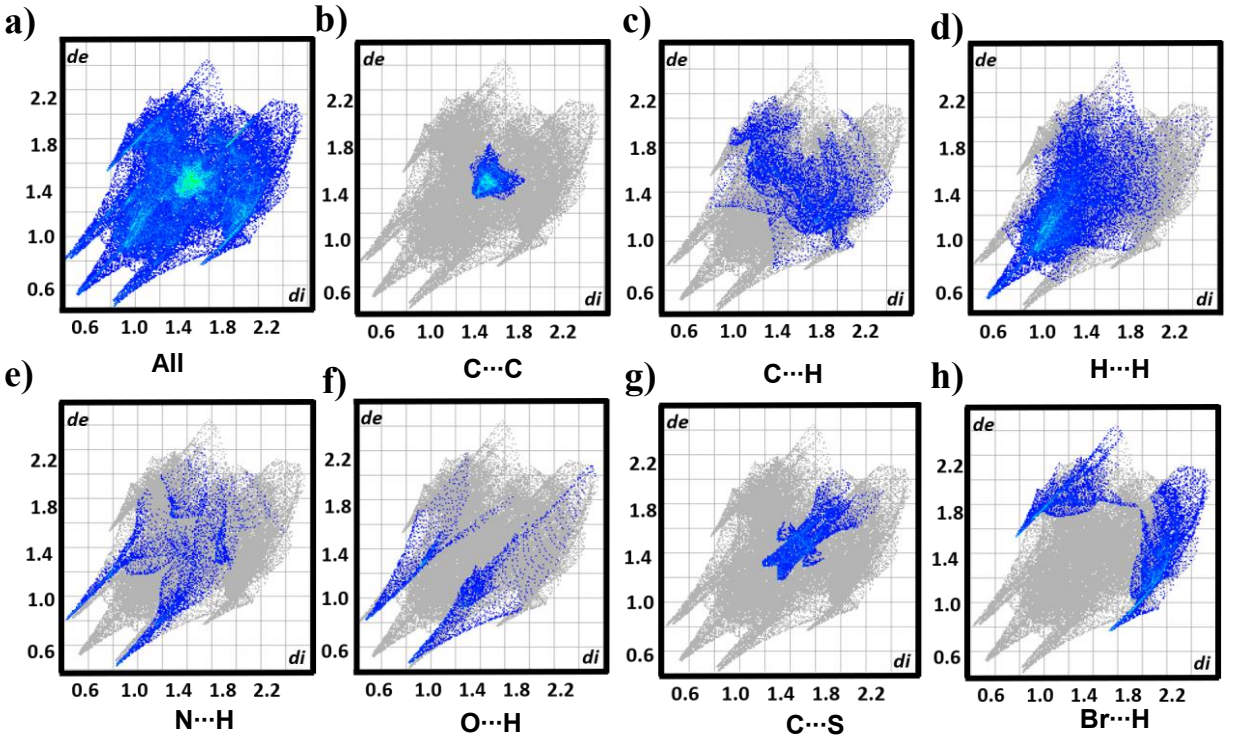

Figure 4.7: 2-dimensional fingerprint plots showing a) total b) C•••C c) C•••H d) H•••H e) N•••H f) O•••H g) C•••S h) Br•••H interactions in NTNB.

Table 4.5: Relative % of intermolecular interactions obtained from Hirshfeld analysis for NTN and NTNB.

Interaction	C•••C	C•••H	O•••H	N•••H	S•••H	H•••Br	H•••H	C•••S	ρ=[(%C•••C)/(%C•••H)]
NTN	5.9	26.7	5.2	8.8	11.5	0	38.4	0.8	4.52
NTNB	7.2	12.8	5.9	8.5	6.2	15.9	30.6	7.9	1.77

indicates localized electron density, and the blue positive potential region represents electron-deficient regions in NT derivatives. A significant difference in charge distribution of the aromatic core is observed with the introduction of a halogen atom. As can be observed, for NTN and NTNB, intermolecular HB donors and acceptors appear as blue (positive ESP) and red (negative ESP) regions on the ESP surface. The electrostatic complementarity among the electron-rich and -deficient zones directs the favorable stacking interactions in the crystal packing of NTs. The σ-hole on the halogen atom in NTNB appears as a distinguishable region of positive electrostatic potential, surrounded by an electron-rich equatorial belt.

Molecules in organic crystals typically align in an antiparallel fashion among the proximate neighbors in the crystal to minimize the net dipole moment.[44] The heteroatoms in NTN and NTNB offer net dipole moments of 2.74 and 2.45 D, respectively. The RAHB dimers of NTN, NTNB, and the antiparallel π-stacked dimer in NTNB possess a negligible dipole moment, attaining the design goal of dipole minimization (Table 4.6). We probed the role of aromaticity in directing the close packing of NT crystals by evaluating the aromaticity variation

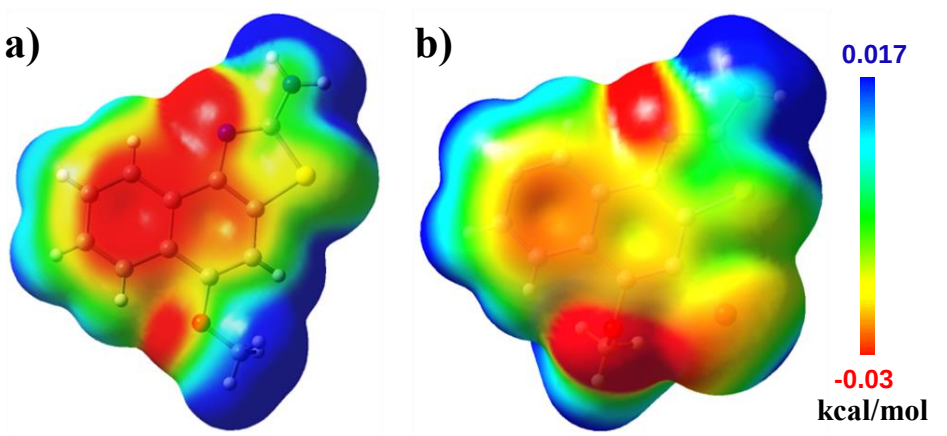

Figure 4.8: ESP maps (0.002 isodensity surface) of (a) NTN and (b) NTNB.

Table 4.6: Magnitudes of dipole moments (Debye) for monomer and different dimers in the crystal packing of NTN and NTNB.

NT derivatives		Dipole moment (Debye)
NTN	Monomer	2.83
	RAHB dimer	0.00
	π-π stack dimer (parallel)	5.67
NTNB	Monomer	2.66
	RAHB dimer	0.00
	π-π stack dimer (anti-parallel)	0.00

in RAHB and π−π stacked dimers of NTN and NTNB. Dissected nucleus-independent chemical shifts,[45,46] $NICS_{zz}(1)$, were calculated at the ωB97XD/Def2- TZVP level of theory at 1 Å above the centroid of each ring of the monomer (Figure 4.9) and dimer (Figures 4.10 and 4.11) to quantify the changes in the aromatic character of NTN and NTNB upon dimerization. $\Delta NICS_{zz}(1)$ = $NICS_{zz}(1)$(dimer) − $NICS_{zz}(1)$(monomer), where a positive $\Delta NICS_{zz}(1)$ indicates an enhancement in the antiaromatic character in the RAHB or π−π stacked dimers in comparison to the monomer and a negative value signifies the opposite. The thiazole ring participating in hydrogen bonding shows positive $\Delta NICS_{zz}(1)$ values, suggesting disruption of the aromaticity in the RAHB dimers of NTN and NTNB (Tables 4.7 and 4.8). The parallel π−π stacked dimer of NTN shows $\Delta NICS_{zz}(1)$ values of −0.17, 0.49, and 0.91 ppm for rings a′, b′, and c′, respectively, indicating a decrease in aromaticity in rings b′ and c′, though ring a′ exhibits a marginal aromaticity gain (Table 4.9). However, the antiparallel π−π stacked dimer of NTNB exhibits notably negative $\Delta NICS_{zz}(1)$ values of −2.60, −5.30, and −3.95 ppm for rings a′, b′, and c′, respectively, depicting an aromaticity gain in the π−π stacked antiparallel dimer (Table 4.10).

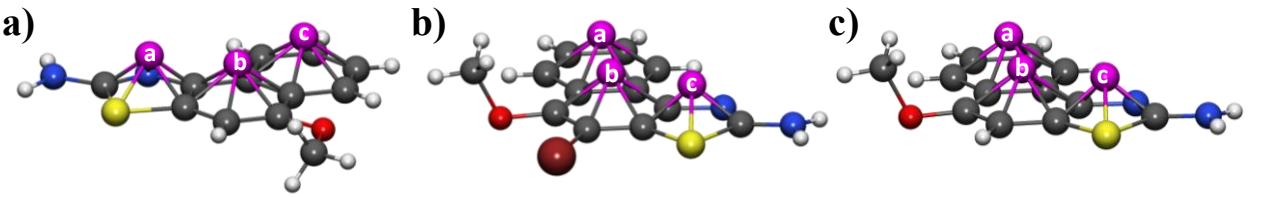

Figure 4.9: Schematic illustration of NICS probes placed at 1 Å above the centroid of each ring of monomer a) NTN b) NTNB and c) NTNH.

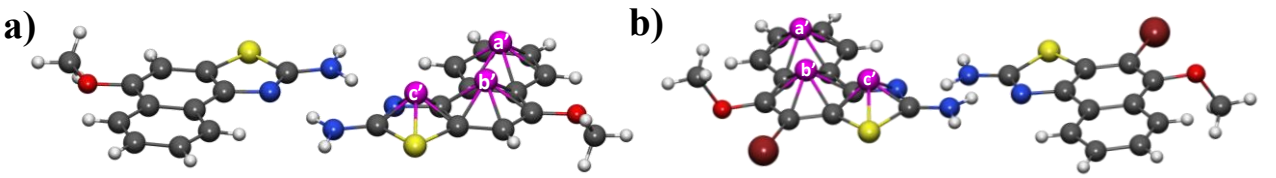

Figure 4.10: Schematic illustration of NICS probes placed at 1 Å above the centroid of each ring in RAHB dimers a) NTN and b) NTNB.

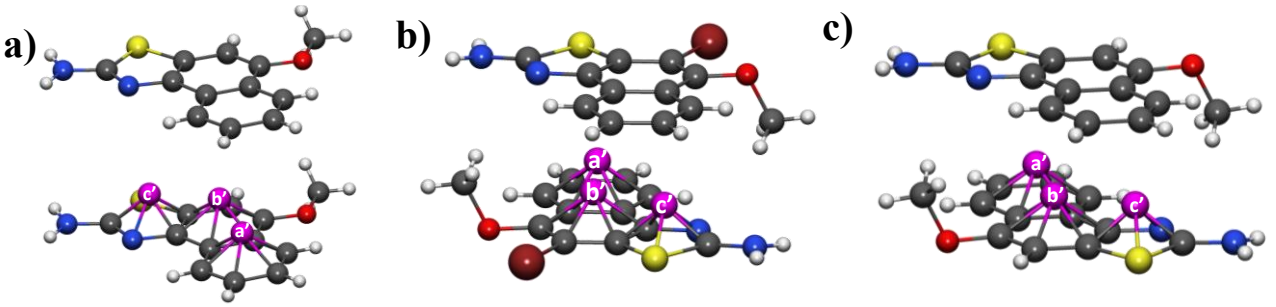

Figure 4.11: Schematic illustration of NICS probes placed at 1 Å above the centroid of each ring in π-π stacked dimers a) NTN b) NTNB and c) NTNH.

To decouple the effect of bromine atom and antiparallel packing in the aromaticity gain of NTNB, we computed $\Delta NICS_{zz}(1)$ for the antiparallel π−π stacked dimer of NTNB by replacing a bromine atom with a hydrogen atom (NTNH). To our surprise, the $\Delta NICS_{zz}(1)$ values in the modified dimer were −1.78, −4.88, and −3.73 ppm for rings a′, b′, and c′, respectively, clearly establishing the effect of aromaticity in stabilizing the antiparallel packing (Table 4.11). The charge transfer mechanism and its stabilization energies of N−H•••N contacts formed in both NTN and NTNB were further characterized by performing a natural bonding orbital (NBO)[47] analysis on the hydrogen-bonded dimer. The second-order perturbation energies due to the charge delocalization between the lone pair of the nitrogen atom and the antibonding σ* orbital of the N−H bond are provided in Table 4.12. The stabilization energies for the N−H•••N HB in NTN and NTNB are 7.70 and 6.26 kcal/mol, respectively. The merging lobes indicating orbital overlap between the donor and acceptor NBOs associated with HBs are given in Figure 4.12.

We now discuss the role of π−π stacking and RAHB in guiding the supramolecular assembly of NT crystals in the emergent charge transport properties predicted from the quantum chemical simulations.[9,48,49] Intermolecular electronic coupling and reorganization energy play a vital role in determining the rate of charge transfer.[48] The inner-sphere reorganization energy ($\lambda_{e/h}$) takes into account the energy associated with the geometric reorganization from the nuetr

Table 4.7: $NICS_{ZZ}$ (1) calculated for NTN monomer and RAHB dimer. a, b, and c represent the rings in monomer and a', b', and c' represent the corresponding rings in the dimer. $NICS_{ZZ}$ (1) units are in ppm. $\Delta NICS_{ZZ}$ (1) = $NICS_{ZZ}$ (1) (dimer) – $NICS_{ZZ}$ (1) (monomer).

Ring number	$NICS_{ZZ}$ (1)	$\Delta NICS_{ZZ}$ (1)
a	-1.33	-0.44
a'	-1.77	
b	-3.38	-0.25
b'	-3.63	
c	-3.54	0.40
c'	-3.14	

Table 4.8: $NICS_{ZZ}$ (1) calculated for NTNB monomer and RAHB dimer.

Ring number	$NICS_{ZZ}$ (1)	$\Delta NICS_{ZZ}$ (1)
a	-10.03	0.35
a'	-9.68	
b	-7.01	0.20
b'	-6.81	
c	-7.72	0.53
c'	-7.19	

Table 4.9: $NICS_{ZZ}$ (1) calculated for monomer and parallel π-π stacked dimer of NTN.

Ring number	$NICS_{ZZ}$ (1)	$\Delta NICS_{ZZ}$ (1)
a	-1.33	-0.17
a'	-1.50	
b	-3.38	0.49
b'	-2.89	
c	-3.54	0.91
c'	-2.63	

Table 4.10: $NICS_{zz}$ (1) calculated for NTNB monomer and antiparallel π-π stacked dimer.

Ring number	$NICS_{ZZ}$ (1)	$\Delta NICS_{ZZ}$ (1)
a	-10.03	-2.60
a’	-12.62	
b	-7.01	-5.30
b’	-12.30	
c	-7.72	-3.95
c’	-11.67	

Table 4.11: $NICS_{zz}$ (1) calculated for monomer and antiparallel π-π stacked dimer of NTNH.

Ring number	$NICS_{ZZ}$ (1)	$\Delta NICS_{ZZ}$ (1)
a	-9.60	-1.78
a’	-11.38	
b	-5.43	-4.88
b’	-10.31	
c	-6.98	-3.73
c’	-10.71	

Table 4.12: Selected donor-acceptor natural bond orbital interactions with their corresponding second-order perturbation stabilization energies of N-H•••N RAHB dimers in NTN and NTNB. Energies are given in kcal/mol.

Dimer	Donor NBO	Acceptor NBO	E(2)
NTN	LP(1) N21	BD*(1) N48-H51	7.7
	LP(2) N47	BD*(1) N22-H25	7.7
NTNB	LP(2) N20	BD*(1) N49-H51	6.26
	LP(1) N46	BD*(1) N23-H25	6.26

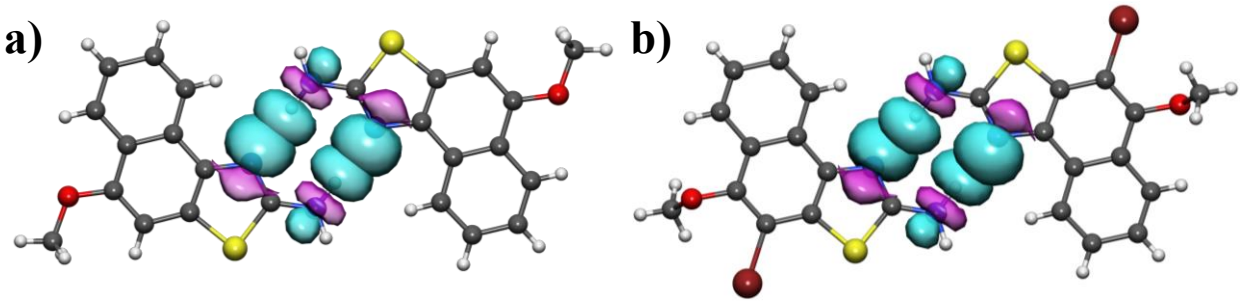

Figure 4.12: NBO plots of the donor and acceptor orbitals involved in the RAHB interaction in a) NTN and b) NTNB.

al state to the corresponding charged state in the electron or hole transfer process.[50] The outer-sphere reorganization energy was not evaluated due to the small value and large computational cost.[51,52] The charge transfer integral ($V_{e/h}$) of a crystalline organic chromophoric pair is known to be highly sensitive to the spatial orientations, noncovalent interactions, and intermolecular distance between the chromophores.6 π–π stacks play a vital role in modulating the charge transport process.[12,48,53] NTN exhibits π–π stacking along the b axis at an intermolecular distance of 5.0 Å, while NTNB's π–π stacks align in a antiparallel orientation, at a comparatively shorter distance of 3.4 Å. On comparison of the π–π stacked dimers of NT crystals, the electron transfer coupling (V_e) is twice the hole transfer coupling (V_h) (Table 4.13), which can be associated with an improved overlap of LUMO−LUMO orbitals relative to HOMO−HOMO orbitals (Figure 4.13). The RAHB dimer in a crystalline NT exists nearly orthogonally to the π–π stacked dimer with similar HB lengths (2.07 and 2.08 Å for NTN and NTNB, respectively). The hole transfer coupling in the RAHB dimer is comparatively higher for NTN (V_h = 36 meV) compared to that of NTNB (V_h = 8 meV), while the electron transfer coupling is equal (V_e = 18 meV). In contrast to the π–π stacked dimers of NT crystals, the RAHB dimer of NTN exhibits a higher hole transfer coupling (V_h = $2V_e$). However, the RAHB dimer of NTNB possesses a higher electron transfer coupling ($V_e \approx 2V_h$). The higher V_h and lower V_e of the RAHB dimer in NTN is possibly due to the better overlap of the HOMO−HOMO orbitals in comparison to the LUMO−LUMO orbitals. RAHB has indirectly facilitated the overlap of the HOMO−HOMO orbital wave function in NTN more than in NTNB. The reorganization energies of NT crystals were found to be higher than the coupling values; hence, the charge transfer rate was calculated according to the hopping mechanism ($2V_{e/h} < \lambda_{e/h}$).[53] A charge transport simulation was carried out based on Marcus−Hush theory and first-principles quantum chemical calculations. A large transfer integral and small reorganization energy are favorable for enhancing the charge transfer rate. The rate of charge transfer (k_i),

Table 4.13: Electron and hole transfer coupling values of selected dimers of NTN and NTNB.

Molecule	Dimer type	V_e (meV)	V_h (meV)
NTN	Stacked dimer	55	29
	RAHB dimer	18	36
NTNB	Stacked dimer	62	33
	RAHB dimer	18	8

representing the rate of electron/ hole hopping from a monomer to the ith neighbor was obtained through the Marcus−Hush equation[54]

$$k_i = \frac{{V_{e/h}}^2}{\hbar}\left(\frac{\pi}{\lambda_{e/h} k_B T}\right)^{\frac{1}{2}} \exp\left(-\frac{\lambda_{e/h}}{4 k_B T}\right)$$

where V_e and V_h are the electron and hole transfer couplings between the monomers of a dimer, respectively, k_B is the Boltzmann constant, and T is the temperature (300 K). The value of the reorganization energy inversely affects the rate of electron transfer.[55] The NT crystal hole reorganization energies are greater than the electron reorganization energies (Table 4.14), while V_h values were lower than the V_e values (Table 4.13). As a result, the rate at which hole transfer

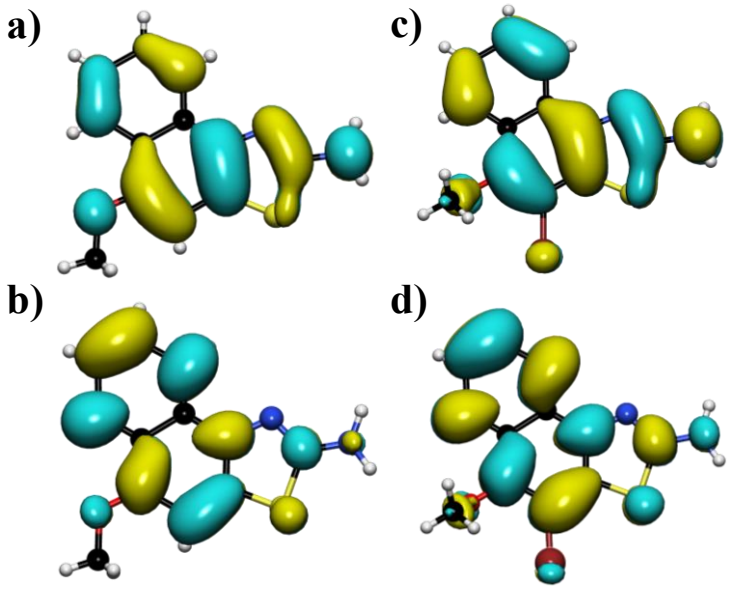

Figure 4.13: HOMOs (a, c) and LUMOs (b, d) of NTN and NTNB (isosurface value 0.02), respectively.

takes place is lower in comparison to the electron transfer. The drift mobility (μ) was calculated employing Einstein's relation:[54]

$$\mu = \frac{1}{6}\frac{e}{k_B T}\sum_i r_i^2 k_i P_i$$

The charge-hopping probability (P_i) is given by

$$P_i = \frac{k_i}{\sum_i k_i}$$

Both NTN and NTNB display high electron mobility (Table 4.15). The calculated theoretical electron mobility was found to be greater for NTN (μ_e = 0.02 $cm^2V^{-1}s^{-1}$ vs μ_e = 0.01 $cm^2V^{-1}s^{-1}$ for NTNB). Despite NTNB having stronger electronic coupling than NTN, the mobility of NTN is higher. The difference lies in the molecular packing of crystalline NTN and NTNB. NTN has similar repeating slip stack dimers at an intermolecular distance of 5.0 Å, while NTNB has two types of dimers in the stacks, one at an intermolecular distance of 3.4 Å and two others at a higher intermolecular distance ($d_{\pi-\pi}$ = 9.3 Å and $d_{\pi-\pi}$ = 9.6 Å). Only the dimer with a lower intermolecular distance ($d_{\pi-\pi}$ = 3.4 Å) in NTNB contributes significantly to the mobility. RAHB dimers have a significant electron transfer integral in NTN. As a result, the effective contribution of the π–π

Table 4.14: The hole and electron reorganization energy of NTN and NTNB.

Molecule	Hole reorganization energy (eV)	Electron reorganization energy (eV)
NTN	0.62	0.43
NTNB	0.84	0.43

Table 4.15: The theoretically predicted hole and electron mobility of NTN and NTNB.

Molecule	Hole mobility, μ_h ($cm^2V^{-1}s^{-1}$)	Electron mobility, μ_e ($cm^2V^{-1}s^{-1}$)
NTN	0.0019	0.0189
NTNB	0.000057	0.0108

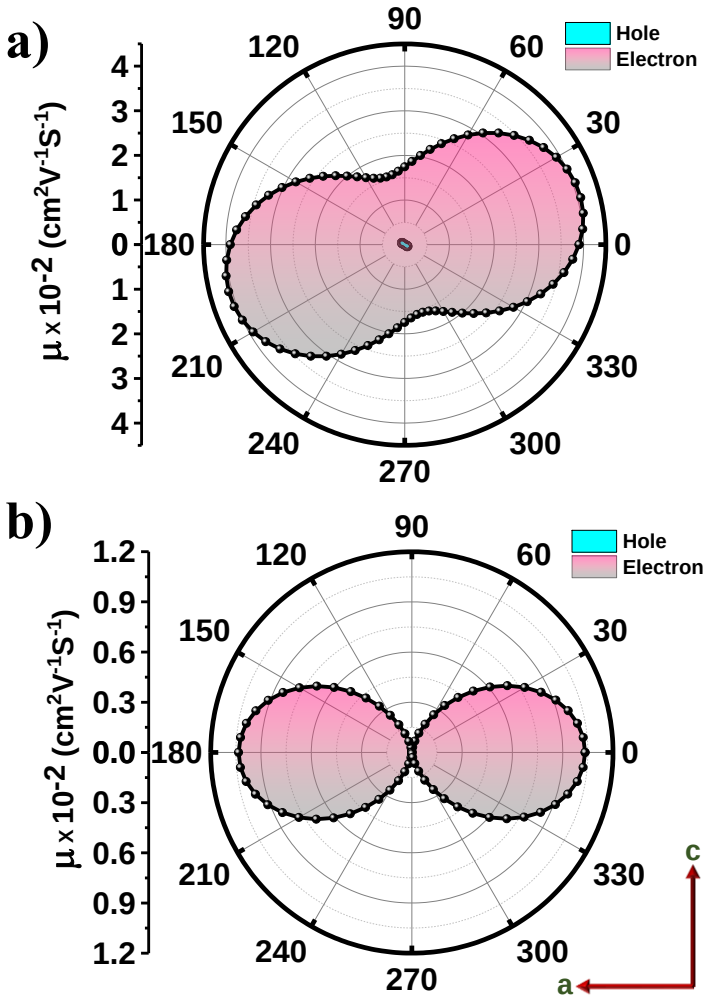

Figure 4.14: Anisotropic hole and electron mobilities of (a) NTN and (b) NTNB along the stacking plane. The crystallographic a axis is taken as the reference axis and is projected on the ac plane.

stacked dimers and RAHB dimers of NTN resulted in a higher mobility in comparison to NTNB. To understand the anisotropic mobility (μ_ϕ)[41] in the NT crystals. μ_ϕ is calculated as

$$\mu_\phi = \frac{e}{2k_BT}\sum_i k_i r_i^2 P_i \cos^2\gamma_i cos^2(\theta_i - \phi)$$

where γ_i is the angle between the charge-hopping pathway and the plane of interest (ac plane), ϕ is the orientation angle of the transport channel relative to the reference axis, and θ_i is the angle between the projected hopping paths of different dimers and the reference axis. Both NT crystals exhibit anisotropic hole and electron mobility distributions. The calculated anisotropic electron

mobility (Figure 4.14) of NTN reaches a maximum along the directions ϕ = 15° and 195°, in terms of molecular packing between π−π stacked (a axis) and hydrogen-bonded dimer directions. This gives us an idea of effective contribution of the RAHB dimer to the calculated charge transfer integral and charge carrier mobilities along the hydrogen-bonding direction. However, in the case of NTNB the highest electron and hole mobilities appear along the π−π stacking direction (a axis), as the contributions from hydrogen bonded dimers were comparatively less. The predictedanisotropic mobility suggests the contribution of RAHB to the charge transport, which has rarely been explored for the molecular design of organic semiconductors.[56]

4.3. Conclusions

In summary, we describe the novel angular naphthothiazoles NTN and NTNB, whose crystalline packing is primarily governed by RAHB and π−π stacking interactions. A dipole moment minimization in the RAHB dimer of crystalline NTs and antiparallel dimer of NTNB reinforces the role of electrostatic dipolar interactions in tailoring the solid-state packing. An aromaticity gain in the antiparallel NTNB dimer can offer a better roadmap for crystal engineering of π−π stacked organic molecules with aromatic stabilization. IQA calculations establish the stabilizing nature of RAHB with the major contribution stemming from electrostatics. The stabilization energies associated with a charge-transfer interaction between the lone pair of the nitrogen atom and the antibonding N−H orbital in RAHB were assessed using NBO calculations. Theoretical calculations employing the Marcus−Hush formalism and quantum chemical calculations in NTN reveal maximum hole and electron transfer couplings for RAHB and π−π stacked dimers, respectively. In contrast, NTNB displays higher hole and electron transfer couplings along the direction of the π−π stacked dimer. Crystal engineering can be exploited as an effective strategy to modulate the charge transport properties by achieving the precise control of π−π stacking and RAHB in π-conjugated molecules. The theoretically predicted high electron mobility in crystalline NT makes them potential candidates for the development of novel high-performance organic semiconductor devices.

4.4. Experimental Section

4.4.1. Synthesis of 4-methoxynaphthalen-1-amine (2)

1-methoxy-4-nitronapthalene (2.46 mmol) was dissolved in methanol and catalytic amount of Pd/C was added to the round bottom flask. The reaction mixture was purged with hydrogen and was stirred for 8 hours at room temperature. The reaction mixture was then extracted with dichloromethane. The crude mixture was used for the next reaction without further purification.

4.4.2. Synthesis of 5-methoxynaphtho[1,2-*d*]thiazol-2-amine (3)

Dissolved 4-ethoxynapthalen-1-amine (crude, 0.23 mmol) and potassium thiocyanate (0.46 mmol) in a round bottom flask charged with glacial acetic acid and stirred for 5 minutes. Then slowly added Br_2 (catalytic amount) and the reaction was stirred for 6 hours at room temperature. After confirming the full consumption of reactant, added 10ml of saturated sodium thiosulphate solution to quench the excess bromine in the reaction mixture. The organic compound was extracted using dichloromethane and was purified using silica gel column chromatography (petroleum ether: ethyl acetate = 3:1) to obtain compound 3 in 34 % yield.

M.p. = 225°C

^{1}H NMR (500 MHz, $CDCl_3$, ppm) δ = 8.35 (d, J = 8 Hz, 1H), 8.19 (d, J = 8.5 Hz, 1H), 7.50 (t, J = 8 Hz, 1H), 7.74 (t, J = 8 Hz, 1H), 6.96 (s, 1H), 5.13 (s, 2H), 3.94 (s, 3H).

^{13}C NMR (500 MHz, $CDCl_3$, ppm) δ = 166.3, 143.84, 134.69, 133.10, 128.14, 126.06, 124.94, 123.57, 122.60, 95.63, 55.95

HRMS (APCI) m/z calculated for $C_{12}H_{10}N_2OS$ [$(M+H)^+$]; 231.0514; found 231.0586.

4.4.3. Synthesis of 4-bromo-5-methoxynaphtho[1,2-*d*]thiazol-2-amine (4)

To a solution of 4-ethoxynapthalen-1-amine (crude, 0.23 mmol) in glacial acetic acid, potassium thiocyanate (0.46 mmol) and excess of bromine were added. The reaction mixture was stirred overnight at room temperature. After confirming the complete consumption of reactant, saturated solution of sodium thiosulphate was added to quench the excess bromine. The mixture was further separated and purified employing silica gel column chromatography using a mixture of petroleum ether and ethyl acetate (99:1) and light pink solid material was obtained with a yield of 46%.

M.p. = 231°C

^{1}H NMR (500 MHz, $CDCl_3$, ppm) δ = 8.37 (d, J = 8 Hz, 1H), 8.06 (d, J = 8 Hz, 1H), 7.50 (m, J = 28.5 Hz, 2H), 5.24 (s, 2H), 3.94 (s, 3H)

^{13}C NMR (500 MHz, $CDCl_3$, ppm) δ = 164.15, 147.97, 128.12, 126.34, 125.69, 125.62, 125.20, 123.20, 121.43, 103.27, 60.92.

HRMS (APCI) m/z calculated for $C_{12}H_9BrN_2OS$; 309.1810; found 309.9660.

4.5 Appendix

4.5.1: Materials and Methods

Same as discussed in section 2.6.1 (Chapter 2)

4.5.2: Dissected nucleus-independent chemical shifts:[45,46] $NICS_{zz}$ (1) were calculated at ωB97XD/Def2-TZVP level of theory using Gauge Including Atomic Orbital (GIAO) method at 1 Å above the centroid of each ring of the monomer and dimer using Gaussian 16 software. The local contributions from the sigma framework (orbitals) have minimal impact on $NICS_{zz}$(1). Negative NICS value indicates diatropic current or aromaticity as NICS value corresponds to the negative of magnetic shielding and vice versa. The aromaticity variation of monomers upon RAHB and π-π stacking was assessed using $NICS_{zz}$(1).

4.5.3: Natural bond orbital analyses:[57,58] The natural bond orbital (NBO) analyses was performed at the ωB97XD/Def2-TZVP level of theory, by means of the Gaussian 16 calculation package. The orbital donor-acceptor interactions are assessed by probing all possible interactions between occupied (donor) Lewis-type NBOs and unoccupied (acceptor) non-Lewis NBOs by second-order perturbation theory. For each donor NBO (i) and acceptor NBO (j), the stabilization energy E(2) associated with delocalization from the filled NBOs into the unoccupied non-Lewis orbitals is estimated.

4.6. REFERENCES

(1) Anthony, J. E. Functionalized Acenes and Heteroacenes for Organic Electronics. *Chemical Reviews* **2006**, *106*, 5028–5048.

(2) Sirringhaus, H.; Brown, P. J.; Friend, R. H.; Nielsen, M. M.; Bechgaard, K.; Langeveld-Voss, B. M. W.; Spiering, A. J. H.; Janssen, R. A. J.; Meijer, E. W.; Herwig, P.; de Leeuw, D. M. Two-Dimensional Charge Transport in Self-Organized, High-Mobility Conjugated Polymers. *Nature* **1999**, *401*, 685–688.

(3) Sariciftci, N. S.; Smilowitz, L.; Heeger, A. J.; Wudl, F. Photoinduced Electron Transfer from a Conducting Polymer to Buckminsterfullerene. *Science* **1992**, *258*, 1474–1476.

(4) Burroughes, J. H.; Bradley, D. D. C.; Brown, A. R.; Marks, R. N.; Mackay, K.; Friend, R. H.; Burns, P. L.; Holmes, A. B. Light-Emitting Diodes Based on Conjugated Polymers. *Nature* **1990**, *347*, 539–541.

(5) Bässler, H.; Köhler, A. Charge Transport in Organic Semiconductors. In *Topics in Current Chemistry*; 2011; Vol. 312, pp 1–65.

(6) Feng, X.; Marcon, V.; Pisula, W.; Hansen, M. R.; Kirkpatrick, J.; Grozema, F.; Andrienko, D.; Kremer, K.; Müllen, K. Towards High Charge-Carrier Mobilities by Rational Design of the Shape and Periphery of Discotics. *Nature Materials* **2009**, *8*, 421–426.

(7) Dong, H.; Fu, X.; Liu, J.; Wang, Z.; Hu, W. 25th Anniversary Article: Key Points for High-Mobility Organic Field-Effect Transistors. *Advanced Materials* **2013**, *25*, 6158–6183.

(8) Minemawari, H.; Tanaka, M.; Tsuzuki, S.; Inoue, S.; Yamada, T.; Kumai, R.; Shimoi, Y.; Hasegawa, T. Enhanced Layered-Herringbone Packing Due to Long Alkyl Chain Substitution in Solution-Processable Organic Semiconductors. *Chemistry of Materials* **2017**, *29*, 1245–1254.

(9) Mei, J.; Diao, Y.; Appleton, A. L.; Fang, L.; Bao, Z. Integrated Materials Design of Organic Semiconductors for Field-Effect Transistors. *Journal of the American Chemical Society* **2013**, *135*, 6724–6746.

(10) Gsänger, M.; Oh, J. H.; Könemann, M.; Höffken, H. W.; Krause, A. M.; Bao, Z.; Würthner, F. A Crystal-Engineered Hydrogen-Bonded Octachloroperylene Diimide with a Twisted Core: An n-Channel Organic Semiconductor. *Angewandte Chemie International Edition* **2010**, *49*, 740–743.

(11) Dong, H.; Wang, C.; Hu, W. High Performance Organic Semiconductors for Field-Effect Transistors. *Chemical Communications* **2010**, *46*, 5211.

(12) Yao, Z. F.; Wang, J. Y.; Pei, J. Control of π-π Stacking via Crystal Engineering in Organic Conjugated Small Molecule Crystals. *Crystal Growth and Design* **2018**, *18*, 7–15.

(13) Głowacki, E. D.; Irimia-Vladu, M.; Bauer, S.; Sariciftci, N. S. Hydrogen-Bonds in Molecular Solids – from Biological Systems to Organic Electronics. *Journal of Materials Chemistry B* **2013**, *1*, 3742–3753.

(14) Gilli, G.; Bellucci, F.; Ferretti, V.; Bertolasi, V. Evidence for Resonance-Assisted Hydrogen Bonding from Crystal-Structure Correlations on the Enol Form of the .Beta.-Diketone Fragment. *Journal of the American Chemical Society* **1989**, *111*, 1023–1028.

(15) Bertolasi, V.; Gilli, P.; Ferretti, V.; Gilli, G. Evidence for Resonance-Assisted Hydrogen Bonding. 2. Intercorrelation between Crystal Structure and Spectroscopic Parameters in Eight Intramolecularly Hydrogen Bonded 1,3-Diaryl-1,3-Propanedione Enols. *Journal of the American Chemical Society* **1991**, *113*, 4917–4925.

(16) Saez Talens, V.; Davis, J.; Wu, C.-H.; Wen, Z.; Lauria, F.; Gupta, K. B. S. S.; Rudge, R.; Boraghi, M.; Hagemeijer, A.; Trinh, T. T.; Englebienne, P.; Voets, I. K.; Wu, J. I.; Kieltyka, R. E. Thiosquaramide-Based Supramolecular Polymers: Aromaticity Gain in a Switched Mode of Self-Assembly. *Journal of the American Chemical Society* **2020**, *142*, 19907–19916.

(17) Rahmani, M.; Salimi, A.; Mohammadzadeh, S.; Sparkes, H. A. The Supramolecular Effect of Aromaticity on the Crystal Packing of Furan/Thiophene Carboxamide Compounds. *CrystEngComm* **2016**, *18*, 8953–8960.

(18) Kakeshpour, T.; Wu, J. I.; Jackson, J. E. AMHB: (Anti)Aromaticity-Modulated Hydrogen

Bonding. *Journal of the American Chemical Society* **2016**, *138*, 3427–3432.

(19) Wen, Z.; Wu, J. I. C. Antiaromaticity Gain Increases the Potential for N-Type Charge Transport in Hydrogen-Bonded π-Conjugated Cores. *Chemical Communications* **2020**, *56*, 2008–2011.

(20) Yin, X.; Zang, Y.; Zhu, L.; Low, J. Z.; Liu, Z. F.; Cui, J.; Neaton, J. B.; Venkataraman, L.; Campos, L. M. A Reversible Single-Molecule Switch Based on Activated Antiaromaticity. *Science Advances* **2017**, *3*, 1–6.

(21) Maksić, Z. B.; Glasovac, Z.; Despotović, I. Predicted High Proton Affinity of Poly-2,5-Dihydropyrrolimines - The Aromatic Domino Effect. *Journal of Physical Organic Chemistry* **2002**, *15*, 499–508.

(22) Kelley, S. O.; Jackson, N. M.; Hill, M. G.; Barton, J. K. Long-Range Electron Transfer through DNA Films. *Angewandte Chemie - International Edition* **1999**, *38*, 941–945.

(23) Sontz, P. A.; Muren, N. B.; Barton, J. K. DNA Charge Transport for Sensing and Signaling. *Accounts of Chemical Research* **2012**, *45*, 1792–1800.

(24) Guo, X.; Gorodetsky, A. A.; Hone, J.; Barton, J. K.; Nuckolls, C. Conductivity of a Single DNA Duplex Bridging a Carbon Nanotube Gap. *Nature Nanotechnology* **2008**, *3*, 163–167.

(25) Kulikov, V.; Johnson, N. A. B.; Surman, A. J.; Hutin, M.; Kelly, S. M.; Hezwani, M.; Long, D. L.; Meyer, G.; Cronin, L. Spontaneous Assembly of an Organic–Inorganic Nucleic Acid Z-DNA Double-Helix Structure. *Angewandte Chemie (International Ed. in English)* **2017**, *56*, 1141.

(26) Van Hecke, K.; Cardinaels, T.; Nockemann, P.; Jacobs, J.; Vanpraet, L.; Parac-Vogt, T. N.; Van Deun, R.; Binnemans, K.; Van Meervelt, L. Enantioselective Assembly of a Ruthenium(II) Polypyridyl Complex into a Double Helix. *Angewandte Chemie (International ed. in English)* **2014**, *53*, 8959–8962.

(27) Ellena, J.; Bocelli, M. D.; Honorato, S. B.; Ayala, A. P.; Doriguetto, A. C.; Martins, F. T. Base-Paired and Base-Stacked Structures of the Anti-HIV Drug Lamivudine: A Nucleoside DNA-Mimicry with Unprecedented Topology. *Crystal Growth and Design* **2012**, *12*, 5138–

5147.

(28) Ai, Q.; Getmanenko, Y. A.; Jarolimek, K.; Castañeda, R.; Timofeeva, T. V.; Risko, C. Unusual Electronic Structure of the Donor–Acceptor Cocrystal Formed by Dithieno[3,2-a :2′,3′- c]Phenazine and 7,7,8,8-Tetracyanoquinodimethane. *The Journal of Physical Chemistry Letters* **2017**, *8*, 4510–4515.

(29) Yee, N.; Dadvand, A.; Hamzehpoor, E.; Titi, H. M.; Perepichka, D. F. Hydrogen Bonding Versus π-Stacking in Charge-Transfer Co-Crystals. *Crystal Growth & Design* **2021**, *21*, 2609–2613.

(30) Lin, Y.; Fan, H.; Li, Y.; Zhan, X. Thiazole-Based Organic Semiconductors for Organic Electronics. *Advanced Materials* **2012**, *24*, 3087–3106.

(31) Yan, L.; Popescu, F.; Rao, M. R.; Meng, H.; Perepichka, D. F. A Wide Band Gap Naphthalene Semiconductor for Thin-Film Transistors. *Advanced Electronic Materials* **2017**, *3*, 1–8.

(32) de Toledo, J. S.; Junior, P. E. S.; Manfrim, V.; Pinzan, C. F.; de Araujo, A. S.; Cruz, A. K.; Emery, F. S. Synthesis, Cytotoxicity and in Vitro Antileishmanial Activity of Naphthothiazoles. *Chemical Biology and Drug Design* **2013**, *81*, 749–756.

(33) Ramakrishnan, R.; Niyas, M. A.; Lijina, M. P.; Hariharan, M. Distinct Crystalline Aromatic Structural Motifs: Identification, Classification, and Implications. *Accounts of Chemical Research* **2019**, *52*, 3075–3086.

(34) Niyas, M. A.; Ramakrishnan, R.; Vijay, V.; Sebastian, E.; Hariharan, M. Anomalous Halogen–Halogen Interaction Assists Radial Chromophoric Assembly. *Journal of the American Chemical Society* **2019**, *141*, 4536–4540.

(35) Vijay, V.; Ramakrishnan, R.; Hariharan, M. Halogen–Halogen Bonded Donor-Acceptor Stacks Foster Orthogonal Electron and Hole Transport. *Crystal Growth & Design* **2021**, *21*, 200–206.

(36) John, A. T.; Narayanasamy, A.; George, D.; Hariharan, M. Atom-Efficient Halogen-Halogen Interactions Assist One-, Two-, and Three-Dimensional Molecular Zippers.

Journal of Physical Chemistry C **2021**, *125*, 10716–10722.

(37) John, A. T.; Narayanasamy, A.; George, D.; Hariharan, M. The Effect of Single-Atom Substitution on Structure and Band Gap in Organic Semiconductors. *Crystal Growth and Design* **2022**, *22*, 1237–1243.

(38) Gilli, G.; Bertolasi, V.; Ferretti, V.; Gilli, P. Resonance-Assisted Hydrogen Bonding. III. Formation of Intermolecular Hydrogen-Bonded Chains in Crystals of β-Diketone Enols and Its Relevance to Molecular Association. *urn:issn:0108-7681* **1993**, *49*, 564–576.

(39) Guevara-Vela, J. M.; Romero-Montalvo, E.; Costales, A.; Pendás, Á. M.; Rocha-Rinza, T. The Nature of Resonance-Assisted Hydrogen Bonds: A Quantum Chemical Topology Perspective. *Physical Chemistry Chemical Physics* **2016**, *18*, 26383–26390.

(40) Szalewicz, K. Symmetry-Adapted Perturbation Theory of Intermolecular Forces. *Wiley Interdisciplinary Reviews: Computational Molecular Science* **2012**, *2*, 254–272.

(41) Etter, M. C. Encoding and Decoding Hydrogen-Bond Patterns of Organic Compounds. *Accounts of Chemical Research* **1990**, *23*, 120–126.

(42) Spackman, M. A.; Jayatilaka, D. Hirshfeld Surface Analysis. *CrystEngComm* **2009**, *11*, 19–32.

(43) Desiraju, G. R.; Gavezzotti, A. Crystal Structures of Polynuclear Aromatic Hydrocarbons. Classification, Rationalization and Prediction from Molecular Structure. *Acta Crystallographica Section B Structural Science* **1989**, *45*, 473–482.

(44) Dey, A.; Desiraju, G. R. Correlation between Molecular Dipole Moment and Centrosymmetry in Some Crystalline Diphenyl Ethers. *Chemical Communications* **2005**, No. 19, 2486.

(45) Schleyer, P. von R.; Manoharan, M.; Wang, Z.-X.; Kiran, B.; Jiao, H.; Puchta, R.; van Eikema Hommes, N. J. R. Dissected Nucleus-Independent Chemical Shift Analysis of π-Aromaticity and Antiaromaticity. *Organic Letters* **2001**, *3*, 2465–2468.

(46) Fallah-Bagher-Shaidaei, H.; Wannere, C. S.; Corminboeuf, C.; Puchta, R.; Schleyer, P. v.

R. Which NICS Aromaticity Index for Planar π Rings Is Best? *Organic Letters* **2006**, *8*, 863–866.

(47) Reed, A. E.; Curtiss, L. A.; Weinhold, F. Intermolecular Interactions from a Natural Bond Orbital, Donor—Acceptor Viewpoint. *Chemical Reviews* **1988**, *88*, 899–926.

(48) Coropceanu, V.; Cornil, J.; da Silva Filho, D. A.; Olivier, Y.; Silbey, R.; Brédas, J.-L. Charge Transport in Organic Semiconductors. *Chemical Reviews* **2007**, *107*, 926–952.

(49) GitHub - google/catnip: Catnip Sandbox https://github.com/google/catnip (accessed Apr 18, 2022).

(50) Troisi, A. Charge Transport in High Mobility Molecular Semiconductors: Classical Models and New Theories. *Chemical Society Reviews* **2011**, *40*, 2347–2358.

(51) McMahon, D. P.; Troisi, A. Evaluation of the External Reorganization Energy of Polyacenes. *Journal of Physical Chemistry Letters* **2010**, *1*, 941–946.

(52) Norton, J. E.; Brédas, J. L. Polarization Energies in Oligoacene Semiconductor Crystals. *Journal of the American Chemical Society* **2008**, *130*, 12377–12384.

(53) Giannini, S.; Carof, A.; Blumberger, J. Crossover from Hopping to Band-Like Charge Transport in an Organic Semiconductor Model: Atomistic Nonadiabatic Molecular Dynamics Simulation. *Journal of Physical Chemistry Letters* **2018**, *9*, 3116–3123.

(54) Deng, W. Q.; Goddard, W. A. Predictions of Hole Mobilities in Oligoacene Organic Semiconductors from Quantum Mechanical Calculations. *Journal of Physical Chemistry B* **2004**, *108*, 8614–8621.

(55) Kalita, K. J.; Giri, I.; Vijayaraghavan, R. K. Influence of Non-Covalent Interactions in Dictating the Polarity and Mobility of Charge Carriers in a Series of Crystalline NDIs: A Computational Case Study. *RSC Advances* **2021**, *11*, 33703–33713.

(56) Zhang, F.; Lemaur, V.; Choi, W.; Kafle, P.; Seki, S.; Cornil, J.; Beljonne, D.; Diao, Y. Repurposing DNA-Binding Agents as H-Bonded Organic Semiconductors. *Nature Communications* **2019**, *10*, 1–11.

(57) Weinhold, F. Natural Bond Orbital Analysis: A Critical Overview of Relationships to Alternative Bonding Perspectives. *Journal of Computational Chemistry* **2012**, *33*, 2363–2379.

(58) Reed, A. E.; Curtiss, L. A.; Weinhold, F. Intermolecular Interactions from a Natural Bond Orbital, Donor-Acceptor Viewpoint. *Chemical Reviews* **1988**, *88*, 899–926.

5. List of Publications

1. Access to Triplet Excited States of Organic Chromophores, Devika Sasikumar[‡], **Athira T. John[†],** Jeswin Sunny and Mahesh Hariharan Chem. Soc. Rev. **2020**, *49*, 6122-6140. **(Inside Front Cover).**
2. Atom-Efficient Halogen–Halogen Interactions Assist One-, Two-, and Three-Dimensional Molecular Zippers, **Athira T. John**, Akshaya Narayanasamy, Deepu George, and Mahesh Hariharan*, *J. Phys. Chem. C* **2021***, 125,* 10716−10722. **(Front Cover) (Virtual Special Issue "D. D. Sarma Festschrift").**
3. The Effect of Single-Atom Substitution on Structure and Band Gap in Organic Semiconductors, **Athira T. John,**[†] Akshaya Narayanasamy,[†] Deepu George, and Mahesh Hariharan***** *Cryst. Growth Des.* **2022**, *22*, 1237−1243.
4. Resonance-Assisted Hydrogen Bonding and π−π Stacking Modulates the Charge Transfer Coupling in Crystalline Naphthothiazoles, **Athira T. John**, Akshaya Narayanasamy, Keerthy P. Sudhakaran, and Mahesh Hariharan*, *Cryst. Growth Des.* **2022***, 22,* 5686-5693. **(Virtual Special Issue on Non-Covalent Interactions: Celebrating Prof. Guru Row).**
5. Deciphering the Role of (Anti)Aromaticity in Cofacial Excimers of Linear Acenes, Akhilesh Krishnan,[†,‡] Aitor Diaz-Andres,[†,ǁ] Keerthy P. Sudhakaran,[‡] **Athira T. John**,[‡] Mahesh Hariharan,[*,‡] David Casanova[*,ǁ,#] (under revision).
6. Charge Transport Through Discrete Crystalline Archetectures, **Athira T. John**, Deepu George and Mahesh Hariaharan* (Under preparation).
7. Tweaking Antiaromaticity of Pentalene on Grphene Fragment, Keerthy P. Sudakaran, Alfy benny, **Athira T. John** and Mahesh Hariharan* (Under preparation).
8. Competition Between Vibronic Coupling and Heavy Atom Induced Triplet Excited State Population in Terrylenediimide, **Athira T. John**, Suvarna Sujilkumar C., and Mahesh Hariharan* (under preparation).

†=These authors contributed equally.

6. Workshops and Conferences

- **3rd Indian Materials Conclave and 32nd Annual meeting of MRSI Research Society of India Conference 2021** | 17th -23rd Dec, 2021| Indian Institute of Technology Madras, Virtual Symposium |.
- **12th National Workshop on Fluorescence and Raman Spectroscopy (FCS 2021)** | 29th Nov - 4th Dec, 2021| Virtual Symposium|.
- **Light-Matter Interactions from Scratch; Theory and Experiments at the Border with Biology** | ICTP | 22nd – 25th Nov, 2021| Virtual Symposium|.
- Virtual Chemistry Course "**Functional Pi-Systems– Organic Materials Design by Molecular and Supramolecular Engineering.**" |19th-23rd Jul, 2021| University of Würzburg |.
- **International Conference on Ultrafast Spectroscopy (ICUS2020)** | 21st-22nd Feb, 2020 | IISER TVM, Kerala, India |.
- **IISERTVM-RSC Symposium on Advances in Chemical Sciences** | 4th Feb, 2020 | IISER TVM, Kerala, India|
- **National workshop on single molecule fluorescence (FCS 2019)** | 16th – 21st Dec, 2019| TIFR Hyderabd, India|.
- **Faraday Discussions (2018): Photoinduced Processes in Nucleic Acids and Proteins** | 11th-13th Jan, 2018 Thiruvananthapuram, Kerala, India|.
- **Nanobioteck-2017: 2nd Annual Conference of Indian Society of Nanomedicine** | 6th-8th Dec, 2017 | Thiruvananthapuram, Kerala, India|.
- **8th East Asia Symposium on Functional Dyes and Advanced Materials** | 20th-22nd Sep, 2017| Council of Scientific and Industrial Research -National Institute for Interdisciplinary Science and Technology (CSIR-NIIST) Thiruvananthapuram, Kerala, India |.
- **Workshop for scientific writing** organized by Taylor and Francis group| September 2015| |IISER Mohali|.
- **National Seminar on Crystallography (43A)** |March 28-30, 2014)| |IISER Mohali|.

7. Copyrights and Permissions

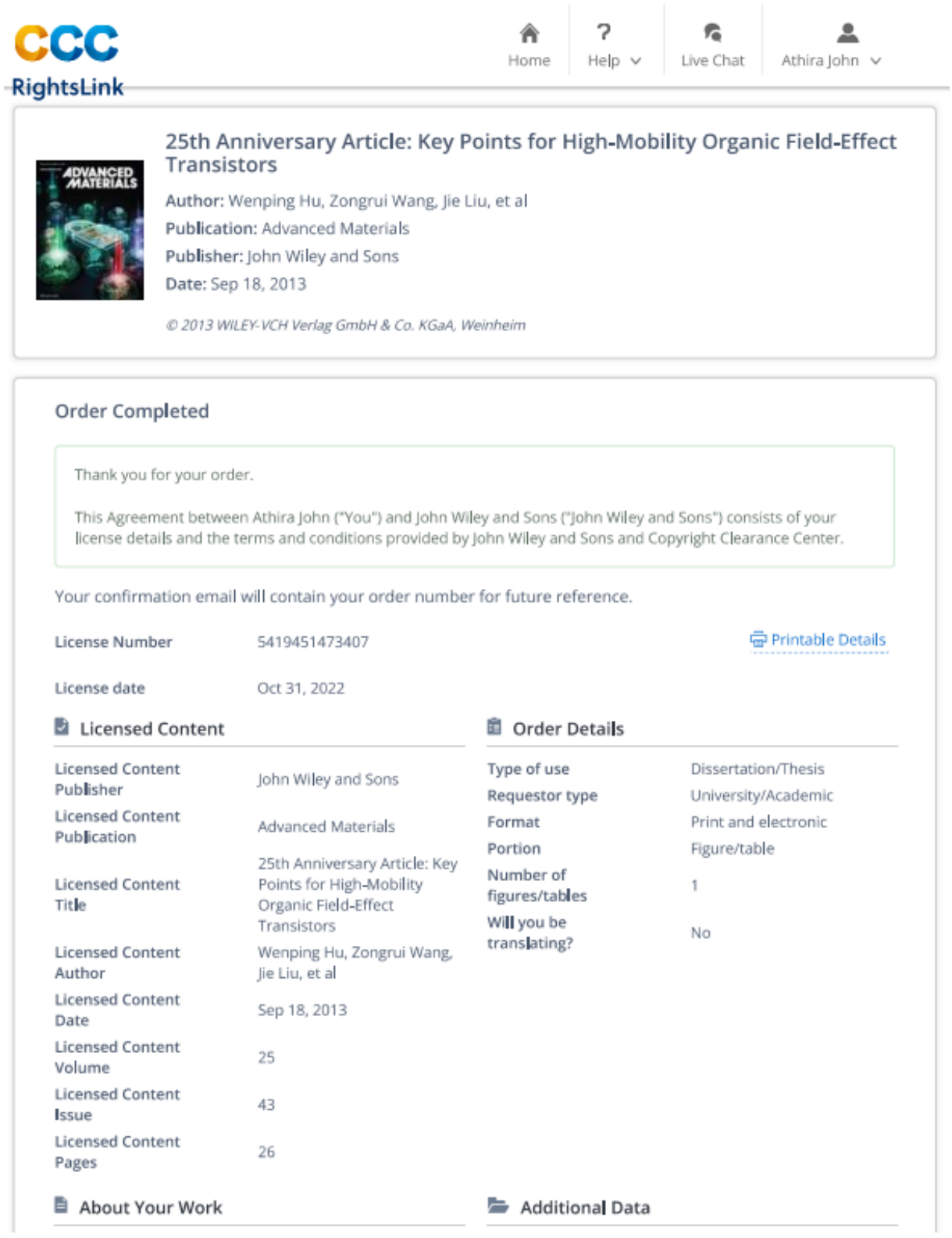

CCC RightsLink

Home | Help | Live Chat | Athira John

25th Anniversary Article: Key Points for High-Mobility Organic Field-Effect Transistors

Author: Wenping Hu, Zongrui Wang, Jie Liu, et al
Publication: Advanced Materials
Publisher: John Wiley and Sons
Date: Sep 18, 2013

© 2013 WILEY-VCH Verlag GmbH & Co. KGaA, Weinheim

Order Completed

Thank you for your order.

This Agreement between Athira John ("You") and John Wiley and Sons ("John Wiley and Sons") consists of your license details and the terms and conditions provided by John Wiley and Sons and Copyright Clearance Center.

Your confirmation email will contain your order number for future reference.

Printable Details

License Number	5419451473407
License date	Oct 31, 2022

Licensed Content

Licensed Content Publisher	John Wiley and Sons
Licensed Content Publication	Advanced Materials
Licensed Content Title	25th Anniversary Article: Key Points for High-Mobility Organic Field-Effect Transistors
Licensed Content Author	Wenping Hu, Zongrui Wang, Jie Liu, et al
Licensed Content Date	Sep 18, 2013
Licensed Content Volume	25
Licensed Content Issue	43
Licensed Content Pages	26

Order Details

Type of use	Dissertation/Thesis
Requestor type	University/Academic
Format	Print and electronic
Portion	Figure/table
Number of figures/tables	1
Will you be translating?	No

About Your Work

Additional Data

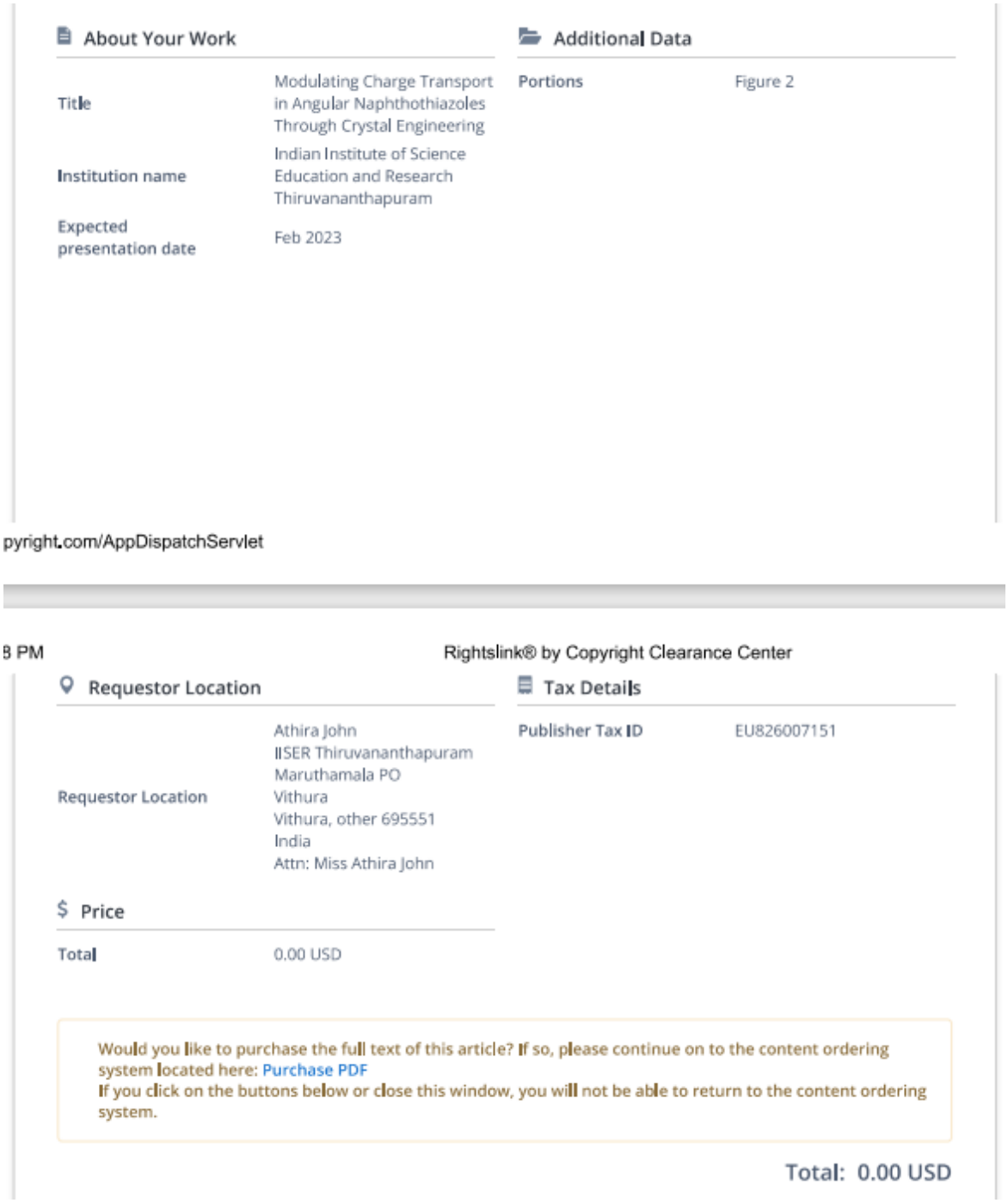

About Your Work

Title	Modulating Charge Transport in Angular Naphthothiazoles Through Crystal Engineering
Institution name	Indian Institute of Science Education and Research Thiruvananthapuram
Expected presentation date	Feb 2023

Additional Data

Portions	Figure 2

pyright.com/AppDispatchServlet

8 PM Rightslink® by Copyright Clearance Center

Requestor Location

Requestor Location	Athira John IISER Thiruvananthapuram Maruthamala PO Vithura Vithura, other 695551 India Attn: Miss Athira John

Tax Details

Publisher Tax ID	EU826007151

Price

Total	0.00 USD

Would you like to purchase the full text of this article? If so, please continue on to the content ordering system located here: Purchase PDF
If you click on the buttons below or close this window, you will not be able to return to the content ordering system.

Total: 0.00 USD

CCC RightsLink

Home | Help | Live Chat | Athira John

Non-Equal Ratio Cocrystal Engineering to Improve Charge Transport Characteristics of Organic Semiconductors: A Case Study on Indolo[2,3-a]carbazole

Author: Junfeng Guo, Yan Zeng, Yonggang Zhen, et al
Publication: Angewandte Chemie International Edition
Publisher: John Wiley and Sons
Date: May 17, 2022

Order Completed

Thank you for your order.

This Agreement between Athira John ("You") and John Wiley and Sons ("John Wiley and Sons") consists of your license details and the terms and conditions provided by John Wiley and Sons and Copyright Clearance Center.

Your confirmation email will contain your order number for future reference.

License Number	5419451276005
License date	Oct 31, 2022

Printable Details

Licensed Content

Licensed Content Publisher	John Wiley and Sons
Licensed Content Publication	Angewandte Chemie International Edition
Licensed Content Title	Non-Equal Ratio Cocrystal Engineering to Improve Charge Transport Characteristics of Organic Semiconductors: A Case Study on Indolo[2,3-a]carbazole
Licensed Content Author	Junfeng Guo, Yan Zeng, Yonggang Zhen, et al
Licensed Content Date	May 17, 2022
Licensed Content Volume	61
Licensed Content Issue	28
Licensed Content Pages	6

Order Details

Type of use	Dissertation/Thesis
Requestor type	University/Academic
Format	Print and electronic
Portion	Figure/table
Number of figures/tables	1
Will you be translating?	No

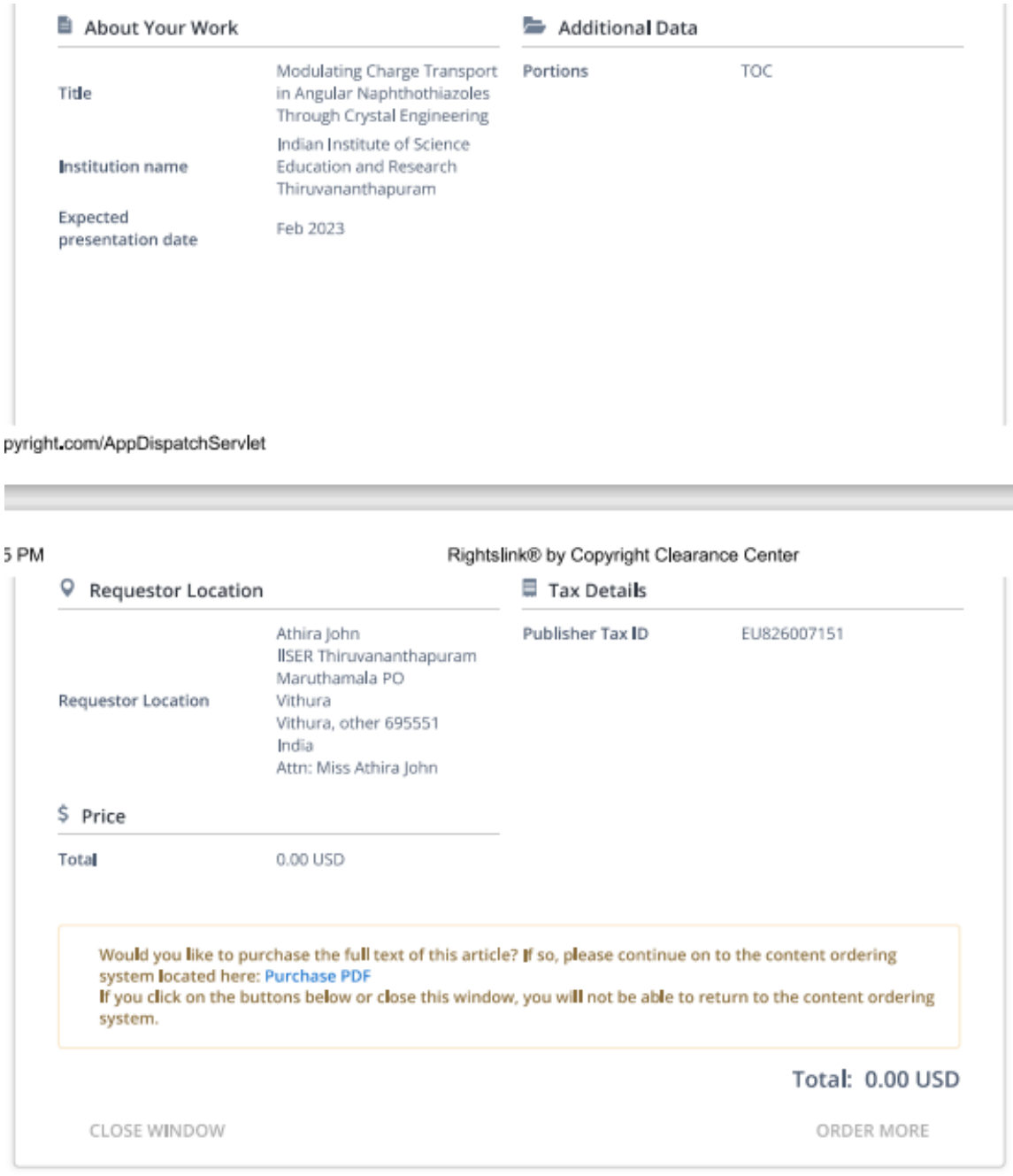

About Your Work

Title	Modulating Charge Transport in Angular Naphthothiazoles Through Crystal Engineering
Institution name	Indian Institute of Science Education and Research Thiruvananthapuram
Expected presentation date	Feb 2023

Additional Data

Portions	TOC

pyright.com/AppDispatchServlet

5 PM Rightslink® by Copyright Clearance Center

Requestor Location

Requestor Location	Athira John IISER Thiruvananthapuram Maruthamala PO Vithura Vithura, other 695551 India Attn: Miss Athira John

Tax Details

Publisher Tax ID	EU826007151

$ Price

Total	0.00 USD

Would you like to purchase the full text of this article? If so, please continue on to the content ordering system located here: Purchase PDF
If you click on the buttons below or close this window, you will not be able to return to the content ordering system.

Total: 0.00 USD

CLOSE WINDOW ORDER MORE

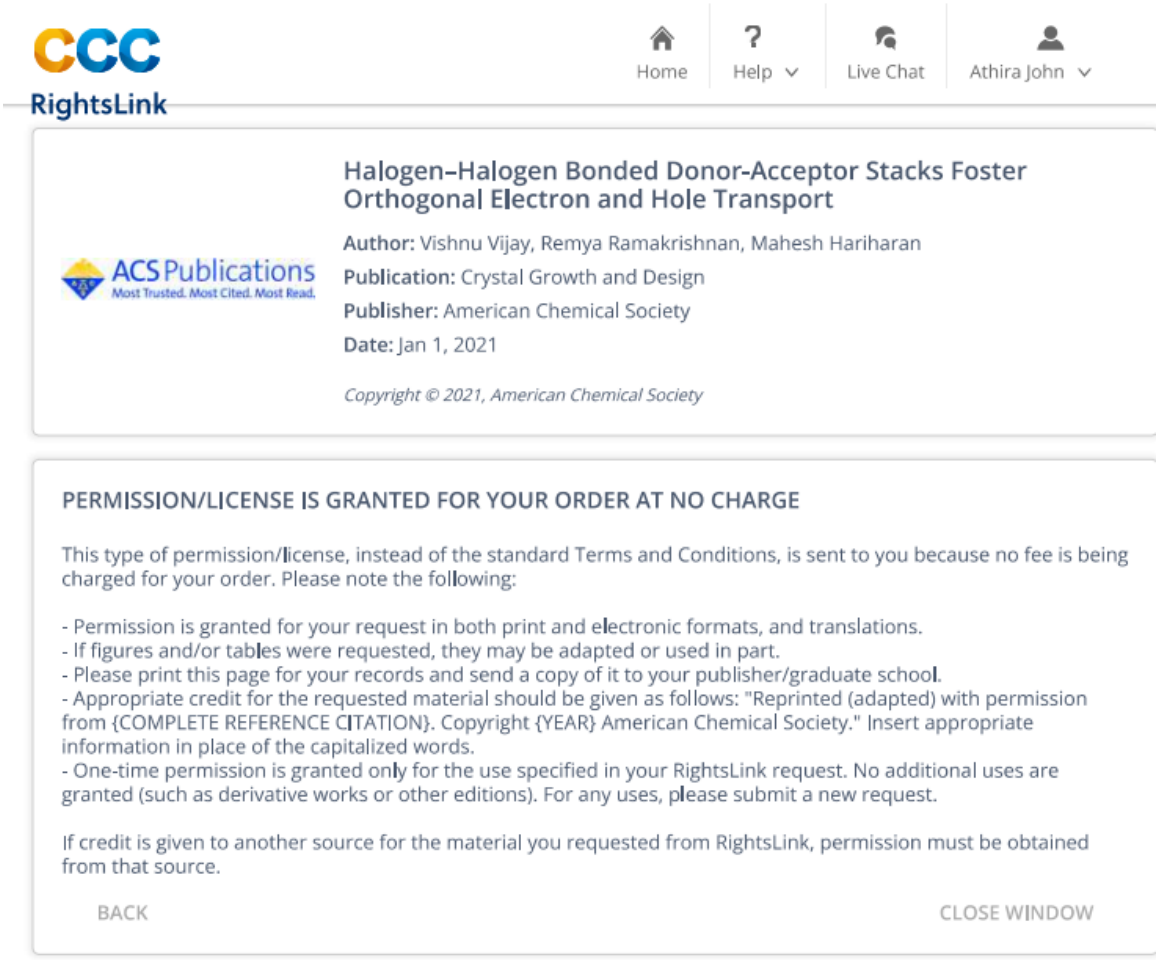

CCC RightsLink

Home | Help | Live Chat | Athira John

ACS Publications
Most Trusted. Most Cited. Most Read.

Halogen–Halogen Bonded Donor-Acceptor Stacks Foster Orthogonal Electron and Hole Transport

Author: Vishnu Vijay, Remya Ramakrishnan, Mahesh Hariharan
Publication: Crystal Growth and Design
Publisher: American Chemical Society
Date: Jan 1, 2021

Copyright © 2021, American Chemical Society

PERMISSION/LICENSE IS GRANTED FOR YOUR ORDER AT NO CHARGE

This type of permission/license, instead of the standard Terms and Conditions, is sent to you because no fee is being charged for your order. Please note the following:

- Permission is granted for your request in both print and electronic formats, and translations.
- If figures and/or tables were requested, they may be adapted or used in part.
- Please print this page for your records and send a copy of it to your publisher/graduate school.
- Appropriate credit for the requested material should be given as follows: "Reprinted (adapted) with permission from {COMPLETE REFERENCE CITATION}. Copyright {YEAR} American Chemical Society." Insert appropriate information in place of the capitalized words.
- One-time permission is granted only for the use specified in your RightsLink request. No additional uses are granted (such as derivative works or other editions). For any uses, please submit a new request.

If credit is given to another source for the material you requested from RightsLink, permission must be obtained from that source.

BACK CLOSE WINDOW

Null Exciton Splitting in Chromophoric Greek Cross ( ) Aggregate

Author: Mahesh Hariharan, Alfy Benny, Abbey M. Philip, et al
Publication: Angewandte Chemie International Edition
Publisher: John Wiley and Sons
Date: Nov 7, 2018

Order Completed

Thank you for your order.

This Agreement between Athira John ("You") and John Wiley and Sons ("John Wiley and Sons") consists of your license details and the terms and conditions provided by John Wiley and Sons and Copyright Clearance Center.

Your confirmation email will contain your order number for future reference.

License Number	5419450665978
License date	Oct 31, 2022

Printable Details

Licensed Content

Licensed Content Publisher	John Wiley and Sons
Licensed Content Publication	Angewandte Chemie International Edition
Licensed Content Title	Null Exciton Splitting in Chromophoric Greek Cross ( ) Aggregate
Licensed Content Author	Mahesh Hariharan, Alfy Benny, Abbey M. Philip, et al
Licensed Content Date	Nov 7, 2018
Licensed Content Volume	57
Licensed Content Issue	48
Licensed Content Pages	6

Order Details

Type of use	Dissertation/Thesis
Requestor type	University/Academic
Format	Print and electronic
Portion	Figure/table
Number of figures/tables	2
Will you be translating?	No

About Your Work

Title	Modulating Charge Transport in Angular Naphthothiazoles Through Crystal Engineering
Institution name	Indian Institute of Science Education and Research Thiruvananthapuram
Expected presentation date	Feb 2023

Additional Data

Portions	Figure 1, Figure 3

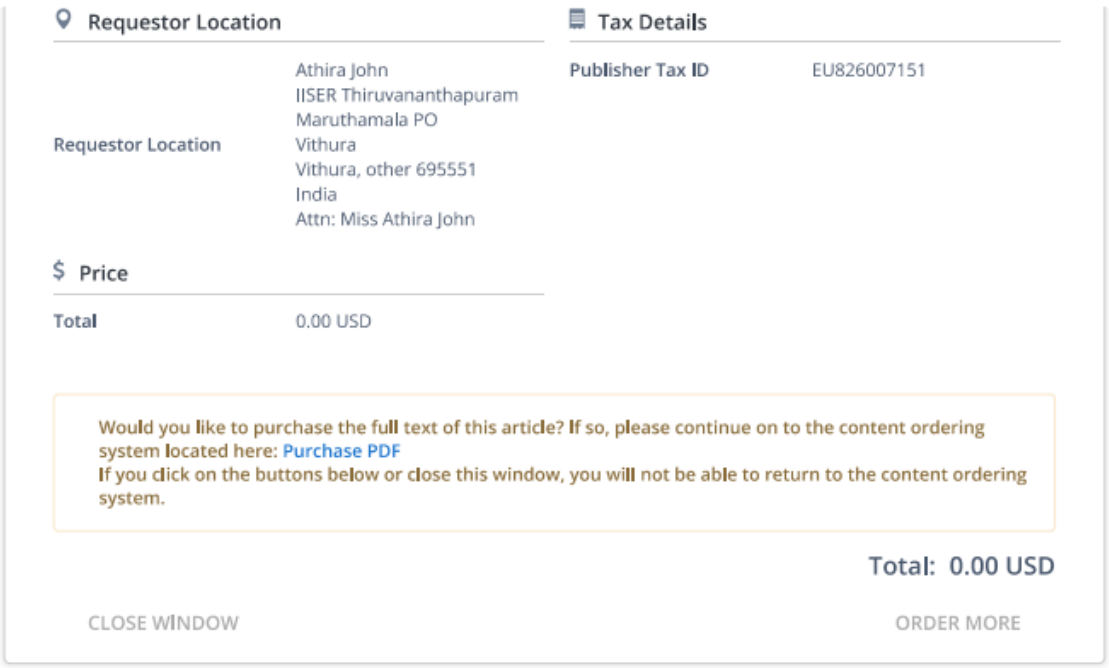

Requestor Location

Requestor Location	Athira John IISER Thiruvananthapuram Maruthamala PO Vithura Vithura, other 695551 India Attn: Miss Athira John

Tax Details

Publisher Tax ID	EU826007151

Price

Total	0.00 USD

Would you like to purchase the full text of this article? If so, please continue on to the content ordering system located here: Purchase PDF
If you click on the buttons below or close this window, you will not be able to return to the content ordering system.

Total: 0.00 USD

CLOSE WINDOW ORDER MORE

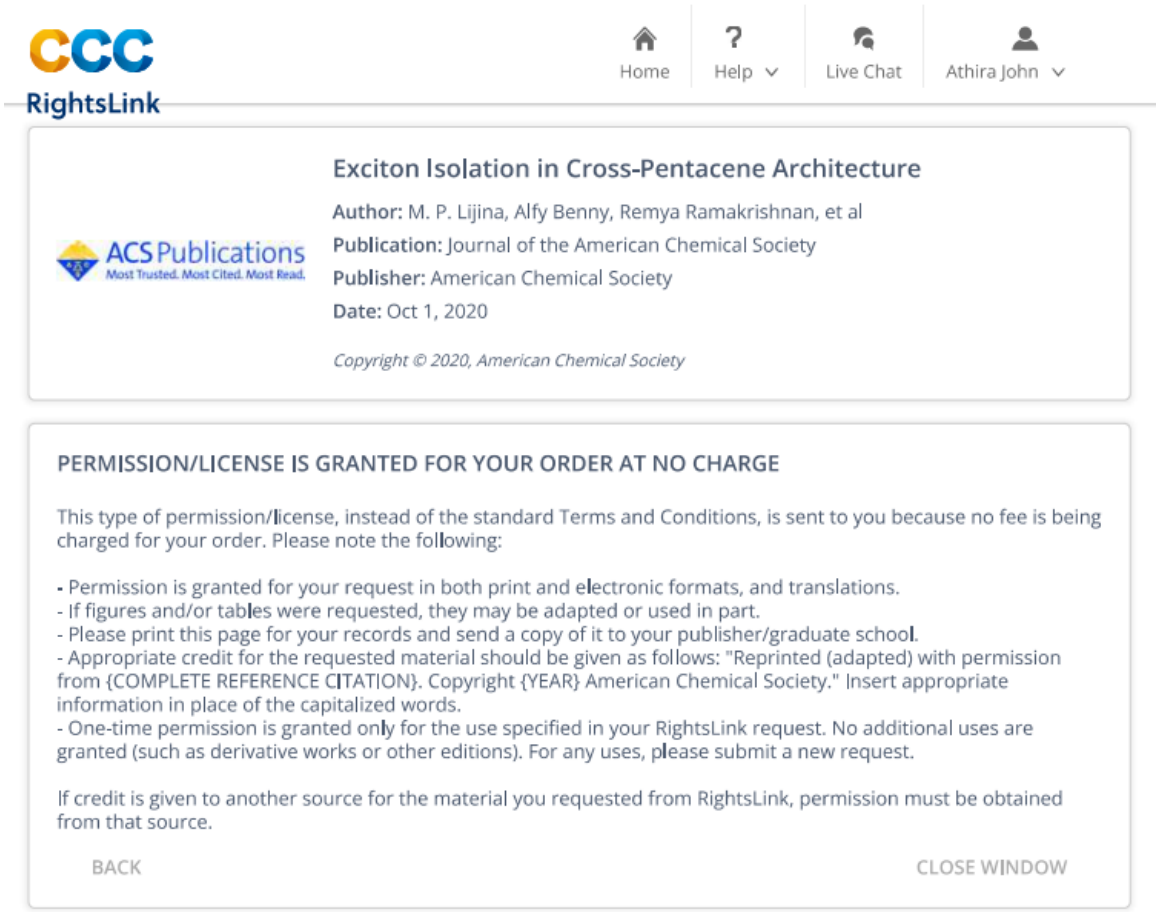

RightsLink

Home Help Live Chat Athira John

ACS Publications
Most Trusted. Most Cited. Most Read.

Exciton Isolation in Cross-Pentacene Architecture

Author: M. P. Lijina, Alfy Benny, Remya Ramakrishnan, et al
Publication: Journal of the American Chemical Society
Publisher: American Chemical Society
Date: Oct 1, 2020

Copyright © 2020, American Chemical Society

PERMISSION/LICENSE IS GRANTED FOR YOUR ORDER AT NO CHARGE

This type of permission/license, instead of the standard Terms and Conditions, is sent to you because no fee is being charged for your order. Please note the following:

- Permission is granted for your request in both print and electronic formats, and translations.
- If figures and/or tables were requested, they may be adapted or used in part.
- Please print this page for your records and send a copy of it to your publisher/graduate school.
- Appropriate credit for the requested material should be given as follows: "Reprinted (adapted) with permission from {COMPLETE REFERENCE CITATION}. Copyright {YEAR} American Chemical Society." Insert appropriate information in place of the capitalized words.
- One-time permission is granted only for the use specified in your RightsLink request. No additional uses are granted (such as derivative works or other editions). For any uses, please submit a new request.

If credit is given to another source for the material you requested from RightsLink, permission must be obtained from that source.

BACK CLOSE WINDOW

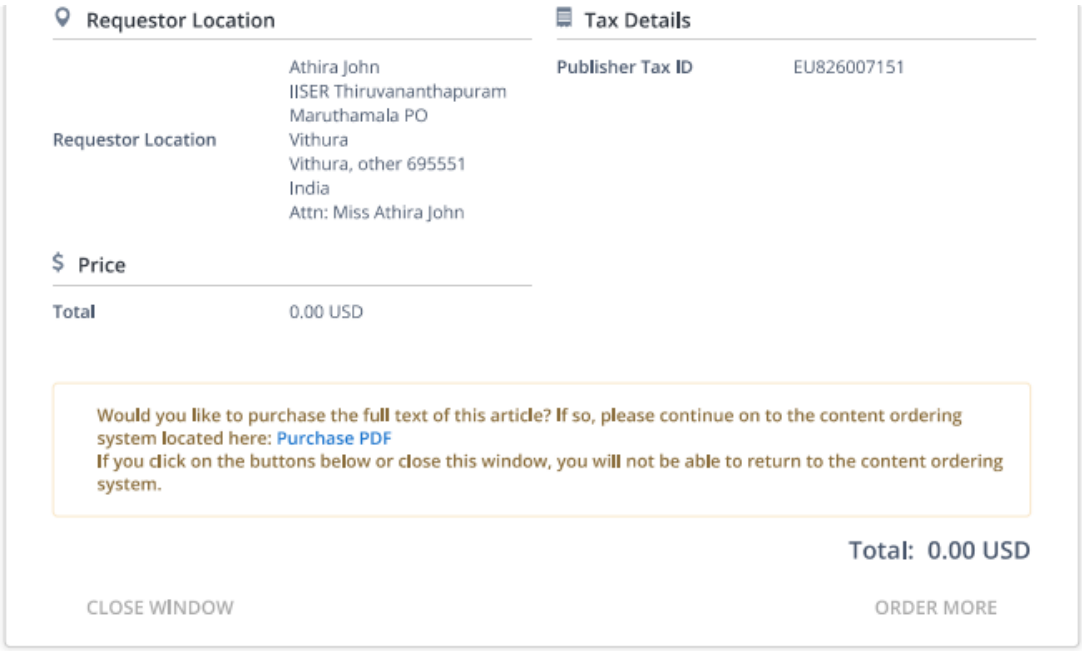

Requestor Location

Requestor Location	Athira John IISER Thiruvananthapuram Maruthamala PO Vithura Vithura, other 695551 India Attn: Miss Athira John

Tax Details

Publisher Tax ID	EU826007151

Price

Total	0.00 USD

Would you like to purchase the full text of this article? If so, please continue on to the content ordering system located here: Purchase PDF
If you click on the buttons below or close this window, you will not be able to return to the content ordering system.

Total: 0.00 USD

CLOSE WINDOW ORDER MORE